UNIVERSITÀ DELLA CALABRIA

UNIVERSITA' DELLA CALABRIA

Dipartimento di Ingegneria Informatica, Modellistica, Elettronica e Sistemistica (DIMES)

Scuola di Dottorato

Archimede

Indirizzo

Scienze, Comunicazione e Tecnologie

CICLO

XXVIII

DESIGN OF HIGH-EFFICIENCY CRYSTALLINE SILICON SOLAR CELLS BASED ON NUMERICAL SIMULATIONS

Settore Scientifico Disciplinare ING-INF/01 ELETTRONICA

Direttore: Ch.mo Prof. Pietro Pantano

Firma _____

Relatore: Ch.mo Prof. Giuseppe Cocorullo

Firma _____

Correlatore: Ch.mo Prof. Felice Crupi

Firma _____

Dottorando: Dott. Paul Alejandro Procel Moya

Firma _____

Contents

One

1 Introduction

1.1 Solar Energy

Solar energy potentially is by far the more abundant energy resource. Even if we consider only emerged continents, its potential energy amount is around 23000 TWy/y [1]. Such value overpass by several orders of magnitude the current world energy consumption of 18TWy [2] and 27TWy projected to 2040. However, around 80% of world energy consumption comes from finite energy resources as coal, fuel and nuclear [2], even when their consumption is associated to the so called greenhouse gases. Among these, considering the plenty of potential energy coming from sunlight make this option as the most attractive to face a promising future of human society. Even more, solar energy is free, and worldwide accessible. Therefore, it is crucial that in the near future, solar energy will become a very important option in the generation of electrical energy by means of photovoltaic (PV) conversion inside a semiconductor device (solar cells). Among that, according to ITRPV report [3], in 2016 the PV module production capacity of 60GWp is overpassing the global market demand for second consecutive year. Thus, to keep the prices reduction has become the main challenge to PV industry. However, to address this situation, some strategies can be developed by optimizing mate-

rials use and by improving conversion efficiency of the PV module/solar cell.

1.2 c-Si Solar Cells

Crystalline silicon (c-Si) solar cells dominates current PV market thanks to the material abundance, low processing cost and relatively high conversion efficiency [3]. In fact, c-Si solar cells industry is associated to integrated circuit market and are the more efficient of commercial solar cells. Moreover, recently, bulk production of c-Si ingots has been also improved on last years by reducing the presence of impurities in crystalline structure, expanding the potential achievable efficiency. However, c-Si characteristics are not the best for PV applications. In particular, c-Si has an indirect bandgap of 1.12 eV equivalent to 1160nm spectrum wavelength cut-off [4] that corresponds to a relatively low absorption coefficient that can be counterposed by using light-trapping schemes. Light-trapping consists on the formation of texturized surfaces covered by Anti-Reflect Coatings (ARC) in front and Back-Reflectors (BR) on rear side in order to catch more efficiently sun light.

To control and avoid the presence of minority carriers at defective interfaces passivation schemes are used. Such passivation strategies are chemical when depositing thin layers of dielectric with charges that catch the interface crystal dangling bounds, or electrical when using highly doped regions or depositing charged layers to repel the charges from silicon boundaries. Accordingly, to collect generated carriers inside the bulk into the metallic contacts, similar structures are needed, but in this case, they have to allow the transport of one type of charges (electrons or holes) and repealing the others from interfaces.

1.3 Efficiency limit

Considering only radiative recombination mechanism, Shockley and Queisser [5] estimated a theoretical conversion efficiency limit of 33.5%. However, due to the fact that silicon has an indirect bangap, the radiative recombination is minimized, but Auger recombination becomes dominant. Consequently, on the basis of state-of-the-art semi empirical Auger recombination model [6], Richter et al estimated the limit of efficiency for c_Si in 29.4% [7]. This limit is not feasible, but mark the direction on the task to reach more efficient solar cells. A more realistic or practical limit was proposed by Swanson [8] on 26%, but this limit underestimate the potential to apply novel structures as passivated contacts. Considering such structure the practical limit could be considered to 27% keeping same assumptions than Swanson.

1.4 Evolution of c-Si solar cells

The evolution of c-Si solar cells in the history it is summarized on Figure 1.1 and it is clear the increasing trend in the time. Such evolution has been well reported by Green in [9].

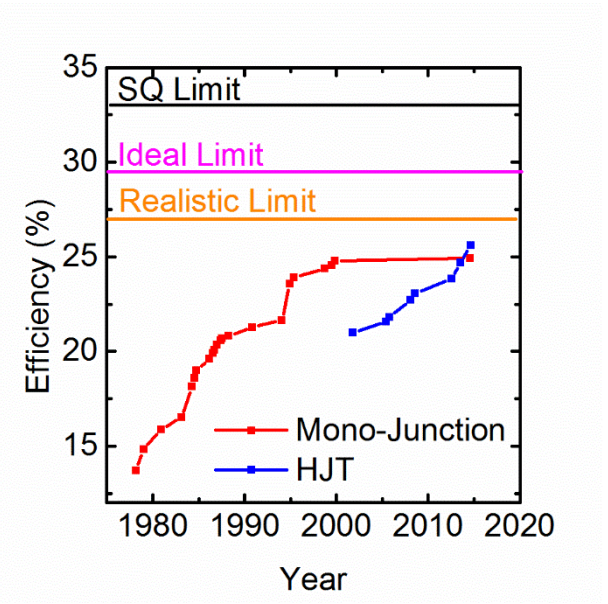

Figure 1.1: History of c-Si solar cells efficiency. Mono-junction structures are showed in red and hetero-junction in blue. The plot is based on data from NREL report [10]

However, in order to summarize it, the following milestone are presented:

- In 1941, Ohl reported the first silicon solar cell with an efficiency around 1% [11]
- In 1953, 1954 and 1955 Bell Laboratories announced 4.5% [12], 6% and 10% efficiency [13]
- In 1961, commercial cell reported 14.5% efficiency for n-type bulk.
- In 1963, it was assessed the effect of n-type and p-type bulk in space radiation, giving a better result for p-type bulks [14]
- In 1970 and 1974 Comsat Laboratories reported a 13.7% and 15 % [15]respectively efficiency on p-type silico solar cells
- In 1976, Rittner reported an efficiency of 16.7% [16]
- In 1983, UNSW cell showed 18% efficiency [17]

- In 1985, UNSW reported for first a 20% efficiency passivated emitter solar cell (PESC)
- In 1988, UNSW announced a fabricated PESC solar cell 21.4%
- In 1988, Standford, reported a fabricated 22.3% efficiency solar cell
- In 1989, UNSW fabricated 23% efficiency passivated emitter rear locally diffused (PERL) solar cell that was improved to 24.7% in 1999.
- In 2014, Sunpower announced an interdigitated back-contact (IBC) solar cell of 25% efficiency
- In 2016, Kaneka apply HIT junction IBC achieving 26.3% efficiency [18].

1.5 Novel Strategies to improve conversion Efficiency

1.5.1 Selective diffusions and Localized contacts

Doping impurities diffusion are used in contact regions to attract collecting carriers to the metal contact. Similarly, such diffusion is used to avoid that minority carriers arrive to defective interfaces. It has been also demonstrated that doping underneath the metallic interfaces has to be high enough in order to improve interface resistivity and increase the fill factor (FF). However, highly doped regions leads to low resistivity regions, but at the same time increase Auger recombination. Such compromise has aimed to reduce metallic interfaces as well than highly doped regions. In fact, beyond that fabrication process are increased, localized contacts with selective diffusion increased efficiency when modeling these structures [19].

1.5.2 Passivated Contacts/Selective contacts

To achieve a good passivation on c-Si is one of the keys to achieve higher efficiencies. Indeed, metallized interfaces are highly defective and they can be passivated and collect carriers thanks to the use of passivated contacts. Such structure consists on applying a very thin layer of a wide bandgap material (usually SiO2) between metal and silicon interface forming heterojunctions (HJT). Collection and transport mechanism are achieved thanks to the quantum tunneling mechanisms occurring through the passivating layer. The efficiency improvements of this architecture are expressed on reported efficiencies over 25% [20][21], with the potential to go beyond.

1.6 Advanced Solar Cells

Recently, in the task for efficiency increase and cost reduce of solar cells, new cell designs have been proposed and developed. In this way, novel concepts has been presented to attract the interest of the PV industry.

1.6.1 Heterojunctions solar cells

In order to achieve a better passivation and at the same time carrier collection, as previously explained, a junction from 2 different materials are used. This material is applied as a thin layer among silicon and metal (See Figure 1.2). This thin layer has to accomplish two passivating conditions: chemical and electrical passivation by using ionized dopants to achieve a good band alignment. This concept commonly consider the deposition of amorphous silicon (a-Si) layer, and has demonstrate clear improvements especially on

open circuit voltage (Voc) values. In fact, world record c-Si solar cell achieved 25.6% of conversion efficiency with a Voc of 0.74 V.

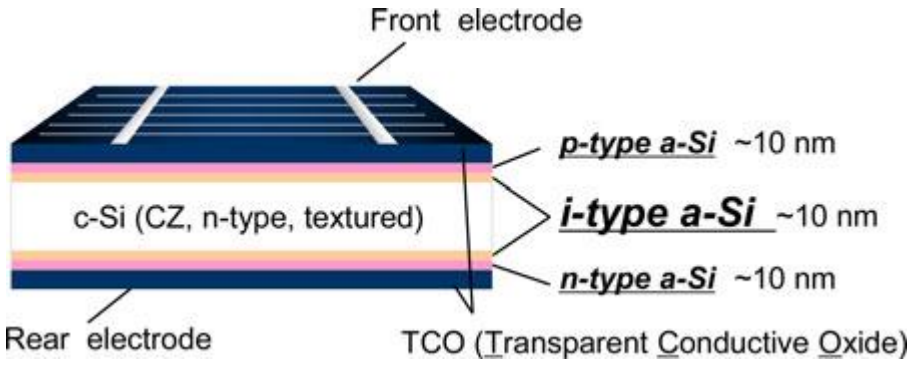

Figure 1.2: HIT Solar Cell [22]

1.6.2 Tunneling Oxide Passivated Contact (TOPcon)

This novel concept created by Fraunhover ISE, consist on the use of the advantages of conventional homo-junction solar cell as light-trapping and a complete rear passivated contact (see Figure 1.3). Therefore, transport among the solar cell is simplified because the straight carrier collecting paths and using high quality passivation schemes. Such advantages are expressed in terms of FF and Voc improvement that have been demonstrated to reach 83.2% FF, 0.718 V of Voc with 25.1% of efficiency. However, front contact width has to be as small as possible in order to avoid shading losses.

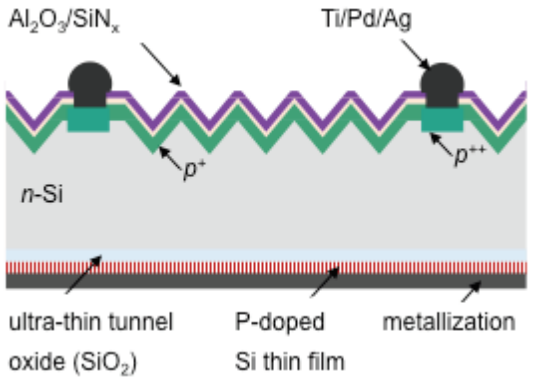

Figure 1.3: Sketch of TOPcon solar cell [20][23]

1.6.3 Interdigitated Back-Contact IBC

Back-Contact Back-Junction solar cells (BC-BJ) allow improving conversion efficiency (η) because of the absence of front contact shadowing and simplified cell interconnection at module level (see Figure 1.4). Thanks to these advantages, efficiencies over 25% have been already reported [21][18] with the potential to go beyond. On the other hand, BC-BJ efficiency is sensitive to recombination mechanisms related to fabrication process, such as SRH recombination due to defectiveness in bulk and at interfaces [24].

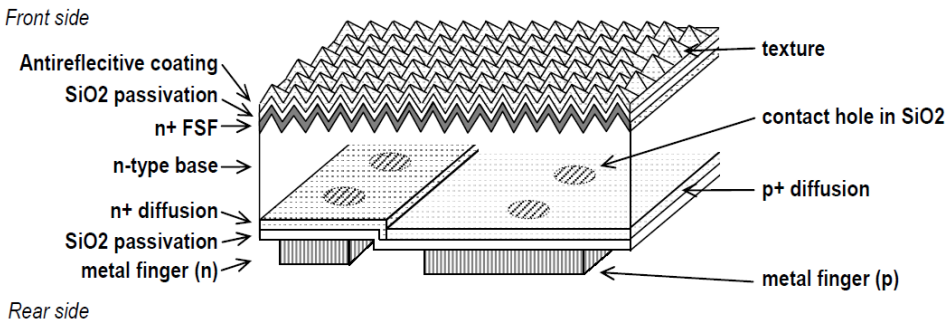

Figure 1.4: Sketch of IBC solar cell [25]

1.7 Solar Cell Numerical Simulations

Advanced solar cells are becoming more complex and usually demands more fabrication process steps and thus, requiring the assist of simulation tools. Accordingly, the use of numerical simulations has become a strategic and critical key in the improvement of PV efficiency by optimizing their geometrical and process design. Moreover, simulation tools provides an insight of Physics inside the solar cell and assist researchers to predict efficiency dependence from design parameters [26]. It is worth noting, that due to their own inherent complexity, advanced solar cell structures can be only investigated using two or three dimensional simulations tools.

Numerical simulators, so called technology computer-aided design (TCAD), are a very used tool in the semiconductor industry and have been developed for more than 20 years [27]. Therefore, TCAD support has been stablished as strategic target to achieve nowadays photovoltaics challenges: more efficient and less costly advanced solar cells. In general, device simulations consist on the solution of the semiconductor transport equations in semiconductor regions using metal contacts as boundary conditions. Even more, solutions account several external conditions such as interaction of impurities, doping, traps defects, activation energy, tunneling, etc. Because of their unique opto-electrical physics, solar cells simulations have to account a wide range of parameters that include optical and electrical models according to properties of materials composing the device especially anti-reflect coating (ARC), and their interfaces.

1.8 Aim of the Thesis

The aim of this Thesis is to provide guidelines for the design of c-Si based solar cells featuring advanced architecture and novel physical mechanisms as interdigitated back contact back junction (iBC) structures and carrier selective contacts. Accordingly, this contribution is based on TCAD simulations (Sentaurus) and is focused on identifying critical design parameters by understanding the competitive mechanisms associated to each design parameter. Thereby, by accounting technological constrains, optimized designs are presented in the path to achieve the highest efficiency.

In order to present such contribution, this thesis is presented in different chapters.

In Chapter 2, the general state-of-the-art properties related to c-Si solar cells is described. In particular, c-Si models and parameters are identified and presented with the aim to calibrate and implement them in TCAD Sentaurus platform to obtain realistic results.

In Chapter 3, a theoretical study based on electro-optical numerical simulations of the impact of geometrical and doping parameters on main figures of merit of crystalline silicon back-contact back-junction solar cells is presented. The studied design parameters are the doping level in front surface field (FSF), back surface field (BSF) and emitter, and the main geometrical parameters. A doping level value that allows the maximization of the efficiency for the three highly doped regions can be clearly identified. In particular, for BSF and emitter, an efficiency degradation is observed for relatively lower doping values and is ascribed to the higher contact recombination while for higher doping values the Auger recombination plays a significant role in reducing the ultimate efficiency. In FSF region the recombination due to defects at the front interface is the main limiting mechanisms for efficiency. On

the basis of the analysis, a marked sensitivity of the efficiency to the gap and pitch size is caused by the series resistance increase. The efficiency exhibits a maximum value for an emitter coverage fraction (R) of 85%. However, in the case of lower emitter coverage, Auger, Shockley-Read-Hall (SRH): in bulk and at interfaces are detrimental for the cell conversion efficiency.

In Chapter 4, a novel IBC simulation model is presented, validated and deployed to study optical light-trapping and front recombination competitive mechanisms. In collaboration with TUDelft, the model presented on Chapter 2 has been upgraded and calibrated. A more accurate simulation methodology is presented to account in detail the optical and passivation mechanisms of front texturization. Its validation has been carried out with respect to a novel homo-junction IBC c-Si solar cell based on ion implantation and epitaxial growth, comparing measured and simulated Reflectance (R), Transmittance (T), Internal Quantum Efficiency (IQE), External Quantum Efficiency (EQE) spectra and current density-voltage characteristics. As a result of the calibration process, the opto-electrical losses of the investigated device have been identified quantitatively and qualitatively. Then, an optimization study about the optimal front surface field (FSF) doping, front-side texturing morphology, and rear-side geometry has been performed. Simulation results show that a not-smoothed pyramid-textured front interface and an optimal FSF doping are mandatory to minimize both the optical and the recombination losses in the considered IBC cell and, consequently, to maximize the conversion efficiency. Similarly, it has been showed that recombination losses are affected more by the doping profile rather than the surface smoothing. Moreover, the performed investigation reveals that the optimal FSF doping is almost independent from the front texturing morphology and FSF passivation quality. According to this result, it has been demonstrated that an IBC cell featuring an optimal FSF doping does not exhibit a signifi-

cant efficiency improvement when the FSF passivation quality strongly improves, proving that IBC cell designs based on low-doped FSF require a very outstanding passivation quality to be competitive. Deploying an optimization algorithm, the adoption of an optimized rear-side geometry can potentially lead to an efficiency improvement of about 1%abs as compared to the reference IBC solar cell. Further, by improving both emitter and c-Si bulk quality, a 22.84% efficient solar cell for 280-μm thick c-Si bulk was simulated.

In Chapter 5, a validated simulation model is used to identify critical design parameters when using passivated contacts in a conventional solar cells. Simulation results shows that energy barrier, electron and holes tunneling masses, and oxide thickness are the critical parameters that constrains transport mechanisms. With the aim to study effects related to band alignment it has been deployed a set of simulations for different band gap and electron affinity range. It has been demonstrated that transport mechanism are limited also for band alignment quality which is correlated to the calculated build in voltage (V_{bi}). For small V_{bi} values, transport mechanism are constrained by the absence of holes on c-Si/oxide interface. For large V_{bi} values, transport mechanisms are constrained by the band bending achieved on oxide/deposited layer interface. It was also qualitatively identified a V_{bi} interval in which a good transport mechanisms are achievable for optimal band alignment cases. Regarding small V_{bi} values, it is identified the assist of in-diffusion in c-Si in order to improve solve aforementioned transport issues. Similarly, a critical doping that allows tunneling mechanisms work is also identified and it depends on to the density of filled states and relative permittivity of deposited material.

In Chapter 6 conclusions of this thesis are presented.

Two

2 Modelling of Crystalline Silicon

In this chapter, a review of the solar cell modeling is presented. It is considered state-of-the-art crystalline silicon parameters as well than new models. Accordingly, it is explained the adoption of a novel model describing intrinsic recombination for silicon. Finally, the typical solar cell simulation scheme is described.

2.1 Numerical Simulations

Numerical simulations are based on the discretization of a virtual device into Finite Elements that reproduces numerically electrical behaviour of semiconductor devices. For the case of solar cell devices, the simulator estimates charge distribution and transport mechanisms according to the so called Drift Diffusion Model. Therefore, the solar cell device are replicated virtually by means of geometrical, materials stack, interfaces and doping profiles discretized onto a grid so called mesh [28] and then solved calculating electrical parameters according to boundary and physical conditions.

2.1.1 Element Discretization (Mesh)

The accuracy of the numerical solution of the device is related to the grid resolution but, at the same time a large number of points could be limited by computational resources. Consequently, discretization of the device is a crucial stage on device modelling, because it has to lead to an accurate solution in feasible computational time. However, solar cells are highly symmetrical devices that allows to account the most element of symmetry to consider as simulation domain. Therefore, by modelling only this simulation domain, the entire solar cell behaviour can be replicated. However some special considerations have to account in particular regions of the solar cell in which parameters gradient is large among spatial reference. Hence, a small mesh step size has to be considered in such regions. According to Altermatt et al [29] a good mesh can be achieved by starting with a resolution of parallel to 1nm from the front interfaces and 10nm for other cases and the mesh step size can be coarser going inside the cell. However, such initial mesh resolution value is a reference that can be modified depending on the mechanisms that dominates some regions. For instance, these regions are i) front surface, where the absorption of most energetic photons occurs and surface recombination needs to be modelled accurately, ii) back surface, again for optimal modelling of surface recombination, both on passivation layer and contacts, iii) the interface region between emitter and base. Similarly, to reproduce accurately light-trapping mechanisms different resolution are recommendable similarly to mimic tunnelling mechanisms in case of passivating contacts, and of course, considering the grid size (i.e. 2D or 3D simulation). Thus, choosing an adequate mesh is an iterative process that account accuracy and attainable computational time for solving the parameters of the device.

2.1.2 Electrical Modelling

In order to accurate reproduce semiconductor modelling for different conditions, the Drift Diffusion model is applied to attain an adequate accuracy in modelling of solar cells [29]. Then, the semiconductor are solved by coupling Poisson equation (1) with continuity equation (2 and 3) and Drift-Diffusion equations (4 and 5):

$$\nabla^2\Phi(r,t) = -\frac{\rho(r,t)}{\varepsilon} \qquad (1)$$

$$\frac{1}{q}\nabla\cdot\overrightarrow{J_p} = G_{OPT} - R_p - \frac{\partial p}{\partial t} \qquad (2)$$

$$\frac{1}{q}\nabla\cdot\overrightarrow{J_n} = R_n - G_{OPT} + \frac{\partial n}{\partial t} \qquad (3)$$

$$\overrightarrow{J_p} = -q\mu_p pE - qD_p\nabla p \qquad (4)$$

$$\overrightarrow{J_n} = -q\mu_n nE + qD_n\nabla n \qquad (5)$$

2.1.3 Optical Modelling

Beyond that there is several methods to solve the optical behaviour of a solar cell by calculating optical generation G_{OPT}, Ray-traycing algorithm is the most commonly used due to the low use of computational resources and the capability of reproduce texturing effects when evaluating light-trapping. Therefore, in this thesis we have used Ray-tracer from Sentaurus [28] in the optical platform.

Commonly, a 3-D optical simulations are performed by raytracing simulator accounting for a thin film stack boundary condition to model ARC at the front interface and elemental texturing element at top. The incidence angle of rays is passed as input to a Transfer Matrix Method (TMM) solver

which returns the reflectance, transmittance, and absorbance to the raytracer assuming absorbance, refractive and extinction coefficients as probability within Monte Carlo approach [28],[30], [31]. The angle of refraction is calculated by the raytracer according to Snell's law.

In particular, the TMM-based model adopted for the ARC stack layers uses a 2x2 matrix for each interface between two materials, thus representing the relationship between the incoming and outgoing transmitted and reflected waves provided at each interface as follows:

$$\begin{pmatrix} T_j^+ \\ R_j^+ \end{pmatrix} = M_{j,j+1} \begin{pmatrix} T_{j+1}^- \\ R_{j+1}^- \end{pmatrix} \qquad (6)$$

$$M_{j,j+1} = \begin{bmatrix} A & B \\ B & A \end{bmatrix} \qquad (7)$$

where

$C=exp(2\pi i n_j d_j/\lambda cos\varphi_j)$ *and* $D=exp(-2\pi i n_j d_j/\lambda cos\varphi_j)$

j is the material index and φ_j is the incidence angle in the material j. The relationship for thin layers with a thickness d smaller than the coherence length of the light becomes:

$$\begin{pmatrix} T_j^- \\ R_j^- \end{pmatrix} = M_j \begin{pmatrix} T_j^+ \\ R_j^+ \end{pmatrix} \qquad (8)$$

$$M_j = \begin{bmatrix} C & 0 \\ 0 & D \end{bmatrix} \qquad (9)$$

where

$C=exp(2\pi i n_j d_j/\lambda cos\varphi_j)$ *and* $D=exp(-2\pi i n_j d_j/\lambda cos\varphi_j)$.

Assuming that the transmitted wave at the end of the ARC stack is not back-reflected and knowing the intensity I and the angle of incidence φ of the input light, it is possible to relate the layers of the ARC stack through the following relationship:

$$\binom{I}{0} = M^{*}_{ARC} \binom{R_{ARC}}{T_{ARC}} \qquad (10)$$

where M^{*}_{ARC} is the inverse matrix given by the product of all interfaces matrices, R_{ARC} and T_{ARC} are the reflectance and the transmittance of the ARC layer, respectively. Hence, the computational cost of solving the optical problem is clearly reduced and simplified. However, this assumption is valid before until the second reflectance becomes apparent, such effect will be discussed on Chapter 4.

As result of the optical model, the 3-D optical generation map calculated is spatially integrated over the distance from the front interface in order to calculate the 1-D optical generation profiles. Lastly, the optical generation map is interpolated on the spatially nonuniform 2-D mesh for the device simulation [32].

2.1.4 Boundary conditions

In order to mimic the symmetry of the simulation domain and to describe some electrical scenarios, boundary condition has to be carefully specified and designated. For instance, in optical simulation, the boundaries between symmetry elements in optical simulation has to be set with perfect reflectivity to account properly the behaviour of the complete solar cell. In case of emulating ARC effects, TMM boundary conditions has to be specified, as well as Snell's law in the other cases. Accordingly, for electrical simulation, the boundary condition has to be specified on the metallic contact in order to model the conditions in which the solar cell has to be evaluated (i.e. different voltages to build J-V curve). It is worth noting that, for electrical simulation, on the boundaries of simulation domain, current and charges are assumed to

be symmetrical, then, there is no charge crossing from one symmetry element to another.

2.2 c-Si Models and Properties

c-Si dominates PV market because the low costs achieved thanks to research and development contribute by electronic field.

Table 1 Summary of the physical models and parameters used in modelling c-Si solar cells.

	Model parameter	**Value**
Intrinsic Parameters	Free carrier statistics	Fermi-Dirac [26]
	Bandgap narrowing	Schenk [33][34]
	Mobility	Klaassen [35]
	Intrinsic recombination: Auger and radiative	Richter [36], [37]
	Intrinsic carrier density	Altermatt [38] (9.65×10^{9} cm^{-3} at 300 K)
	Optical Properties c-Si	Green [39]
Extrinsic Parameters	Metal/Si interface recombination velocity	$1x10^{7}$ cm/s (thermal velocity)
	SRH lifetime	Calibration of Scharfetter relation [40] from measurements
	Surface SRH recombination velocity at passivated interfaces	Calibration of Altermatt's model [41] from measurements
	Contact resistance	Calibration of a distributed resistance model from interface resistivity measurements
	Finger and bus bar resistance	Distributed model according to material resistivity
	Optical Properties ARC	Measurements depending on material [42]

Consequently, parameters from c-Si have been reported and studied deeply and have been assumed for PV community to deploy theoretical studies. Due

to its inherent simplicity, solar cell can be considered as diode with a high quality emitter working on low injection regime from electronic point of view [29]. Therefore, parameters and models used on PV field has to describe accurately such behaviour and has been studied and reported by Altermatt et al [29] and Fell et al [26] and summarized on Table 1. It is worth noting that models and parameters described are directly related on the previously explained Drift Diffusion model. In general, parameters can be considered intrinsic, those implicitly realated to the material (c-Si) and extrinsic, those related to fabrication process.

Most of the detailed models are already implemented in TCAD Sentaurus. However, it was not the case of intrinsic recombination semi-empirical model proposed by Richter et al [6]. In this case, the model was implemented by means of Physical Model Interface in Sentaurus [28]. Such model was validated according to experimental data reported [6] and showed on Figure 1 and Figure 2. Effective lifetime has been estimated by:

$$\frac{1}{\tau_{eff}} = \frac{1}{\tau_{int}} + \frac{1}{\tau_{srh}} + \frac{1}{\tau_s} \qquad (11)$$

Where τ_{eff} is the effective lifetime measured from Quasi-Steady-State-Photoconductance (QSSP) method [43], τ_{int} is lifetime factor reported on [6], and τ_{SRH} and τ_{s} is used as fitting parameter to estimate bulk lifetime and surface recombination velocity (SRV).

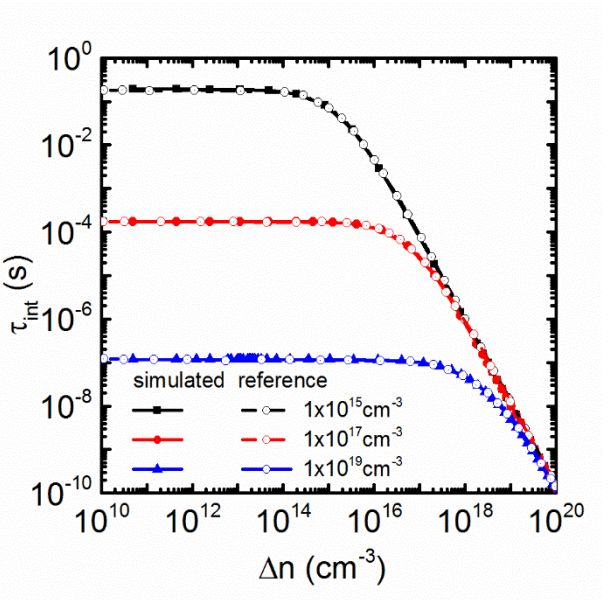

Figure 1: Implemented Auger model validated by [6]

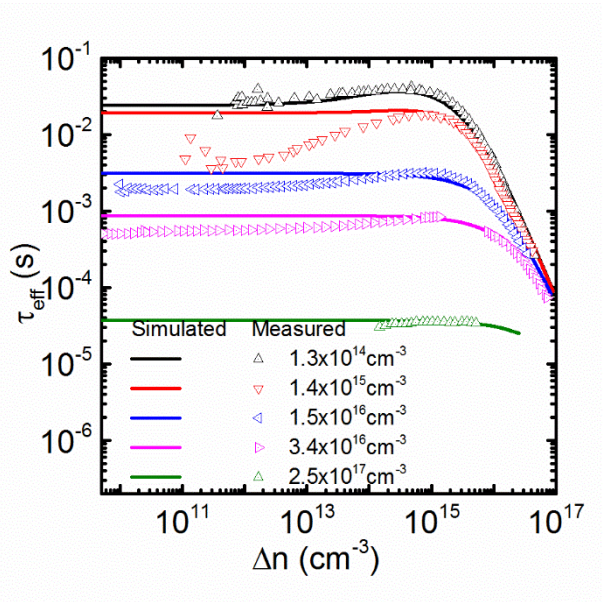

Figure 2: Implemented Auger model validated with measurements reported in [6]

Intrinsic physical models are implemented according to state-of-the-art, while the extrinsic physical models are implemented by calibration or measured parameters.

Accordingly, recombination losses due to trap-assisted recombination through deep defect level and due to defects at material interfaces are commonly modelled by assuming the single-level trap model by Shockley-Read-Hall (SRH) [44], [40] with traps in the energy mid-gap. In this way, bulk lifetime (τsrh) is calculated by the doping dependant model according to:

$$\tau_{SRH} = \frac{\tau_{max}}{1+\left(\frac{N_{A,D}}{N_{ref}}\right)^{\gamma}} \quad (12)$$

where τmax are related to the value estimated by using fabrication parameter fitted in (τ_{eff} equation), $N_{A,D}$ represents the acceptor or donor doping concentration, respectively. In order to evaluate doping process related issues for solar cell fabrication, N_{ref} and γ are used as calibration parameters to model the SRH recombination lifetime in the different doped regions of the simulated solar cell. Similarly, to account for SRH recombination due to defects at material interfaces are modelled by surface recombination velocity that usually is estimated from measurements by fitting $\tau SRH = \frac{\tau_{max}}{1+\left(\frac{N_{A,D}}{N_{ref}}\right)^{\gamma}}$

(12. It is worth noting that some works has reported a dependence of SRV with doping concentration at interface [14], [18]. In order to model the very highly defective metal/semiconductor interface, almost thermal surface recombination velocity is usually assumed to $1x10^7$cm/s.

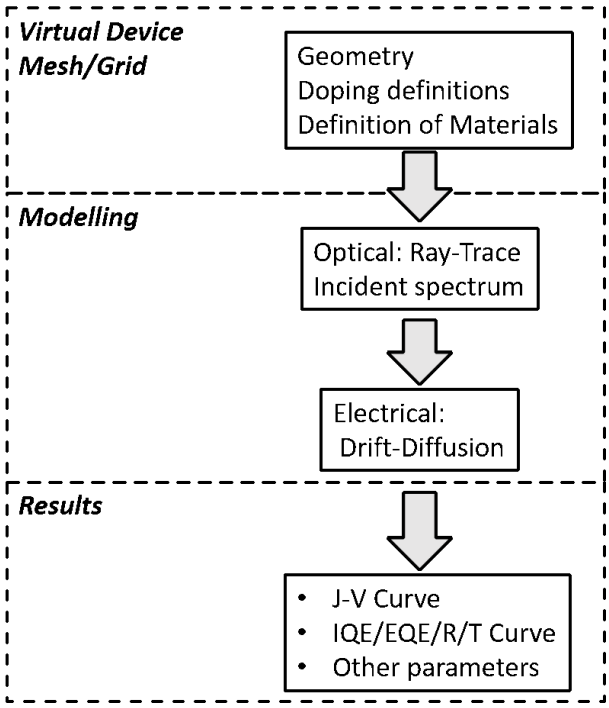

Figure 3: Simulation process scheme

The optical generation rate profiles is calculated assuming illumination with normal incidence with respect to the device plane and standard AM1.5G spectrum (1000 W/m2) [47]. Then the electrical simulation is deployed in order to reach solar cell FOM and spectral response, as it is explained on Figure 3.

Accordingly, simulation-based works have employed a two-step simulation approach [26]. First, an optical model, typically based on ray tracing (RT) or rigorous Maxwell's solvers for devices with nano-textured features, derives the generation profile of electron-hole pairs within the device. Second, an electrical model based on drift-diffusion uses as an input the calculated optical generation profile [26]. For the sake of simplicity, this approach typically involves in each step the use of different simulation domains. In

fact, the optical simulation is carried out on an element that features textured surfaces (light-trapping) with the aim of properly accounting for the optical situation within the silicon. The electrical simulation instead usually is set up on an approximated simulation domain that simply features planar surfaces.

Three

3 Numerical Simulation of the Impact of Design Parameters on the Performance of IBC Solar Cell

In this Chapter, updated physical models of realistic parameters were used on TCAD simulations in order to present a systematic and extensive analysis of the dependence of monocrystalline silicon BC-BJ solar cell FOM on the doping level of the different regions and on main geometrical parameters. The aim of this paper is twofold. One aim is to deepen our physical understanding of BC-BJ solar cells. The second one is to provide guidelines for the design of BC-BJ solar cells. To this purpose, it has been used the simulation results about different physical mechanisms, such as the recombination of photogenerated carriers and the influence of doping levels and geometrical parameters on electrical field intensity and parasitic resistance. Numerical Simulation of the Impact of Design Parameters on the Performance of Back-Contact Back-Junction Solar Cell.

(This Chapter is based on the following publication: P. Procel, M. Zanuccoli, V. Maccaronio, F. Crupi, G. Cocorullo, P. Magnone, and C. Fiegna, "Numerical simulation of the impact of design parameters on the performance of back-contact back-junction solar cell," J. Comput. Electron., vol. 15, no. 1, pp. 260–268, Mar. 2016.)

3.1 Simulation Approach

Figure 1 reports a schematic representation of the element of symmetry of the simulated solar cells. It has been considered a FZ-Si n-type doped wafer featuring a resistivity of 2 Ω-cm within the range reported by McIntosh et al. [48]. The doping profiles in BSF, FSF and emitter are described by Gaussian functions featuring a peak located at the edge of the interface and with a junction depth of 2µm for BSF and emitter and of 1µm for FSF region [49].

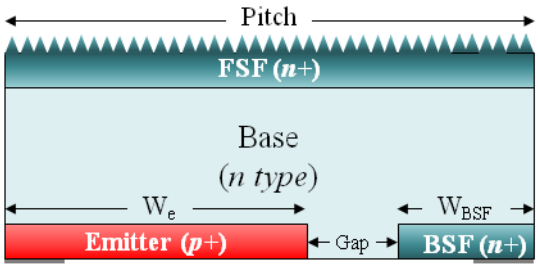

Figure 1: Element of symmetry of BC-BJ solar cell used as domain of simulation

3-D optical simulations have been performed by raytracing simulator accounting for a thin film stack boundary condition to model ARC at the front interface. The incidence angle of rays is passed as input to a Transfer Matrix Method (TMM) solver which returns the reflectance, transmittance, and absorbance to the raytracer. The angle of refraction is calculated by the raytracer according to Snell's law. The front surface is coated by a double-layer anti-reflective coating (ARC) composed by 42nm Si3N4 and 27nm SiO2, texturized by regular upright pyramids featuring a 10 µm-wide base and opening angle between the two faces of the pyramid equal to 70 degrees. Such ARC configuration is close to the optimum one.

The non-metallized back side is passivized by a 0.1 μm-thick SiO2 layer, thus, bottom internal reflectance is calculated by means of Fresnel equations according to the kind of back interface, passivated or contacted by aluminum. The 3-D optical generation map calculated for different wafer thickness values is spatially integrated over the distance from the front interface in order to calculate the 1-D optical generation profiles. Lastly, the optical generation map is interpolated on the spatially nonuniform 2-D mesh for the device simulation.

The Drift-diffusion model, suitable to attain an adequate accuracy in modeling of solar cells, has been applied by means of numerical simulations by finite element simulator Sentaurus TCAD. As explained in Chaper 2, Physical models have been calibrated by means of state-of-the-art parameterizations [28] and material properties have been considered to calculate realistic values of FOM. Recombination losses due to trap-assisted recombination through deep defect level has been modelled by assuming the single-level trap model by Shockley-Read-Hall (SRH) [44],[50] with traps in the energy mid-gap. To account for SRH recombination due to defects at material interfaces (either textured and planar), we used the doping dependent models of surface recombination velocity, at passivated interfaces suggested by Glunz et al. [51] with the parameterization reported in [41], consistently with the adopted ni value. It has been considered a 100 μm-wide metal ohmic contact without potential barrier and resistivity of 2 $m\Omega \cdot cm^2$. The recombination velocity for carriers at metal/Si interfaces has been set to $1x10^6$ cm/s. The optical generation rate profiles has been calculated assuming illumination with normal incidence with respect to the device plane and standard AM1.5G spectrum (1000 W/m^2) [47]. Lastly, we have assume fully ionized and activated doping concentrations in our simulations.

3.2 Results and discussion

In order to investigate the impact of the main doping and geometrical parameters of BC-BJ solar cell over FOM, we have performed simulations by changing doping peaks in emitter, FSF and BSF regions, and then geometrical parameters. In each set of simulations, we changed only one parameter at time in order to study its impact on the BC-BJ performance. All simulations were carried out under illumination to estimate J_{sc} recombination losses and in dark conditions [52] to evaluate the impact of the recombination losses on V_{oc} [53].

3.2.1 Doping Analysis

We simulated the entire space of parameters obtained by varying the doping peak concentration of FSF from $2.31x10^{15}cm^{-3}$ up to $1.44x10^{22}cm^{-3}$, of BSF and emitter from $1x10^{18}cm^{-3}$ up to $5x10^{22}cm^{-3}$ range. We have considered a pitch of 955 µm, a 5 µm-wide gap and 200 µm-thick wafer. The maximum efficiency equal to 22.3% was obtained for doping peak concentrations equal to $3.47x10^{18}cm^{-3}$, $1.44x10^{20}cm^{-3}$ and $4.16x10^{19}cm^{-3}$ for FSF, BSF and emitter, respectively. We observed, within the investigated doping concentration range, that in each region (BSF, FSF and emitter), a change in doping level does not affect appreciably the recombination and the carrier transport of the other regions of the device [54]. For this reason, in the following we will discuss separately about the impact of the doping of each region on FOM.

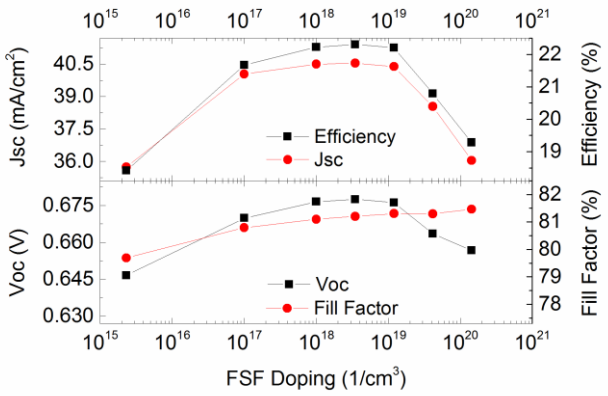

Figure 2 Simulated BC-BJ solar cell FOM as a function of FSF doping peak concentration (C_{fsf}). Efficiency exhibits a bell-shape with a clear maximum value at doping concentration level of 3x10^{18} cm^{-3}. J_{sc} and V_{oc} exhibit qualitatively the same trend

3.2.1.1 FSF Doping

Figure 2 shows solar cell FOM trends for different doping peak concentration of FSF diffusion ($C_{fsf,pk}$). We observe that η exhibits a bell-shaped leading to a maximum value for $C_{fsf,pk}$ of 3.48 x10^{18} cm^{-3} confirming qualitative trends reported by King *et al.* [55]. The η trend follows the J_{sc} bell shape, which is explained by the presence of a minimum of the of the total recombination current density under illumination for short-circuit conditions (see Figure 3).

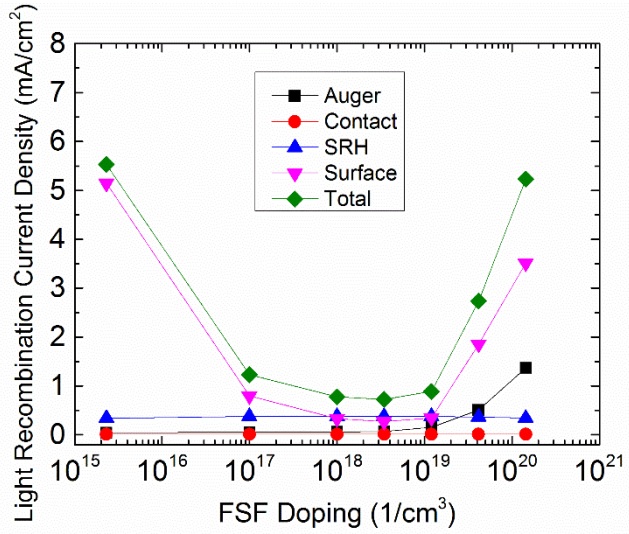

Figure 3 Recombination losses components under illumination in short-circuit conditions explaining Jsc. behavior that dominates the efficiency trend in FSF doping peak concentration (C_{fsf}) experiment. Total recombination (green) minimum point matches with maximum η in Figure 2

In turn, the trend of the total recombination current density is dictated by the trap-assisted recombination at the Si/SiO_2 front interface. For low doping levels (before the efficiency peak), the rate of the SRH recombination due to surface defects at the front texture interface decreases with decreasing doping level. As a matter of fact, a reduction in minority carrier density in the FSF region is caused by the relatively higher electrical field intensity as Figure 4 shows.

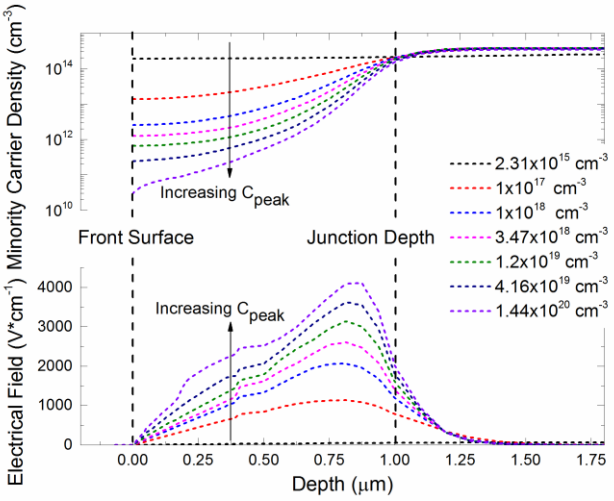

Figure 4 Comparison of minority carrier (hole) density and electrical field intensity for different FSF doping peak concentration at short-circuit condition under illumination in FSF region. Higher FSF doping levels lead to stronger electrical field intensity in the junction depth and to lower minority carrier density values at interface. Depth equal to 0 um indicates the front interface position

At high doping levels (beyond the efficiency peak), the SRH surface recombination rate becomes stronger again due to the higher SRV doping dependent value at interface contrasting with the concentration of minority carriers. An additional but less relevant contribution to the increase of the total recombination at high $C_{fsf,pk}$ is due to the Auger recombination, which clearly increases as a function of doping. It is worth noting that FF increases due to reduction of series resistance, as reported in [56].

3.2.1.2 BSF Doping

As shown in Figure 5, by increasing the peak doping concentration of BSF ($C_{bsf,pk}$), η initially rises and afterwards slightly decreases leading to a value

that maximizes η for ($C_{bsf,pk}$ = 1.44 x10^{20} cm^{-3}). Similarly to the FSF region, the influence of doping level on η is dictated by the J_{sc} trend, which is explained by the mirrored curve of the total recombination current density under illumination for short-circuit conditions (see Figure 6).

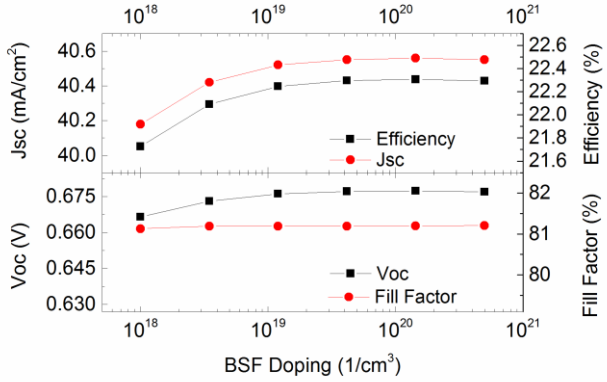

Figure 5. Simulated BC-BJ solar cell FOM as a function of BSF doping peak concentration (Cbsf). Efficiency exhibits a maximum value for peak doping concentration level 1.44x1020 cm-3. Jsc and Voc exhibit similar trends

By increasing the doping level, a lowering of the recombination at base contact is observed, hence leading to an increase of J_{SC} and η. This is ascribed to the a reduction of the minority carrier density at the Si/Al interface thanks to the stronger electrical field intensity with increasing $C_{bsf,pk}$ (Figure 7).

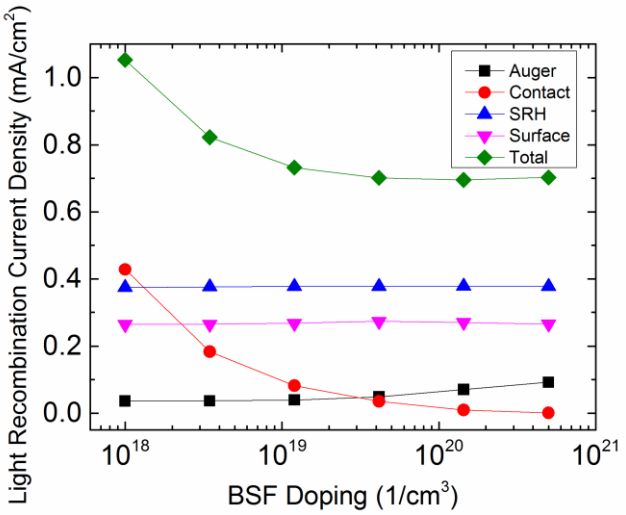

Figure 6 Recombination losses contributions under illumination in short-circuit conditions explaining J_{sc}. behavior that dominates η trend in BSF doping peak concentration (C_{bsf}) experiment. Auger recombination (black squares) exhibits an increase for higher C_{bsf} leading to a minimum point in Total recombination (green). A trade-off between recombination losses at contact and Auger recombination mechanism occurs

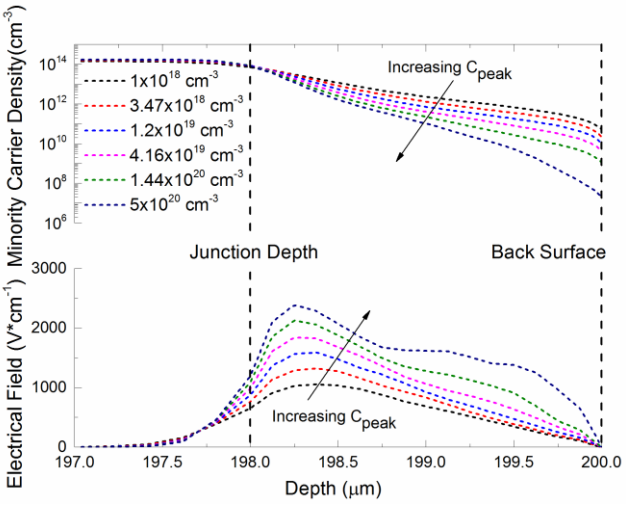

Figure 7. Comparison of minority carrier (hole) density and electrical field intensity for different BSF doping peak concentration at short-circuit condition under illumination in the BSF region. Higher doping levels lead to stronger electrical field intensity in the junction depth and to lower minority carrier density values at Si/Al interface

However, for relatively higher doping levels, the slight increase of the total recombination is due to the rise of the Auger recombination, which clearly depends on doping. Then, a trade-off, allowing to maximize η, is achieved for intermediate doping levels.

3.2.1.3 Emitter Doping

Figure 8, showing FOM trends for different doping peak concentration of the emitter diffusion ($C_{em,pk}$), indicates remarkable variations of V_{oc}, FF and consequently of η. We observe that η exhibits a bell shape leading to a maximum for a $C_{em,pk}$ value of $4.16x10^{19}$ cm^{-3}.

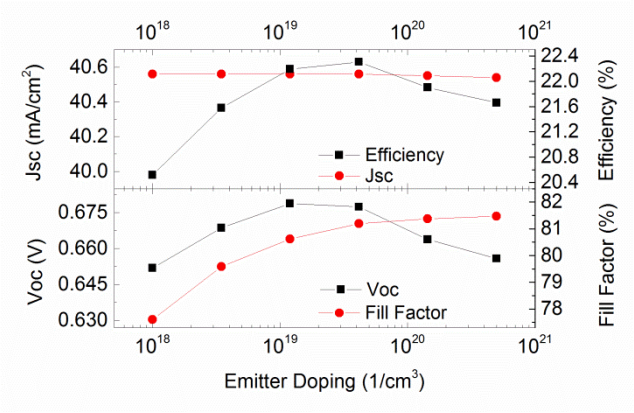

Figure 8. Simulated BC-BJ solar cell FOM as a function of emitter doping peak C_e. Efficiency exhibits a clear maximum value at peak doping concentration of $4.19x10^{19}$ cm^{-3}. V_{oc} follows the same trend. However, the maximum point for η is different from V_{oc} due to the degradation of FF for lower C_e values

The trend of V_{oc} becomes apparent by examining the mirrored behaviour of the total saturation current density in dark conditions, plotted in Figure 9.

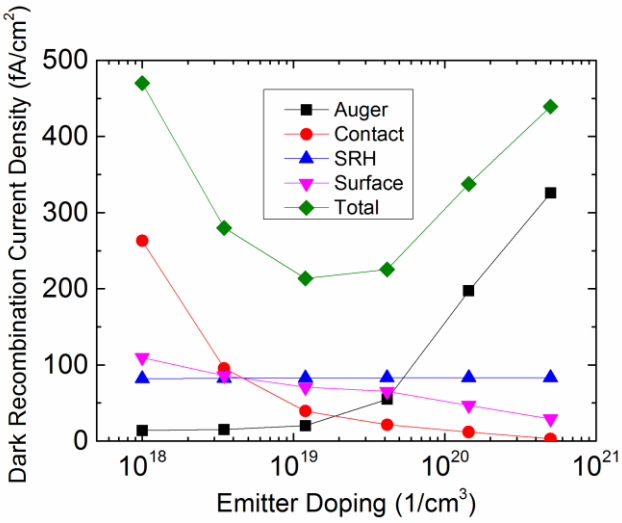

Figure 9. Saturation current competitive components in dark scenario. The bell shape exhibits a clear minimum point at doping peak concentration, $C_{em,pk}=1.2x10^{19}$ cm^{-3} explained in terms of contact and auger recombination trade-off in dark. SRH contribution increase is not appreciable considering scale size

On the one hand, an increase in $C_{em,pk}$ leads to a degradation of contribution of recombination at emitter contact in agreement with King [55]. This is ascribed to the stronger electrical field intensity at Si/Al interface for higher $C_{em,pk}$ that results into a reduction of minority carrier density at contact interface as Figure 10 confirms for open-circuit conditions under illumination. On the other hand, for higher $C_{em,pk,}$ Auger recombination contribution becomes stronger and predominant on the total recombination.

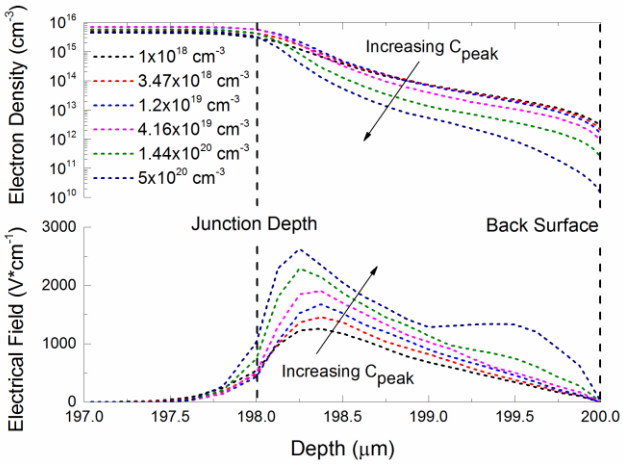

Figure 10. Comparison of electron density and electrical field intensity for different emitter doping peak concentrations in open-circuit condition under illumination in emitter region. Higher doping levels lead to stronger electrical field intensity in the junction depth and to lower minority carrier density values at Si/Al interface

A trade-off between the contact recombination and the Auger recombination leads to a minimum of the dark recombination current density for $C_{em,pk}$ = $1.2x10^{19}$ cm^{-3}, close to the value reported in [57]. It is worth noting that the $C_{em,pk}$ value observed for maximum η is higher due to the FF contribution. Indeed, FF increases with increasing $C_{em,pk}$ due to a reduction of the emitter sheet resistance. The highest calculated efficiency η is 22.3%. The marked difference from 24.2% [57] can be mainly ascribed to longer minority carrier lifetime, and higher passivation quality of silicon interfaces.

3.2.2 Geometry Parameters Analysis

In this section, we performed an extensive analysis of the influence of geometrical design parameters on the performance of the BC-BJ solar cell. The

geometrical considered parameters are: gap between emitter and BSF, BSF width (W_{bsf}), emitter width (W_e), and pitch (as defined in Figure 1). We considered the doping peak concentrations calculated in section 3.1, allowing to maximize η.

3.2.2.1 Gap and BSF Width

We performed simulations by changing the BSF region width W_{bsf} (Figure 1) and gap width at the same time, keeping constant the pitch (1000μm) and W_e (725μm). The assumed gap surface recombination velocity for carriers (SRV) is 25cm/s for base doping concentration according to [41].

Figure 11 shows that η decreases with increasing gap width, due to the remarkable reduction of FF. Evidently, the effect of the gap variation is reflected in a BSF and gap resistivity trade-off that explains the FF degradation for longer gap.

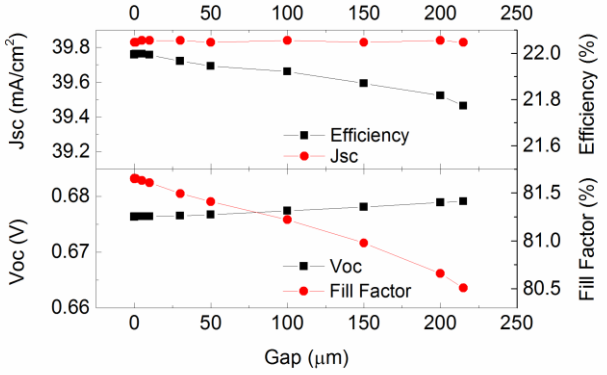

Figure 11. Simulated BC-BJ solar cell FOM as a function of gap. Efficiency and FF exhibit decreasing trend with increasing gap width.

However, we notice that J_{sc} has a negligible dependence on gap width. In fact, as Figure 12 shows, by changing the gap longitude there is a rise in SRH surface recombination rate contribution due to the absence of appreciable electrical field intensity at rear interface for wider gaps. In this case, the decrease in auger recombination loss is ascribed to wider gap, which leads to a smaller volume of highly doped BSF diffused region. Similarly, the increase in V_{oc} can be explained, but in this case, Auger recombination degradation becomes slightly more significant than surface recombination contribution.

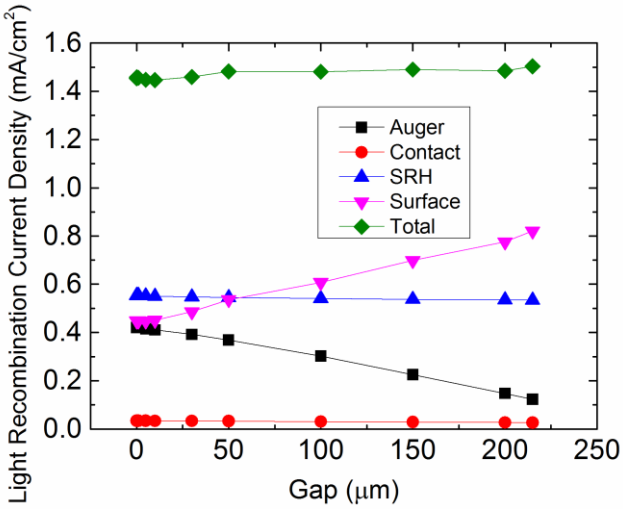

Figure 12. Recombination losses components under illumination in short-circuit condition explaining J_{sc} and V_{oc} trends. Auger recombination (black) exhibits a degradation that is compensated by surface defect recombination rise.

On the other hand, the trap-assisted recombination at the gap surface increases because of the absence of the electrical field (which prevents the high carrier density at the BSF interface). Evidently, the effects of surface defectiveness in rear interface expressed in terms of surface recombination velocity become critical for the gap region in agreement with reports in

[58],[59]: for relatively high defective interfaces, it is expected that surface defect recombination component becomes significant causing the degradation of J_{sc} and V_{oc}. In any case, a longer gap causes an efficiency degradation due to resistive and recombination losses confirming what observed in [60],[61].

3.2.2.2 Emitter Width

We performed simulations by changing the emitter width W_e (Fig.1) and that of the BSF region (W_{bsf}) at the same time, keeping the pitch constant (1000μm) as well as the gap width (5μm). In Figure 13, we plot FOM as a function of the W_e to pitch ratio (R). According to our hypotheses, a higher value of R implies both an increase of W_e and a decrease of W_{bsf}. We observed an increasing trend of η as R increases up to a value of 0.85, while a slight η reduction is observed for higher R values. Evidently, η enhancement is explained by J_{sc} rising trend [62] while η decrease by FF degradation. As Figure 14 shows, the decreasing trend of the total recombination under illumination for short-circuit conditions is mainly dictated by Auger and SRH recombination reduction at higher R, due to the higher value of $C_{bsf,pk}$ with respect to $C_{em,pk}$, hence confirming the J_{sc} increasing trend.

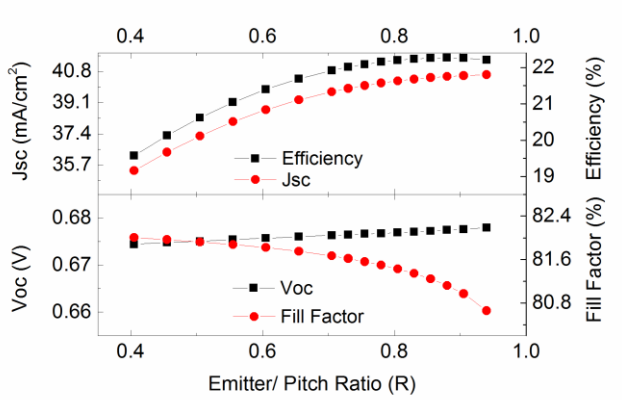

Figure 13. Simulated BC-BJ solar cell FOM as a function of emitter/pitch ratio (R). η exhibits slight a bell shape with a maximum value of 0.85. For lower ratio the trend follows J_{sc}, while for higher values FF degradation becomes prominent

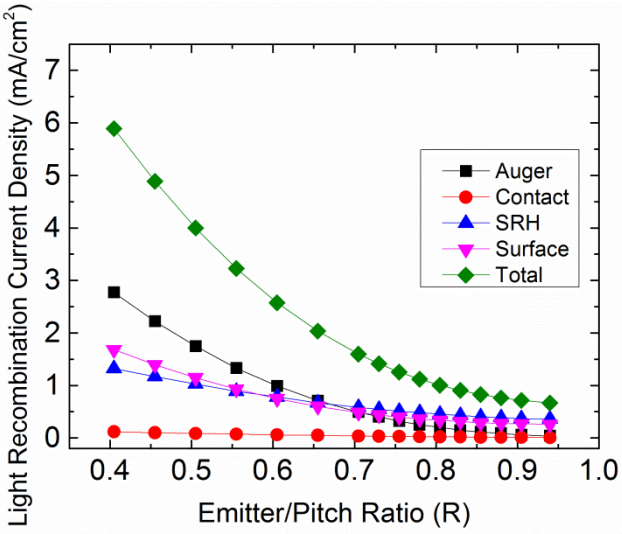

Figure 14. Recombination losses components under illumination in short-circuit scenario explaining J_{sc} trend as a function of emitter coverage ratio (R). R increasing means a general degradation of recombination contributors ascribed to electrical shadow effect reduction for larger emitters [49]

The observed FF degradation at higher R is ascribed to the higher emitter resistivity ($\rho_{em} = 42.76\Omega/\square$) with respect to the BSF resistivity ($\rho_{bsf} = 9.67\Omega/\square$). Therefore, a maximum η value at R of 0.85 is calculated. It is worth noting that, because the optimum R value depends on lateral transport resistance, it is influenced by bulk resistivity, emitter and BSF sheet resistance and therefore on the doping levels. This dependence explains the different R values reported in literature [63],[59].

3.2.2.3 Pitch

In order to understand the impact of the pitch over BC-BJ performance, we performed a set of simulations changing the pitch, keeping constant the emitter to pitch ratio (0.85) and the gap (5 μm). Figure 15 illustrates that η decreases with increasing pitch, mainly due to the FF lowering. Hence, an increase of the pitch causes a rise of series resistance because of the wider distance between contacts [64].

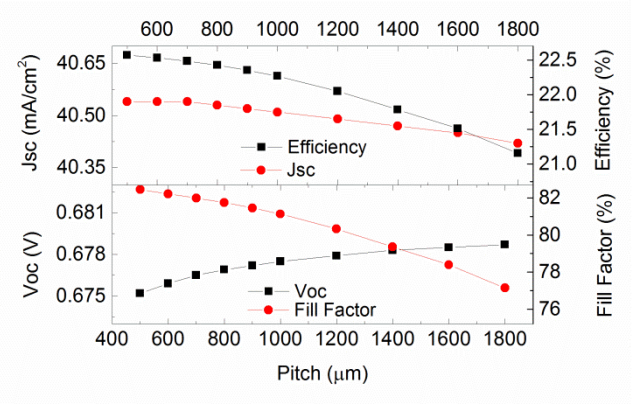

Figure 15. Simulated BC-BJ solar cell FOM as a function of pitch for an emitter coverage ratio of 0.85. η decreases as pitch length increases following FF trend. J_{sc} exhibits a decrease, while V_{oc} shows a negligible increment

The minimum simulated pitch size is 500µm, since lower pitch values would imply W_{bsf} smaller than the BSF contact size. Therefore, due to this design constraint, the minimum simulated pitch can be considered as the maximum efficiency pitch reported in [63],[59],[65]. It is worth noting that all recombination current density contributions increase with the pitch value, as shown in Figure 16. This is ascribed to the wider area affected by electrical shading [62]. The observed trend explains the slight decrease in J_{sc} illustrated in Figure 15. It is worth noting that in all experiments, contact size is assumed to be constant while the pitch changes. This means that contact recombination contribution is lower for larger pitches. While the impact on J_{sc} is negligible (less than 3% contact recombination contribution for optimum C_{bsf} on Figure 6), that on V_{oc} is more marked (around 20% contact recombination contribution for optimum C_e on Figure 9).

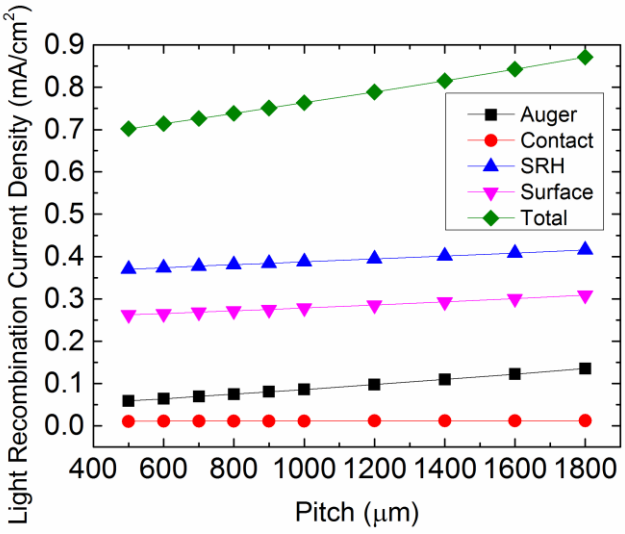

Figure 16. Recombination losses components under illumination in short-circuit scenario explaining J_{sc}. For the same emitter coverage ratio, R=0.85, recombination losses are almost constant for different values of pitch length

3.3 Conclusions

In this Chapter, It has been performed performed an extensive study of the impact of geometrical and doping parameters of BC-BJ solar cells on the main figures of merit, by means of a wide set of numerical simulations.

The results reveal that the efficiency curve as a function of doping exhibits a bell shape with a clearly identifiable maximum value for the three regions (BSF, FSF and emitter). The efficiency degradation for lower doping values is explained in terms of higher contact recombination for BSF and emitter, and in terms of higher SRH surface recombination for FSF. The efficiency decrease observed at higher doping values is explained in terms of higher Auger recombination for BSF and emitter, and in terms of SRH surface recombination losses for FSF. For the simulated solar cell, the values of peak doping that maximize η are: 4.16×10^{19} cm^{-3} for emitter, 1.44×10^{20} cm^{-3} for BSF and 3.48×10^{18} cm^{-3} for FSF.

Additionally, we observed efficiency degradation as a result of wider gap region, due to the resistive losses and the SRH surface recombination losses in this region. The maximum efficiency as a function of emitter/pitch ratio R is obtained for R=0.85. The efficiency decrease for smaller R is explained in terms of higher recombination losses (Auger and SRH recombination) in electrical shadowed regions, due to the reduced p-n junction electrical field intensity, which causes a higher minority carriers density. The efficiency decrease for higher R is ascribed to larger resistive losses in the emitter region compared to BSF. Finally, we also observed efficiency degradation for larger pitch values, due to the FF decrease caused by the increase of the resistive losses.

Four

4 Understanding the impact of front-side texturing and doping on the performance of c-Si IBC solar cells

In this Chapter, a TCAD-based simulation platform has been developed to account accurately and in detail the optical and passivation mechanisms of front texturization. Its validation has been carried out with respect to a novel homo-junction IBC c-Si solar cell based on ion implantation and epitaxial growth, comparing measured and simulated R, T, IQE, EQE spectra and current density-voltage characteristics. As a result of the calibration process, the opto-electrical losses of the investigated device have been identified quantitatively and qualitatively. Then, an optimization study about the optimal front surface field (FSF) doping, front-side texturing morphology, and rear-side geometry has been performed. The proposed simulation platform can be potentially deployed to model other solar cell architectures than homo-junction IBC devices (e.g. passivated emitter rear cell, passivated emitter rear locally diffused cell, hetero-IBC cell) Simulation results show that a not-smoothed pyramid-textured front interface and an optimal FSF doping are mandatory to minimize both the optical and the recombination losses in the considered IBC cell and, consequently, to maximize the conversion effi-

ciency. Similarly, it has been showed that recombination losses are affected more by the doping profile rather than the surface smoothing. Moreover, the performed investigation reveals that the optimal FSF doping is almost independent from the front texturing morphology and FSF passivation quality. According to this result, it has been demonstrated that an IBC cell featuring an optimal FSF doping does not exhibit a significant efficiency improvement when the FSF passivation quality strongly improves, proving that IBC cell designs based on low-doped FSF require a very outstanding passivation quality to be competitive. Deploying an optimization algorithm, the adoption of an optimized rear-side geometry can potentially lead to an efficiency improvement of about 1%abs as compared to the reference IBC solar cell. Further, by improving both emitter and c-Si bulk quality, a 22.84% efficient solar cell for 280-μm thick c-Si bulk was simulated.

4.1 Introduction

As it was noted in Chapter 1, both the front and the rear side still represent significant sources of optical and electrical losses even in IBC solar cells. To this purpose, PV research community is focusing on the study of innovative technological solutions aimed to minimize these losses. Concerning the front side, different texturization techniques, anti-reflective coatings (ARCs) depositions and front surface field (FSF) formation processes have been proposed to reduce both optical and recombination losses. As matter of fact, the analysis of novel texturing processes in high-efficiency solar cells has been elucidated [66]–[71]. On one hand, in fact, some papers have shown clear improvements in case of pyramid-textured or nano-textured structures mainly due to a reduction of front-side optical losses [66], [68], [69]. On the other

hand, some works have highlighted potential improvements in case of smoothed texturization due to a significant reduction of front-side recombination losses [70], [71]. This reveals the existence of a trade-off between two competitive mechanisms, such as the recombination at front side and the light management. In addition, other contributions have discussed the optimization of the FSF in IBC solar cells in terms of recombination losses, lateral resistance losses and UV-light stability [72][56]. Concerning the rear side of IBC solar cells, the analysis and the optimization in terms of rear geometry and process parameters is typically done by means of numerical simulations, which aid cell design and fabrication through a detailed loss analysis [49], [63], [73]–[77]. Commonly, most of simulation-based works have employed a two-step simulation approach [26], [78]. First, an optical model, typically based on ray tracing (RT) or rigorous Maxwell's solvers for devices with nano-textured features, derives the generation profile of electron-hole pairs within the device. Second, an electrical model based on drift-diffusion uses as an input the calculated optical generation profile [26], [78]. For the sake of simplicity, this approach typically involves in each step the use of different simulation domains. In fact, the optical simulation is carried out on an element that features textured surfaces with the aim of properly accounting for the optical situation within the silicon. The electrical simulation instead usually is set up on an approximated simulation domain that simply features planar surfaces. Obviously, the usage of different simulation domains requires the adoption of some correctives with the aim of properly importing the calculated optical generation profile in the equivalent planar electrical domain accounting for the effect of texturing also in the electrical model [26]. In fact, such simulation methodology leads to a loss of accuracy when evaluating in detail optical and electrical mechanisms of the FSF.

In this Chapter, we present a detailed TCAD-based opto-electrical model developed for the study and the optimization of a fabricated reference IBC c-Si solar cell. Differently from the abovementioned two-step modelling approach, our simulation framework involves a two-dimensional (2-D) geometrical model that includes the exact modeling of a pseudo-random pyramids front texturing morphology both in the optical and electrical simulations. As a consequence, our modelling approach allows directly and properly accounting for the optical effect of textured front side, transport and recombination mechanisms, without the need to approximate the optical generation profile under an equivalent planar simulation domain and to use correction factors in the considered physical models [26].

The developed opto-electrical device model has been firstly calibrated and validated with respect to a fabricated reference IBC solar cell. Reflectance (R), transmittance (T), internal quantum efficiency (IQE), external quantum efficiency (EQE) and electrical measurements have been used for the calibration process. Therefore, a detailed analysis of the opto-electrical losses has been realized for the reference device. Then, the calibrated device model has been deployed to perform an extensive simulation study of the impact of different FSF doping levels and front-side texturing morphologies on the IBC solar cell performance. Such an investigation has been also carried out by considering different front surface passivation qualities. Finally, the developed device model has been used to optimize the rear-side geometry of the reference IBC solar cell.

4.2 Experimental

Reference IBC solar cell was based on FZ *n*-type *c*-Si wafer, 280-μm thick and resistivity of 2.5 Ω·cm. Such device fabricated through a novel self-aligned process which combines phosphorous ion implantation for the FSF and the back surface field (BSF), and epitaxial growth of the boron-doped emitter [79][80]. The front side of our solar cell consists of a textured interface with random pyramids, while the rear side is planar (Figure.1). Both interfaces are covered by thermally-grown SiO_2 and plasma-enhanced chemical vapour deposited SiN_x layers in the double role of passivation stack and ARC. Metallic contacts are realized by evaporated 2-um thick Al fingers, opportunely placed in the middle of the emitter and of the BSF (see Section 4.3 for details on geometry). Two 3×3 cm^2 solar cell samples were fabricated: the first one features a FSF (*FSF* sample), exhibiting a sheet resistance equal to 250 Ω/□, while the second is not endowed with the FSF (*NO-FSF* sample). At the rear side of these devices, the gap between the BSF and the emitter was self-defined during the process and is around ~1.5 μm. Defining pitch the distance between the starting points of two consecutive emitters, the two solar cell samples featured a 1-mm wide rear pitch.

The morphological analysis of the front textured interface was performed by means of Scanning Electron Microscopy (SEM, Philips XL-50) and Atomic Force Microscopy (AFM, NT-MDT nTegra NT-MDT) pictures with the aim of extracting the statistical distribution of the height and overlap of the random pyramids. Wavelength-dependent R and T were measured by a Perkin Elmer Lambda 950 spectrophotometer in the wavelength range between 300 and 1200 nm. Thickness, refractive indexes and extinction coefficients of SiO_2 and SiN_x ARC layers were extracted by means of a J. A. Woollam spectroscopic ellipsometer. Current density-voltage (J-V) measurements were performed with a continuous class AAA Wacom solar sun simulator, while EQE meas-

urements were extracted through an in-house built setup that includes a Newport monochromatic illuminator. Quasi steady-state photo-conductance technique was used to evaluate the effective minority carrier lifetime. The phosphorus implanted and boron epitaxial grown doping profiles were extracted from electrochemical capacitance (ECV) measurements. The contact resistance of the related aluminium-coated BSF or emitter layers, deposited on *c*-Si FZ wafers of opposite polarity, was measured by means of Transmission Line Method (TLM).

4.3 Modeling Approach

The modelling approach adopted in this work involves the usage of the same simulation domain, whose 2-D cross-section is shown in Figure.1. In particular, we simulate both optically and electrically a front texturing based on pseudo-random pyramids with the aim of accurately preserving the information related to its effect on light management, passivation and carriers transport. Our modelling approach requires a more extended simulation domain for the optical simulation and a finer mesh in the front textured morphology for electrical simulation as compared to the equivalent flat structure. Nevertheless, several advantages by far counterbalance the slightly greater computational effort: (i) the more accurate distribution of the photo-generated electron-hole pairs within the device, (ii) the proper modelling of the free-carrier absorption, and (iii) the better representation of transport and recombination mechanisms occurring at the textured front side of the solar cell. Based on the proposed approach and according to the geometrical and physical parameters of the reference IBC solar cell, we deployed a numerical

TCAD simulator [28] for running our developed opto-electrical device model.

4.3.1 Modelling of solar cell geometry and doping concentration profiles

The geometrical model used in the optical and electrical simulations has been developed according to the features of the reference IBC solar cell. The illustration of the considered 2-D simulation domain, representing the smallest element of symmetry of the reference cell, is reported in Figure.1. The width of the simulation domain has been set to the half of the rear pitch (i.e. 500 µm). As the BSF-to-pitch ratio is 20%, the emitter width and the BSF width have been set to 400 µm and 100 µm, respectively. As a result of the previously mentioned process [80]**¡Error! No se encuentra el origen de la referencia.**[79], based on isotropic etching of the silicon, the gap between the emitter and the BSF has been modelled with an arc of circumference having a radius of 1.5 µm. Air/cell front interface is texturized by random pyramids, while cell/air rear interface is flat. Both interfaces are covered by SiO_2/SiN_x ARC stack.

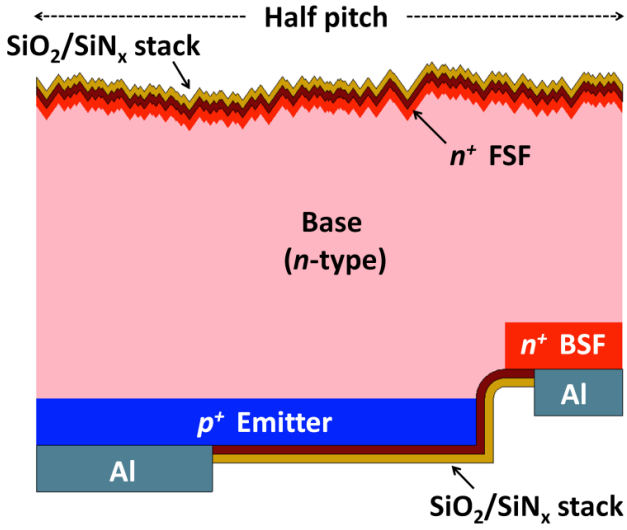

Figure.1: 2-D cross-section of the considered simulation domain (dimensions are not to scale).

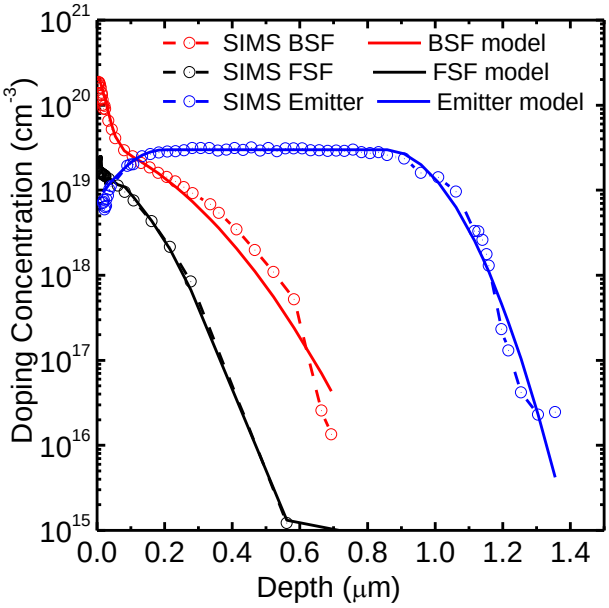

Figure.2: ECV-based and modeled doping concentration profiles. For BSF and FSF doping profiles cerf functions are used. For emitter doping profile, $3x10^{19}$ cm^{-3} is kept constant within 0.2 and 0.85 µm and gaussian functions describe doping concentration changes near emitter boundaries.

To properly simulate the mechanisms related to highly doped regions such as BSF, FSF and emitter, the corresponding doping concentration profiles have been modeled by analytical functions according to ECV measurements, as shown in Figure.2. The FSF, BSF and emitter regions were found to be 0.6-µm, 0.8-µm and 1.4-µm deep, respectively. In case of FSF, a complementary error function (cerf) was deployed with diffusion depth and surface concentration parameters set to 0.2 µm and 2 x 10^{19} cm^{-3}, respectively. For BSF doping profile, a superposition of two cerf was used with parameters 0.04 µm and 2 x 10^{20} cm^{-3} for the first cerf and 0.3 µm and 4 x 10^{19} cm^{-3} for the second. Differently, for the doping profile of the emitter, we mimicked the nature of doping profile of the epitaxial grown layer: a constant doping value within the deposited thickness was set to 3 x 10^{19} cm-3 while the boron inversion layer at the surface and the diffusion tail in the bulk were modelled with two independent gaussian profiles, whose peak values (again 3 x 10^{19} cm^{-3}) were positioned at a depth of 0.2 µm and 0.85 µm, respectively. The front texturing has been modelled by a sequence of triangles with a fixed base angle of 54.7°, which is related to the adopted wet-alkaline etching process. It is worth noting that the statistical distributions of triangles' height and overlap were extracted from measured AFM images, as shown in Figure.3 for the height distribution. Then, the extracted statistical distributions have been fitted through analytical probability distribution functions, as the skewed normal distribution function reported in Figure.3.

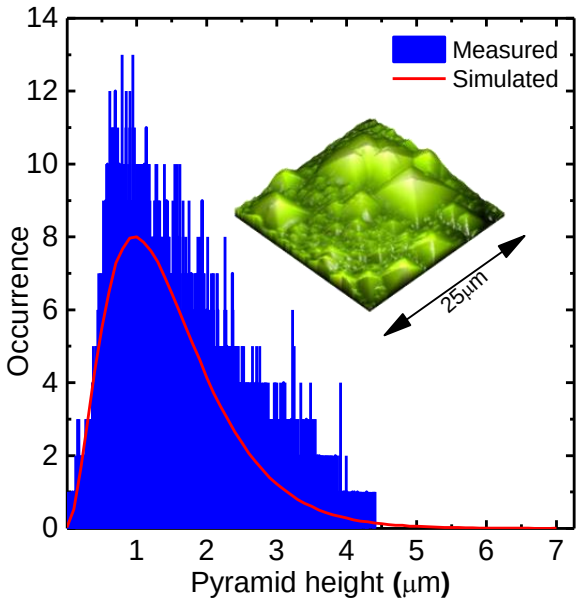

Figure.3: Measured random pyramids height distribution (blue) from an AFM image (inset) and corresponding fitting distribution (red).

Finally, by exploiting the potential of simulating in detail front texturing mechanisms, we have modified the morphology of the front interface by rounding pyramid tips and valleys with the aim of studying the effects of the smoothing process over typical random pyramids texturization. Accordingly, the obtained fitting statistical distributions have been used to generate a realistic pseudo-random pyramids front morphology for the considered 2-D simulation domain as a function of a parameter called R_{text} (see Figure.4). In particular, R_{text} represents the radius of the semi-circumference used to model each peak or valley of the front texturing structure when a smoothing process is applied over the typical random pyramids texturization [71]. Therefore, in our modelling it can range from 0 (i.e. corresponding to a not-

smoothed as-etched pyramids structure) up to an ideal infinity (i.e. corresponding to a flat front interface), as shown in Figure.4.

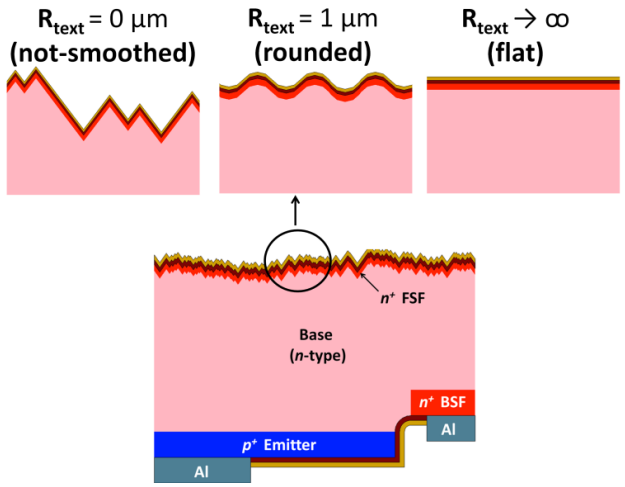

Figure.4: Modeling of the front texturing morphology as a function of Rtext, radius of curvature used to describe tip and valley of each pyramid.

4.3.2 Optical and electrical models

The optical simulation has been performed by means of Monte Carlo ray tracing technique [28], [30], [31] in combination with Transfer Matrix Method (TMM) boundary conditions. In this way, we could properly model within the TCAD software the interference mechanisms occurring at front and back thin SiO_2/SiN_x ARC stack [81]. Vertical interfaces to the left hand and to the right hand of the simulated domain have been modeled as perfectly reflecting layers to prevent the escaping of light from lateral surfaces and to ensure the periodicity of the symmetry element. The measured reflectance has been used to tune the thickness of SiO_2 and SiN_x layers for both front

and back ARC stacks by matching the destructive and constructive interference conditions. Measured refractive indexes and extinction coefficients of SiO_2 and SiN_x ARC layers have been also considered in the model.

It is worth pointing out that TMM approximation assumes that transmitted rays at both the front and the rear ARC stacks is not back-reflected in the bulk. Such a simplification does not allow taking into account the effect of multiple reflections within the device, thus potentially leading to a considerable underestimation of long-wavelength photons scattering. To overcome this issue, two so-called screen layers have been set in air 1 μm away from the top and from the bottom of the modelled structure. These layers do not affect primary-reflected rays and become effective only for wavelengths longer than a certain threshold value. Basically, rays escaped from the front and/or the rear side of the structure can be forcibly sent back in the structure with a certain probability and with an angle dictated by Snell law. It is clear that we used the screen layers merely for fitting purposes. Setting the threshold wavelength at 1000 nm, the best probability was found to be 0.8 (e.g. 80 over 100 escaped rays for wavelength longer than 1000 nm were sent back in the structure).

Based on the proposed approach, the 2-D map of the optical generation rate inside the considered device has been then calculated assuming direct illumination with a standard AM1.5G spectrum (1000 W/m^2) [47]. Moreover, free-carrier absorption (FCA) has been modelled[82][82][82][83][83][83], assuming the doping concentration as the carrier concentration [82].

The electrical simulation has been based on the drift-diffusion model. According to the proposed opto-electrical modelling approach, the 2-D map of the photo-generated electron-hole pairs within the silicon obtained from the optical simulation is directly deployed into the electrical model without the

need for any further adjustment. Moreover, an *ad-hoc* calibration of physical models implemented in the numerical TCAD simulator [28] has been performed according to sets of state-of-the-art parameters [26], [78] and/or several measured parameters (see Table 2 Summary of the most relevant physical models and parameters used in the electrical model.). Among these, electrical and quantum efficiency measurements of the fabricated reference IBC cell have been used to calibrate the doping-dependent trap-assisted Shockley-Read-Hall (SRH) bulk and surface recombination models related to defects in the silicon substrate and at passivated interfaces. In particular, the doping-dependent model for the bulk SRH lifetime adopts the so-called Scharfetter relation [28]:

$$\tau_{SRH} = \frac{\tau_{max}}{1 + \left(\frac{N_{A,D}}{N_{ref}} \right)^{\gamma}} \qquad (1)$$

where τ_{max} has been set to 2 ms, which is equal to the measured bulk minority carrier lifetime, and $N_{A,D}$ represents the acceptor or donor doping concentration, respectively. Then, N_{ref} and γ have been used as calibration parameters to model the SRH recombination lifetime in the different doped regions of the simulated solar cell, such as FSF, BSF and emitter.

Table 2 Summary of the most relevant physical models and parameters used in the electrical model.

Model parameter	**This work**
Free carrier statistics	Fermi-Dirac [28]
Bandgap narrowing	Schenk [33]

Mobility	Klaassen [35]
Intrinsic recombination: Auger and radiative	Richter [6]
Intrinsic carrier density	Altermatt [38] (9.65×10^{9} cm^{-3} at 300 K)
Metal/Si interface recombination velocity	$1x10^{7}$ cm/s (thermal velocity)
SRH lifetime	Calibration of Scharfetter relation [28] from measurements (τ_{max} = 2 ms for bulk lifetime)
Surface SRH recombination velocity at passivated interfaces	Calibration of Altermatt's model [41] from measurements
Contact resistance	Calibration of a distributed resistance model from TLM measurements: - 3.9 $m\Omega\cdot cm^2$ for specific contact resistivity of *p*-contact - 2.2 $m\Omega\cdot cm^2$ for specific contact resistivity of *n*-contact
Finger and bus bar resistance	Distributed model: - 2.8 $\mu\Omega\cdot cm$ for Al metal resistance

4.4 Results

4.4.1 Validation of the opto-electrical device model

The developed opto-electrical device model was validated by comparing simulated J-V characteristics, EQE and IQE curves, R and T spectra with their measured counterparts for the two considered types of solar cells (with and without FSF, respectively).

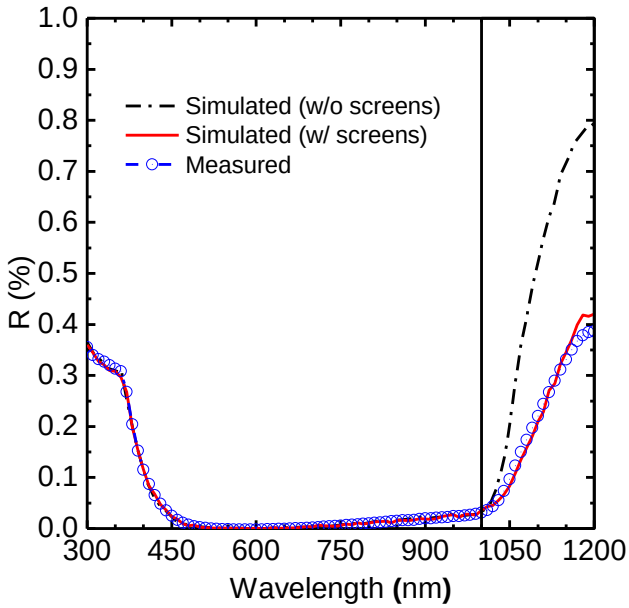

Figure.5: Comparison between measured and simulated reflectance (R) spectra with and without corrective screen layers in the optical model.

In Figure.5 the comparison between measurements and simulations in terms of R spectra of *FSF* cell is reported for two cases. The first case refers to the use of the approximated optical model described in Section 3.2 without the application of the two corrective *screen layers*. In this case, a good agreement between simulated and measured R can be observed only for wavelengths within the primary reflectance range (i.e., from 300 up to 1000 nm), while, as expected, a significant overestimation of the simulated reflectance is obtained in the longer wavelength range. This clearly indicates an inaccurate boundary condition in the simulation environment. The second case, instead, refers to the application of the corrected optical model accounting for the effect of multiple reflections inside the silicon by means of the aforementioned

screen layers. In the latter case, a very good agreement between simulations and measurements can be observed in the entire wavelength range of interest.

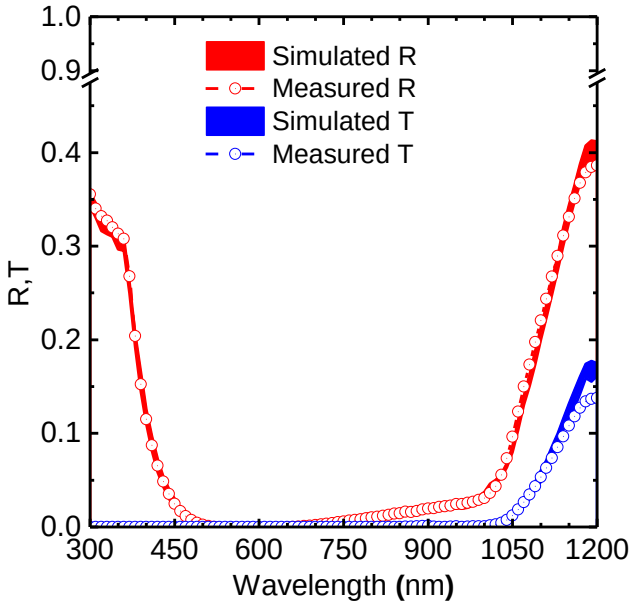

Figure.6: Reflectance (R) and transmittance (T) spectra of 100 simulations (red and blue areas, re-spectively) compared to measurements, confirming statistical robustness.

Moreover, Figure.6 shows the comparison between measured and simulated R, T spectra. Such spectra are related to one hundred simulations based on different pseudo-random not-smoothed pyramidal front texturing generated from the reference statistical distribution (see Section 3.1). A good matching is observed, which confirms the high statistical robustness of the proposed optical model. After having validated our optical approach, we proceeded with the electrical simulations.

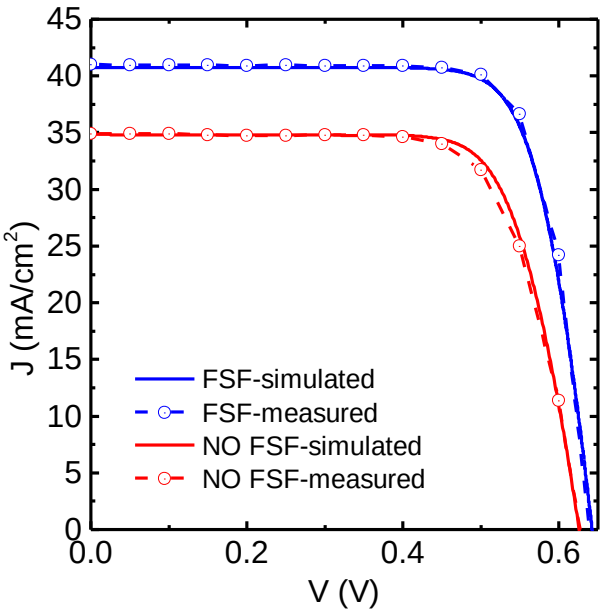

Figure.7: Measured and simulated illuminated J-V curves for the reference IBC solar cells with and without FSF.

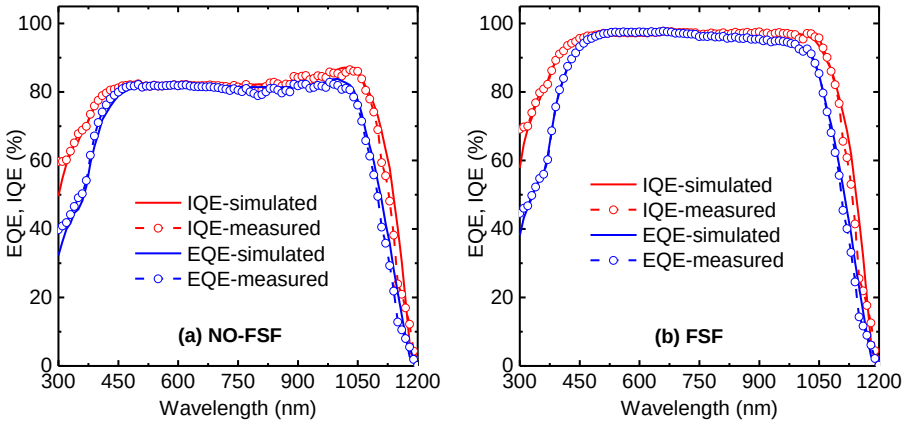

Figure.8: Measured and simulated IQE and EQE of the reference IBC solar cell without (a) and with (b) FSF

Figure.7 shows the comparison between measured and simulated J-V curves under AM1.5 illumination for the two reference samples; while Figure.8 illustrates the same comparison but in terms of IQE and EQE. In addition, Table 3 External parameters of the two measured and simulated solar cells (FSF cell and NO-FSF cell). compares the external parameters, i.e. short-circuit current density (J_{sc}), open-circuit voltage (V_{oc}), fill factor (FF) and conversion efficiency (η), of both simulated and measured solar cells. Overall, a good agreement has been achieved between simulated and experimental data for both considered samples. However, as noticeable in both Figure.7 and Table 3 External parameters of the two measured and simulated solar cells (FSF cell and NO-FSF cell)., in case of *NO-FSF* sample the FF value obtained from the simulation does not perfectly match with the experimental data, leading to a 0.6%$_{abs}$ overestimation of the efficiency. This is due to some additional resistive losses related to issues with metallic contacts fabrication in the *NO-FSF* sample. These losses are neglected in the following analysis when considering *NO-FSF* designs.

Table 3 External parameters of the two measured and simulated solar cells (FSF cell and NO-FSF cell).

	FSF cell		**NO-FSF cell**	
	measured	simulated	measured	simulated
J_{sc} [mA/cm^2]	41.0	40.8	34.5	34.3
V_{oc} [mV]	639	642	627	628
FF [%]	76.9	76.4	72.3	75.8
η [%]	20.1	20.0	15.7	16.3

The developed opto-electrical model allows quantifying and localizing both optical and electrical losses occurring inside the considered devices. From the optical perspective and in the wavelength range of interest, R, T, free-carrier absorption (FCA) in doped *c*-Si layers, optical parasitic absorption in the front SiN_x layer and at the rear metallic interfaces for both emitter and BSF contacts, and recombination losses are shown in Figure.9 for the simulated IBC *FSF* solar cell. As every loss contribution has been estimated in terms of *implied* current density (in mA/cm^2) with reference to the ASTM 1.5G spectrum [47], it is clear that reflectance and recombination losses represent the main loss components in such simulated IBC solar cell. With J_{opt} we define the sum of all parasitic implied current densities related to R, T, FCA in doped *c*-Si layers, absorption in the SiN_x layer and at the rear metallic interfaces for both emitter and BSF contacts.

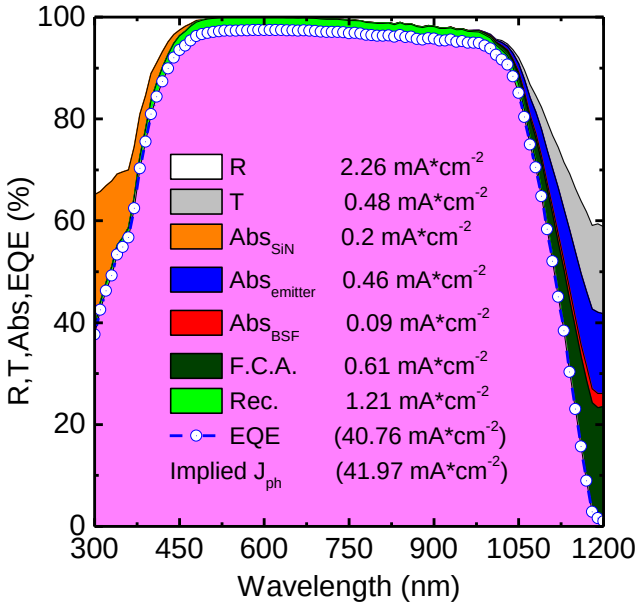

Figure.9: Estimated losses of the simulated IBC solar cell endowed with FSF: R, T, FCA in c-Si doped layers, parasitic absorption (Abs) in front SiNx layer and rear metallic contacts, and recombination (Rec). Losses are reported in terms of mA/cm2.

For the simulated *FSF* device, J_{opt} is 4.1 mA/cm^2, corresponding to 8.9% of the J_{in}, which represents the incident photocurrent density (J_{in} = 46.19 mA/cm^2 in the wavelength range between 300 nm and 1200 nm). For the same modelled device, the breakdown of dark saturation current density (J_0) and light recombination current density (J_{rec}) contributions, describing recombination losses in each region of the simulated device [53], are reported in Figure.10 and Figure.11, respectively.

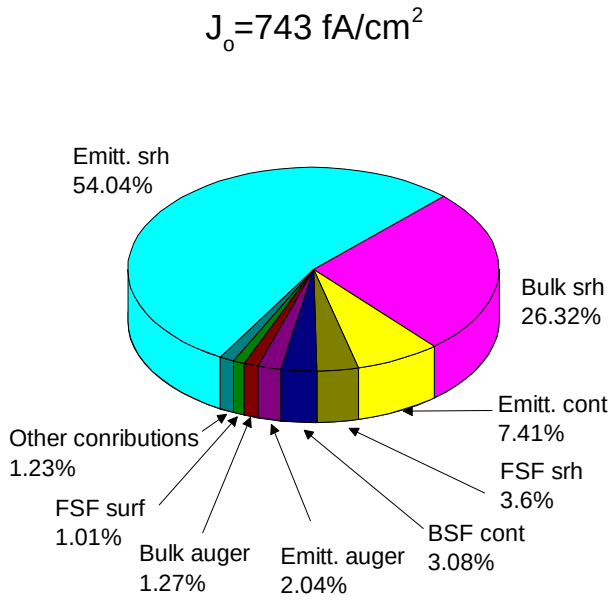

Figure.10: Breakdown of the main J0 contributions from the dark simulation of the considered FSF IBC solar cell.

It is found that defect-related SRH bulk and emitter losses dominate losses in our IBC *FSF* solar cell. Table 4. Dark saturation current density (J0), light recombination current density (Jrec), and optical losses in terms of implied current density Jopt for the two modelled FSF and NO-FSF reference IBC solar cells. reports, for both *NO-FSF* and *FSF* simulated devices, two calculated contributions: (i) the optical losses in terms of percentages of implied current density J_{opt} with respect to J_{in} and (ii) the total and front recombination losses calculated in dark and light conditions in terms of implied current density J_0 and J_{rec}, respectively. When considering the *NO-FSF* device, the main recombination losses occur at the front side.

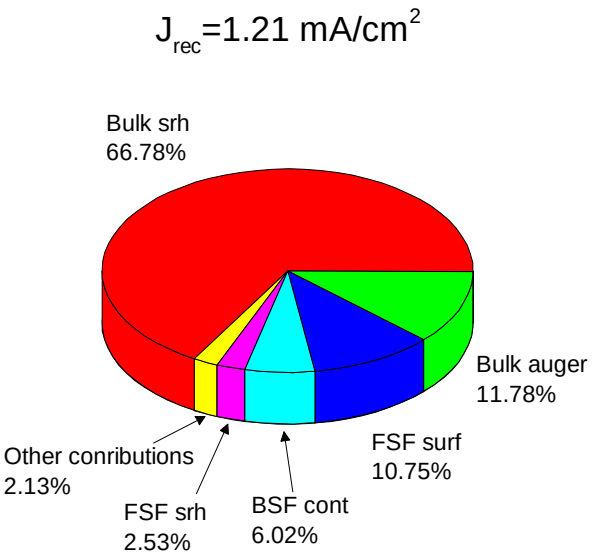

Figure.11: Summary of the main Jrec contributions from the light simulation of the considered FSF IBC solar cell.

Therefore, the results of this detailed loss analysis demonstrate that, in addition to the rear-side optimization, the design of the front side in terms of FSF doping and texturing morphology can be crucial in the considered IBC solar cell to improve the trade-off between the competitive optical and recombination mechanisms. Finally, it is worth noting that the small difference observed in Table 4. Dark saturation current density (J0), light recombination current density (Jrec), and optical losses in terms of implied current density Jopt for the two modelled FSF and NO-FSF reference IBC solar cells. in terms of optical losses between the two considered devices can be ascribed to the slightly higher FCA losses occurring in the FSF cell.

Table 4. Dark saturation current density (J0), light recombination current density (Jrec), and optical losses in terms of implied current density Jopt for the two modelled FSF and NO-FSF reference IBC solar cells.

	***FSF* cell**	***NO-FSF* cell**
$J_{0,TOT}$ [fA/cm^2]	743	1770
$J_{0,front}$ contribution	5%	62%
$J_{rec,TOT}$ [mA/cm^2]	1.21	6.97
$J_{rec,front}$ contribution	13%	91%
J_{opt} contribution	8.9%	8.8%

4.4.2 Impact of front-side texturing and doping on IBC solar cells performance

The front-side texturing and the FSF doping affect the performance of the reference IBC solar cells. We have analyzed these aspects with a set of simulations considering different front texturing morphologies and FSF doping levels. In particular, we have varied the R_{text} parameter from 0 (i.e. not-

smoothed pyramidal front morphology) up to an ideal infinity (i.e. flat front surface). Also, we have changed the FSF peak doping concentration (C_{peak}) from $1\times10^{15}cm^{-3}$ up to $1\times10^{20}cm^{-3}$ with a fixed junction depth of 0.6 µm (see Section 3.1). This sensitivity study is graphically elucidated in the following dual-panel Figure.12-18, in which the left-hand (right-hand) side panel reports the trend as function of C_{peak} (R_{text}) and using R_{text} (C_{peak}) as sweeping parameter. Instead of using, for example, contour plots, we opted for this reporting approach to clearly highlight the main effect of the FSF doping versus the surface texturing and vice versa. Finally, we have further refined our analysis by also varying the passivation quality of the front surface in terms of its front surface recombination velocity (SRV_{front}). All the other parameters of the device model have been kept constant in this analysis, while all the simulations have been performed in both dark and illuminated conditions with the aim of better understanding the existing trade-off between the competing optical and recombination mechanisms. Accordingly, optical and recombination losses as well as the external parameters of the solar cells have been extracted from simulations as a function of FSF doping level and front-side texturing morphology.

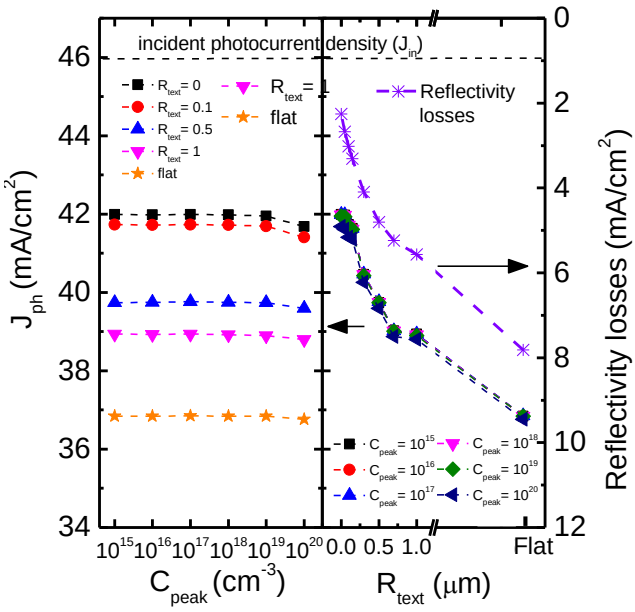

Figure.12: Jph as a function of FSF Cpeak (left) and Rtext (right), and reflectivity losses as function of Rtext (right). Jin represents the incident photocurrent density, which is equal to 46.19 mA/cm2 in the wavelength range between 300 nm and 1200 nm.

The trend of the optical losses can be observed in Figure.12, which shows the calculated photo-generated current density ($J_{ph} = J_{in} - J_{opt}$). In addition, on the right-hand side panel, a secondary y-axis is reported with reflectance losses in terms of implied photo-current density. On the left-hand side, we note that the optical losses and, consequently, the J_{ph} are almost constant for different FSF C_{peak}, slightly decreasing only for highest simulated C_{peak} values owing to greater FCA. On the contrary, on the right-hand side of Figure.12, we recognize a strong degradation of J_{ph} as R_{text} increases, i.e. as the front texturing becomes smoother. Consequently, also reflectance losses greatly increase from 2 mA/cm^2 to almost 8 mA/cm^2 as we simulated smoother and smoother front surface of our devices.

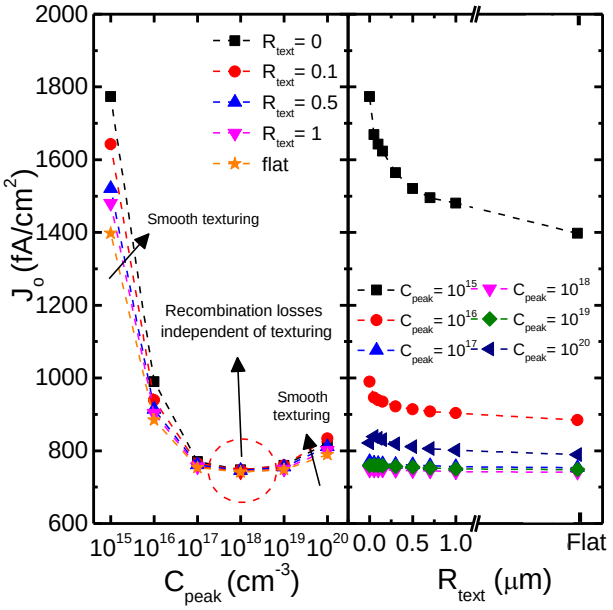

Figure.13: J0 as a function of FSF Cpeak (left) and Rtext (right).

The recombination losses are reported in Figure.13 and Figure.14, where the trends of J_0 and J_{rec} are shown, respectively. According to what already reported in [32], J_0 and J_{rec} curves as a function of FSF C_{peak} show a reversed bell shape leading to an optimal FSF C_{peak} around 1×10^{18} cm^{-3}. Conversely, both J_0 and J_{rec} exhibit a certain dependence on the R_{text}, especially for FSF C_{peak} values not around the calculated optimal value.

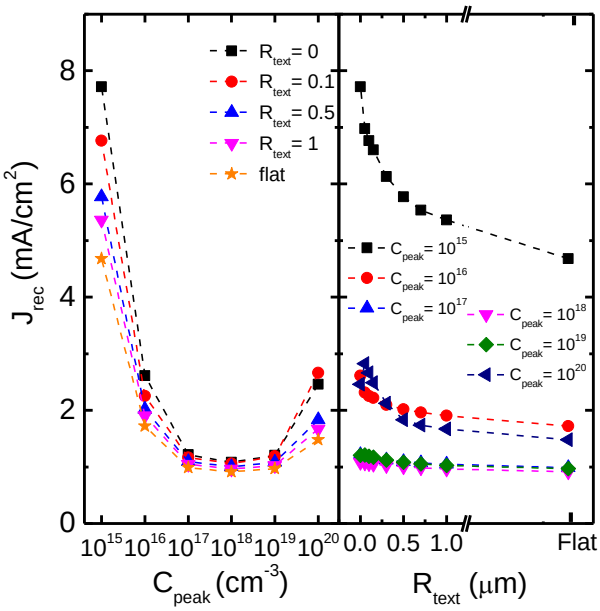

Figure.14: Jrec as a function of FSF Cpeak (left) and Rtext (right).

The variations of J_0 and J_{rec} within the FSF C_{peak} range are ~1000 fA/cm^2 and ~7 mA/cm^2, respectively, while such variations for R_{text} range are comparatively smaller (~200 fA/cm^2 and ~2 mA/cm^2, respectively). Continuing with this sensitivity study, Figure.15 and Figure.16 illustrate, respectively, the J_{sc} and V_{oc} trends. For both external parameters, we notice bell-shaped curves as function of the C_{peak} and regardless the R_{text}. The maxima of these bell trends (J_{sc} = 40.91 mA/cm^2 and V_{oc} = 0.646 V) are realized at the same optimal FSF C_{peak} (1×10^{18} cm^{-3}) that reduces both J_{rec} and J_0 (see Figure.13 and Figure.14).

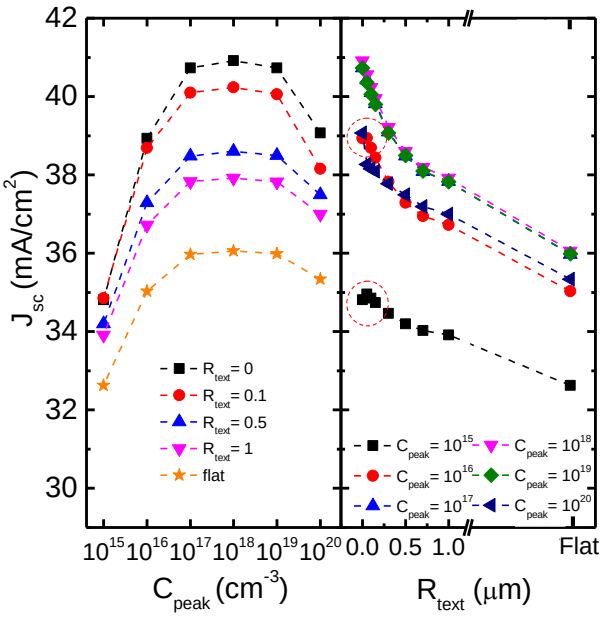

Figure.15: Jsc as a function of FSF Cpeak (left) and Rtext (right). In the right-hand side panel, the small increase of Jsc at low Rtext in case of low FSF Cpeak is highlighted.

On the other hand, J_{sc} exhibits a decreasing trend with the increasing of R_{text} owing to the smoother the front texturing; while the trend of V_{oc} as function of R_{text} varies for different FSF C_{peak} values. In particular, V_{oc} increases with R_{text} for lower C_{peak} (1×10^{15} and $1\times10^{16}cm^{-3}$), and slightly decreases in the other cases. Similarly, a small increase of J_{sc} at low R_{text} can be appreciated in case of low FSF C_{peak}. This is due to the compromise between light trapping and recombination mechanisms (see Section 5.2).

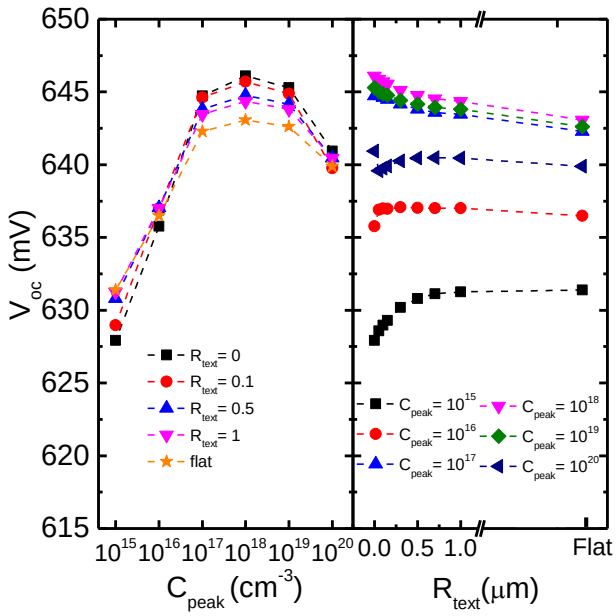

Figure.16: Voc as a function of FSF Cpeak (left) and Rtext (right).

The trend of FF values is reported in Figure.17, where we can observe that (i) at low C_{peak} (up to $1x10^{18}$ cm^{-3}) FF markedly increases as C_{peak} increases, (ii) at high C_{peak} (above $1x10^{18}$ cm^{-3}) FF saturates and (iii) FF generally increases when applying more rounded pyramid texturization. It is worth noting that the improvement of lateral transport within the FSF is reached when C_{peak} and R_{text} increase by enhancing, respectively, carrier conductivity and interface collection path. Thus, FSF sheet resistance is reduced as C_{peak} and R_{text} increase.

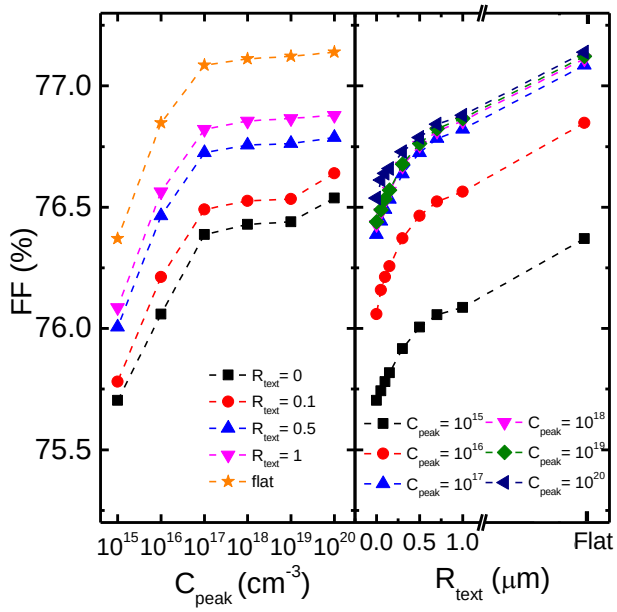

Figure.17: FF as a function of FSF Cpeak (left) and Rtext (right).

Descending from the abovementioned trends of J_{sc}, V_{oc} and FF, Figure.18 shows η as a function of FSF C_{peak} and R_{text}. We can easily note that η shows similar behaviour to J_{sc}: a bell-shaped trend as a function of FSF C_{peak} with an optimal C_{peak} around 1×10^{18} cm^{-3} and a decreasing trend as the front texturing becomes smoother.

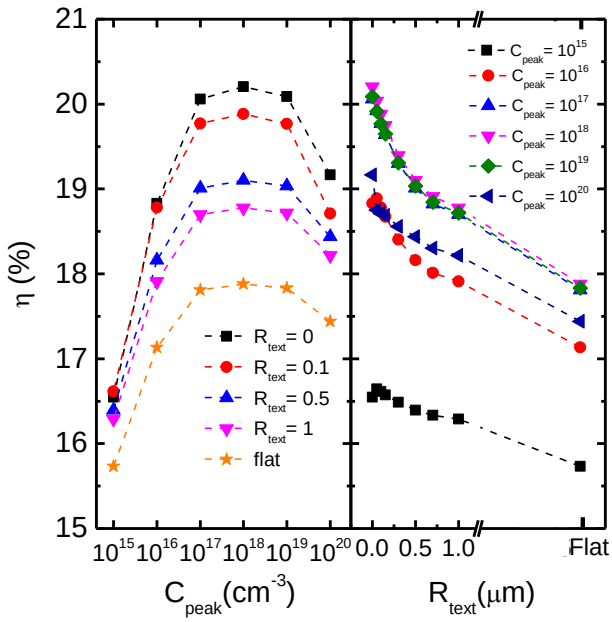

Figure.18: Efficiency (η) as a function of FSF Cpeak (left) and Rtext (right).

Finally, Figure.19 and Figure.20 show the efficiency curves as a function of FSF C_{peak} (for a pyramidal not-smoothed front texturing, i.e. R_{text}=0) and of R_{text} (for *NO-FSF* and optimal *FSF* cell designs), respectively, when considering different values of the SRV_{front}. Such parameterization was deployed with the aim of evaluating the impact of the front passivation quality on the performance of the investigated IBC solar cell. In particular, starting from the SRV_{front} values used for the initial calibration of the modelled devices ($SRV_{front\_NO\text{-}FSF}$ = 80 cm/s and SRV_{front_FSF} = 840 cm/s), we divided them by a scaling factor varying from 0.5 (i.e., corresponding to a worst passivation quality) up to 100 (i.e., corresponding to a strongly improved passivation quality). In Figure.19, we can observe that the FSF C_{peak} for which highest η is realized does not strongly depend on the front surface passivation quality,

however it tends to move slightly towards lower value when the surface passivation quality significantly improves. In fact, the calculated optimal FSF C_{peak} moves from 1×10^{18} cm^{-3} to 1×10^{17} cm^{-3} when the applied SRV_{front} scaling factor is equal to 100. Moreover, both Figure.19 and Figure.20 clearly show that, when considering a FSF C_{peak} around the optimal value (C_{peak} = 1×10^{18} cm^{-3}), an improved front passivation quality does not result in a strong efficiency improvement (0.2%$_{abs}$). On the contrary, in the case of low-doped *FSF* or *NO-FSF* cell designs, a better passivation quality leads to a significant efficiency improvement.

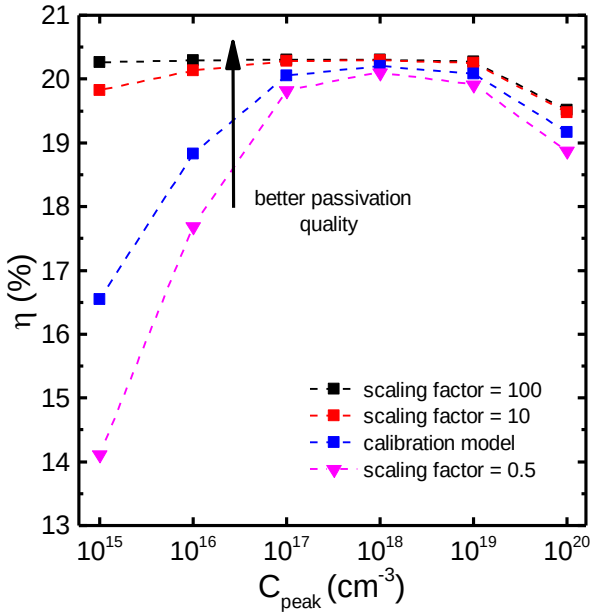

Figure.19: Efficiency (η) as a function of FSF Cpeak with Rtext = 0 for different levels of front passivation quality.

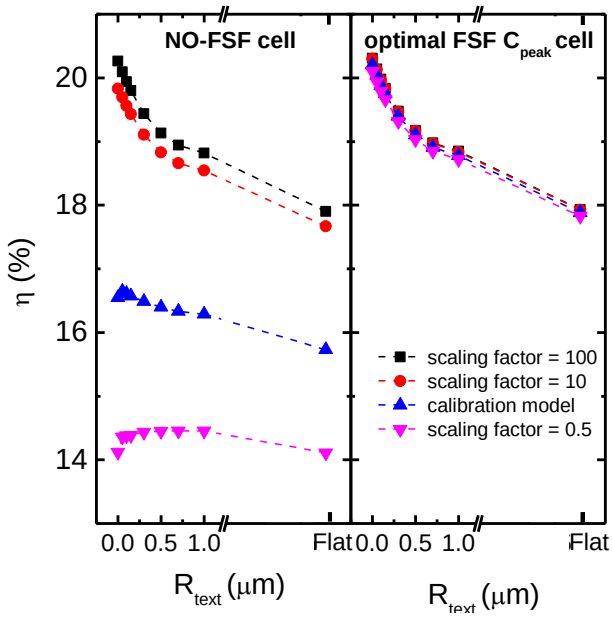

Figure.20: Efficiency (η) as a function Rtext in case of NO-FSF solar cell (left) and FSF solar cell with optimum FSF Cpeak (right) for different levels of front passivation quality.

It is worth noting that looking to previous results, the best conversion efficiency is reached for non-smoothed pyramids and optimum FSF C_{peak} of $1x10^{18}$ cm^{-3}. Such values lead to a negligible efficiency improvement when compared to fabricated IBC measured efficiency (< 0.1% absolute). Thus, FSF characteristics implemented in fabricated devices are very close to the calculated values which maximize efficiency. For this reason, we assumed FSF characteristics as measured (C_{peak}=$2x10^{19}$ cm^{-3} and R_{text}=0) to present an optimized IBC design related to fabrication process features in the next section.

4.4.3 Optimization of the rear-side geometry

After assessing the trustworthiness of our simulation platform, identified loss mechanisms (Section 4.1) and studying the Impact of front-side texturing and doping on IBC solar cells performance (Section 4.2), we proceeded with the optimization of the IBC design considering fabrication process features. To account for such inherent process effects, BSF, FSF and emitter doping demand experimental optimization to improve the conversion efficiency [79]. Thus, beyond that the fabricated FSF is very close to the optimal one, we have considered as fixed parameters those related to highly doped regions as well as all the ARC composition. Therefore, the optimization problem is reduced to find the rear-side design which maximizes conversion efficiency. In this respect, an optimization of the rear-side design was run for the considered reference 3×3 cm^2. The optimization procedure has involved the following parameters related to the rear-side geometry: the emitter contact width ($W_{cont,emitter}$), the BSF contact width ($W_{cont,BSF}$), the emitter width ($W_{emitter}$), the BSF width (W_{BSF}) and, accordingly, the rear pitch.

For the sake of simplicity and considering some process-related constraints on the minimum width and resolution of rear contacts and doped areas, we used an iterative optimization approach, whose flowchart describing the adopted algorithm for each optimization cycle is reported in Figure.21. Starting from the calibrated device model, this approach allows finding an optimized rear-side geometry in few steps of simulation as follows: (i) start an optimization cycle selecting an optimization parameter; (ii) sweep the selected parameter in a reasonable variation range; (iii) check if there is an efficiency improvement (if so, refine the variation range around the new optimum value and repeat step (ii); otherwise, stop the optimization cycle); (iv)

considering the new optimum value for the last considered parameter, repeat the optimization cycle, i.e. steps (i)-(iii), for another optimization parameter; (v) iterate steps (i)-(iv) until the efficiency does not longer show a relevant improvement.

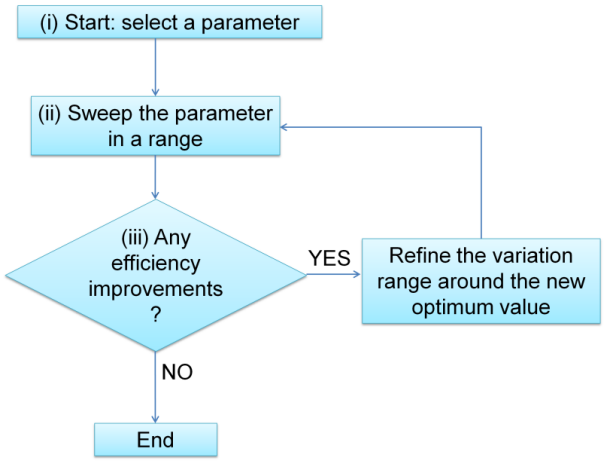

Figure.21: Schematic flowchart describing the adopted algorithm for each optimization cycle (the rhombic conditional block checks if there is an improvement in the conversion efficiency).

Table 5. Comparison between the simulated reference IBC solar cell and the solar cell with the optimized rear-side design. summarizes the comparison in terms of rear-side geometrical parameters and electrical performance between the simulated reference IBC solar cell and the one featuring the optimized rear-side design (Optimized design #1). We note that the performed optimization process led to a new rear-side geometry with a smaller rear pitch as compared to the fabricated reference cell due to the reduction of the emitter width. Further, the BSF contact width of the optimized solar cell increases with respect to the reference cell. These geometrical modifications

entail a conversion efficiency improvement by means of FF enhancement while J_{sc} and V_{oc} remain almost unaltered.

Table 5. Comparison between the simulated reference IBC solar cell and the solar cell with the optimized rear-side design.

	Parameter	Reference IBC cell (simulation)	Optimized design #1
Rear-side geometry	$W_{emitter}$ (μm)	800	400
	W_{BSF} (μm)	200	200
	Pitch (μm)	1000	600
	$W_{cont,emitter}$ (μm)	300	280
	$W_{cont,BSF}$ (μm)	50	150
Performance	J_{sc} (mA/cm^2)	40.82	40.47
	V_{oc} (mV)	642	645
	FF (%)	76.4	81.0
	η (%)	20.03	21.12

4.5 Discussion

4.5.1 Calibration of the opto-electrical device model

The calibration results reported in Section 4.1 demonstrate how the application of the two *screen layers* at the top and the bottom of the considered structure in the optical model was crucial to properly model the light man-

agement inside the device for wavelengths longer than 1000 nm. Indeed, the reflectance calculated at this wavelength range without using the two corrective *screen layers* reveals a poor light trapping in the simulation environment when compared to measurements (see Figure.5), thus indicating an escape probability of light rays higher than expected. The introduction of the corrective *screen layers* decreased such escape probability by emulating the effect of multiple reflections within the device. This has allowed a very good matching between simulations and measurements in the entire wavelength range of interest, as shown in Figure.5 and Figure.6 in terms of both R and T spectra.

Concerning the electrical modelling, Table 6. Summary of the most relevant calibration parameters used in the SRH recombination models. reports the most relevant process-related parameters used for the calibration. They refer to the SRH recombination parameters occurring in highly doped regions (FSF, BSF and emitter) and front-side interface. Indeed, we have observed during the calibration process that the performance of the modelled IBC solar cell are quite insensitive to the SRV at rear passivated interfaces, corresponding to the highly doped regions of BSF and emitter. This can be ascribed to the strong reduction of minority carrier density observed at these interfaces, due to the passivation effect of the build-in electrical field provided by both the BSF and emitter junctions. On the contrary, it has been observed that an accurate calibration of the SRV at the front-side passivated surface is crucial to properly fit both electrical and quantum efficiency measurements, especially in the case of *NO-FSF* device. Similarly, the accurate calibration of the doping-dependent model for the SRH recombination lifetime occurring in highly doped regions, expressed by equation (1), has been also mandatory for achieving a good matching between simulations and

measurements. In particular, as reported in Table 6, the performed calibration process has led to set the $\gamma_{emitter}$ parameter to a value of 1.9, higher than that extracted for FSF and BSF regions. This likely reveals that, in the two considered samples, there is the possibility of traps in emitter background. Such traps could be related to emitter process (i.e. epitaxial growth, passivating and metallization) and the main cause of V_{oc} degradation depicted on J_0 components shown in Figure.10.

Table 6. Summary of the most relevant calibration parameters used in the SRH recombination models.

Parameter	**FSF cell**	**NO-FSF cell**
SRV_{front}	840 cm/s	80 cm/s
γ_{FSF}	1	
γ_{BSF}	1	
$\gamma_{emitter}$	1.9	
N_{ref}	1×10^{16} cm^{-3}	

4.5.2 Front-side investigation

In Section 4.2 we have reported the results of the performed analysis aimed at investigating the impact of front-side texturing morphology and FSF doping on the performance of the reference IBC solar cell. In particular, the effect of the smoothing of the front texturing and different FSF C_{peak} doping has been firstly evaluated in terms of optical and recombination loss-

es. As Figure.12 depicts, the optical losses are referred mainly to reflectance, rising as R_{text} increases due to the worse light trapping in the case of a smoother front texturing. As a matter of fact, a significant increase of these losses can be observed as R_{text} increases in agreement with the observed degradation of J_{ph}. Notice that calculated transmittance losses indicate a negligible increment (0.3 mA/cm^2) respect to R_{text} confirming also a small light trapping improvement for perfect pyramids texturization. On the other hand, calculated transmittance losses are almost insensitive to FSF C_{peak}, while parasitic absorption became slightly apparent in J_{ph} behavior for FSF $C_{peak} > 1x10^{19}$ cm^{-3} due to the enhanced FCA. The recombination losses can be discussed through the trends of J_0 and J_{rec} reported in Figure.13 and Figure.14, respectively. J_0 and J_{rec} curves as a function of FSF C_{peak} exhibit a reversed bell shape with a clear optimal value around 1×10^{18} cm^{-3}. According to [32], such an optimal FSF C_{peak} results from the trade-off between the effect of the front-side built-in electrical field, which affects the minority-carrier density in the FSF region, and the doping-dependent SRV_{front}. Therefore, in correspondence of FSF C_{peak} around the optimal value, the recombination losses are strongly reduced and practically do not depend on the front texturing morphology. Conversely, in the case of FSF C_{peak} quite lower or higher than the optimal value, a J_0 and J_{rec} decrease can be observed when increasing R_{text} due to the reduction of the front interface area, which leads to lower front surface recombination losses. Additionally, by observing the variation range of J_0 and J_{rec} within FSF C_{peak} and R_{text} sweeps, we noted that recombination mechanisms are more affected by the doping profile rather than the front texturing morphology.

J_{sc} curves showed on Figure.15 can be explained in terms of loss mechanisms by looking into J_{ph} and J_{rec} curves in Figure.12 and Figure.14 respectively. In fact, from charge conservation law, J_{sc} can be expressed as:

$$J_{sc} = J_{in} - J_{opt} - J_{rec} = J_{ph} - J_{rec}. \quad (2)$$

According to the previously discussed FSF C_{peak} influence on the trends of J_{ph} and J_{rec}, J_{sc} curve exhibits a bell-shaped trend featuring the maximum value in correspondence of the minimum J_{rec}. In turn, the decreasing curve of J_{sc} related to R_{text} variation (see Figure.15) is mainly dictated by the J_{ph} behavior (see Figure.12). In fact, J_{sc} generally decreases when increasing R_{text} due to optical losses increment. However, in Figure.15 and for low FSF C_{peak}, we can note that highest J_{sc} is obtained at $R_{text} \neq 0$. For such cases, a small increase of J_{sc} within $R_{text} = 0$ and 0.05 μm is noticeable due to the small reduction of J_{ph} is counterbalanced by a higher decrease of J_{rec}.

V_{oc} mainly depends on the ratio between J_{ph} and J_0, as expressed by the well-known following relationship:

$$V_{oc} = \frac{nkT}{q} \ln\left(\frac{J_{ph}}{J_0} + 1\right). \quad (3)$$

Conformal to equation (3), the observed behaviour of V_{oc} as function of FSF C_{peak} (see Figure.16) is bell-shaped and is mainly dictated by the trend of J_0 (see Figure.13), since J_{ph} is almost not affected by FSF C_{peak} (see Figure.12). However, for FSF C_{peak} around the optimum value, we observe that, even though J_0 is rather independent from R_{text}, V_{oc} slightly decreases due to the reduction of J_{ph} for higher R_{text}. For the other FSF C_{peak} cases and with re-

spect to R_{text}, V_{oc} mainly follows a trend that is mirrored to the one of J_0, as shown in Figure.16. Therefore, V_{oc} can be improved by applying perfect pyramidal texturing for FSF C_{peak} around optimal value (dominated by optical losses) and by applying smoother texturing in the other FSF C_{peak} cases (dominated by recombination losses).

Concerning the FF, we note in Figure.17 that FF strongly increases in the range of low FSF C_{peak} (up to 1×10^{18} cm^{-3}) due to two concurrent mechanisms occurring in the FSF, that are recombination (see Figure.13 and Figure.14) and carrier lateral transport (sheet resistance). On the contrary, in the range of high FSF C_{peak} (above to 1×10^{18} cm^{-3}), the FF increment with the FSF C_{peak} is less apparent because the further improvement of the lateral transport is counterbalanced by the slight increase of recombination losses. Figure.17 also shows a FF increase with R_{text} because, in the case of a smoother front texturing, both front-side surface recombination and resistive mechanisms decrease due to the reduction of front interface area and of FSF current paths, respectively.

Finally, from a comparison of η trends (see Figure.18) with the aforementioned J_{sc}, V_{oc} and FF results, we can easily notice that the efficiency mainly follows the J_{sc} behavior. Therefore, the following overall considerations can be drawn for the investigated IBC solar cell. First, there is an optimum FSF C_{peak} independent from R_{text}, mainly ascribed to the reduction of recombination losses. Second, the not-smoothed front texturing (i.e., $R_{text} = 0$) is always better because of the improved light management, except for low-doped FSF cell designs (see Figure.18), according to the J_{sc} trend reported in Figure.15. Third, a higher influence of the FSF doping can be observed in the case of rough front texturing. In fact, as shown in Figure.18, the difference in terms of efficiency between the *FSF* and the *NO-FSF* designs in-

creases as R_{text} decreases. This means that, when the light trapping improves (J_{ph} increases), the effect of recombination losses related to the FSF doping becomes more significant. Fourth, a higher influence of the front texturing morphology can be observed for a FSF C_{peak} around the optimal value. This means that, in the range around the optimal FSF C_{peak}, the impact of FSF recombination losses is strongly reduced and therefore the efficiency mainly depends on light management.

The results of the performed analysis aimed at evaluating the impact of the front-side passivation quality in the investigated IBC solar cell have been reported in Figure.19 and Figure.20. As already stated in Section 4.2, the optimal FSF C_{peak} is quite independent from the passivation quality at the front side. In addition, simulation results reported in Figure.19 and Figure.20 demonstrate that the use of an optimal FSF doping is quite sufficient to reduce the front-side recombination losses. As matter of fact, an improved front-side passivation does not lead to a significant further η improvement in the IBC cell featuring an optimal FSF doping. Conversely, as expected, low-doped FSF or *NO-FSF* IBC cells require a very outstanding passivation quality at the front side to be competitive. Moreover, Figure.20 shows that the *NO-FSF* cell exhibits a stronger dependence on the front texturing morphology when considering a better front passivation quality and hence a reduction of front-side recombination losses. Indeed, in this case, the efficiency mainly depends on the optical losses and therefore the highest efficiency of the NO-FSF cell is achieved for $R_{text} = 0$ (differently from what observed in Figure.18). On the contrary, a worst passivation quality leads to require in the NO-FSF cell a further smoothing of the front texturing to maximize the conversion efficiency due to the reduction of the front interface area and, consequently, of the front surface recombination losses (see Figure.20).

4.5.3 New IBC rear-side design

The rear-side geometrical parameters and the electrical performance of the new optimized IBC design have been reported in Section 4.3. As shown in Table 5, the optimized rear-side geometry is characterized by a smaller pitch (from 1000 μm to 600 μm), featuring narrower emitter and larger BSF contact coverage as compared to the fabricated reference IBC cell. These geometrical modifications have impacted on the complex trade-off between optical, recombination and resistive losses, thus resulting in different electrical performance. As result of such compromise, the optimized geometry presents a significant increment on FF, rather than J_{sc} and/or V_{oc} improvement. Thus, recombination losses practically remain but resistive losses notably decrease thanks to lateral transport reduction expressed in terms of smaller pitch.

Overall, numerical results show that the adoption of an optimized rear-side geometry for the considered IBC solar cell can potentially lead to a conversion efficiency above 21%, with an efficiency improvement of more than $1\%_{abs}$ as compared to the fabricated reference IBC solar cell. It is worth noting that even higher efficiencies are reachable deploying pitches smaller than 600 μm and metallization thicker than 2 μm. However, such designs might not be industrially feasible or are just too expensive, owing to technological constrains to achieve the required pattern resolution and the needed thickness of metallic fingers. For example, according to our simulation model, $\eta = 21.3\%$ could be obtained for a 200-μm wide pitch design and 10-μm thick Al fingers.

Beyond that the optimization of doping parameters is inherent to IBC fabrication process, looking into the reduction of reported emitter background traps (i.e. lowering $\gamma_{emitter}$ in equation (1), see Section 5.1), we identified the potential to improve further the performance of our IBC solar cells architec-

ture. Setting $\gamma_{emitter}$ = 1 and running again our optimization algorithm (see Figure.21), 400-μm wide pitch and 4-μm thick metallization resulted in η = 22.39% (see Optimized design #2 in Table 7). From the reference cell to the optimized design cell #1 in Table 5, the efficiency improvement was due to an increase of FF related to optimized rear-side design. On the other hand, the efficiency boost in Table 7 from Optimized design #1 to Optimized design #2 was due to the improved quality of the emitter (higher V_{oc}) and the augmented emitter-to-pitch ratio (higher J_{sc}). In particular, such value was found to be 85%, that is compatible with the work by Kluska et al. [63]**¡Error! No se encuentra el origen de la referencia.** and accommodates the trade-off between electrical shading and series resistance.

Table 7. Comparison between optimized IBC solar cell designs

	Parameter	**Optimized design #1**	**Optimized design #2**	**Optimized design #3**
Rear-side geometry	$W_{emitter}$ (μm)	400	340	340
	W_{BSF} (μm)	200	60	60
	Pitch (μm)	600	400	400
	$W_{cont,emitter}$ (μm)	280	50	50
	$W_{cont,BSF}$ (μm)	150	50	50
	$\gamma_{emitter}$	1.9	1	1
	Bulk lifetime (ms)	2	2	5
	Al thickness (μm)	2	4	4
Performance	J_{sc} (mA/cm^2)	40.47	41.17	41.5
	V_{oc} (mV)	645	674	676
	FF (%)	81.00	80.69	81.4
	η (%)	21.12	22.39	22.84

Further, considering our IBC self-aligned process in high quality *c*-Si bulk, we simulated a conversion efficiency of 22.84% by setting the *c*-Si bulk lifetime to 5 ms in the Optimized design #2 (see Optimized design #3 in Table 7). In this case, given lower SRH recombination occurring in the *c*-Si bulk from Optimized design #2 to Optimized design #3, the contribution of J_{rec} to the J_{sc} could be further decreased (see Equation 2) and the FF boosted.

4.6 Conclusions

In this work, we have presented a detailed modelling and optimization study on reference homo-junction IBC *c*-Si solar cells fabricated through a novel self-aligned process, combining P-ion implantation for the FSF and BSF and epitaxial growth for the emitter. The study has been carried out by means of a TCAD-based opto-electrical device model based on an innovative approach, involving the accurate optical and electrical modelling of a pyramidal pseudo-random front-textured morphology. The device model has been initially developed and calibrated with respect to a fabricated reference solar cell through the comparison between measured and simulated R, T, IQE and EQE spectra and electrical parameters. As a result of the calibration process, the opto-electrical losses of the considered device have been identified both quantitatively and qualitatively.

Then, the calibrated device model has been deployed to extensively study the impact of front-side texturing and doping on the performance of the considered IBC solar cell. Such an investigation has been also carried out by considering different passivation quality levels at the front side. Simulation results show that a not-smoothed front texturing morphology and an optimal FSF doping are mandatory to minimize both optical and recombination loss-

es in the considered IBC cell and, consequently, to maximize its conversion efficiency. In fact, it was demonstrated that recombination losses are more affected by the FSF doping profile rather than the front surface texturing morphology. Moreover, the performed analysis reveals that the optimal FSF doping is almost independent from the front texturing morphology and FSF passivation quality. Accordingly, simulation results demonstrate that (i) an IBC cell featuring an optimal FSF doping does not exhibit a significant efficiency improvement when the FSF passivation quality strongly improves, therefore the use of an optimal FSF doping is sufficient to reduce the front-side recombination losses, and (ii) IBC cells based on low-doped FSF demand a very outstanding front passivation quality to be competitive.

The calibrated model, that could be potentially used to simulate other solar cell architectures than homo-junction IBC devices, has been used to optimize the rear-side geometry of the reference IBC solar cell. The optimization process, based on an iterative approach, has been performed in few simulation steps. As a result of this optimization, a new rear-side geometry featuring a smaller rear pitch and a larger BSF metallic contact width with respect to the fabricated IBC cell has been defined. Numerical results show that the adoption of these geometrical modifications can potentially lead to an efficiency improvement of more than $1\%_{abs}$ as compared to the reference IBC solar cell. Finally, by allowing changes in the emitter quality and in *c*-Si bulk lifetime, we optimized further our IBC architecture simulating a 22.84% efficient solar cell for 280-μm thick *c*-Si bulk.

Five

5 Modelling of Passivated Contacts

In this Chapter, it is presented a theoretical study of the potentiality of novel solar cells featuring passivated contacts. At the same time, physical mechanisms ruling transport and passivation has been modelled identifying the critical parameters with the aim to present design guidelines for optimal passivated contacts. The results shows that tunneling distance, barrier energy and effective tunneling mass represent the critical parameters of tunneling oxide, but build in voltage, behavior is correlated to band alignment pointing on critical parameters linked to deposited layer and crystalline silicon interface.

5.1 Introduction

From Chapter 3 and 4, around 80 fA/cm^2 in dark and around of 10% of J_{sc} losses are produced by the highly defective metal/silicon interface. As matter of this fact, it is crucial passivate such interfaces to achieve most efficient solar cells. Accordingly, PV community has focused on the concept of passivated contacts as a carrier selective collector that allows good passivation

quality and high conductivity at the same time. In this context, novel solar cells structures has been developed and fabricated. In particular, Tunnel Oxide Passivated Contact (TOPCon) [83] was proposed achieving an efficiency of 25.1% [46]. In this structure, the advantages of full rear metallized and passivated rear contact allows to overcome the typical lateral transport losses on PERL structures [46]. Moreover, a theoretical study describing main physical mechanisms of such structure has been presented by Steinkemper et al [84] by means of TCAD simulations. Similarly to TOPCon, another novel structure has been presented by Ingenito et al [85] to exploit the advantages of passivating both front and rear contacts.

In this Chapter, it is presented the potential advantages of conventional solar cells featuring passivated contacts. To this purpose, an opto-electrical model has been validated by means of measured J-V curves and then used to deploy a systematic study with the aim of identify the critical parameters. Then, the main physical mechanisms related to both transport and passivation are described to provide design guidelines for implementing optimal passivated contacts.

5.2 Simulation approach

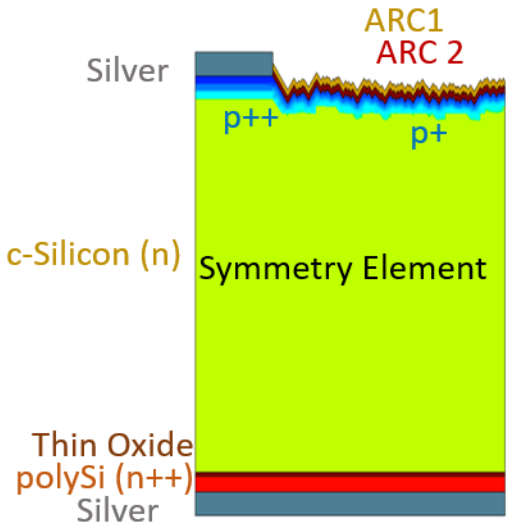

Figure 1. Sketch of simulated symmetry element for TOPCon structures.

The opto-electrical modelling has been based on the drift-diffusion model by using state-of-the-art parameters as it is explained in Chapter 2 for structures featuring passivated contacts as Figure 1 depicts. In particular, Table 1 summarizes particular parameters assumed for this study. In order to evaluate the potential conversion efficiency of passivating contact structures, we assume 1nm thick SiO_2 as tunneling oxide (TOX).

Table 8 Modelling and Parameters used on numerical simulations.

Model/Parameter	**This work**
SRH lifetime	Bulk lifetime 7ms [84]
Surface SRH recombination velocity at passivated interfaces (including passivated contacts)	SRV=10cm/s
Tunneling model	Non Local Tunneling Model [28]
Effective tunneling mass for e/h in SiO_2	0.4/0.32 [86] [84]
Optical Model	Ray-Tracing [28]
Incident spectrum	AM1.5g [47]

5.3 Validation

The simulation platform has been validated according to the solar cell described in [84] by means of measured J-V curves as Figure 2 depicts. In fact, a good agreement between simulation and measured values has been reached. It is worth noting that values related to emitter design has been obtained by means of EDNA [87] using reported values in [84]. Similarly to the model applied on Chapter 4, the opto-electrical model share the same domain between optical and electrical stages.

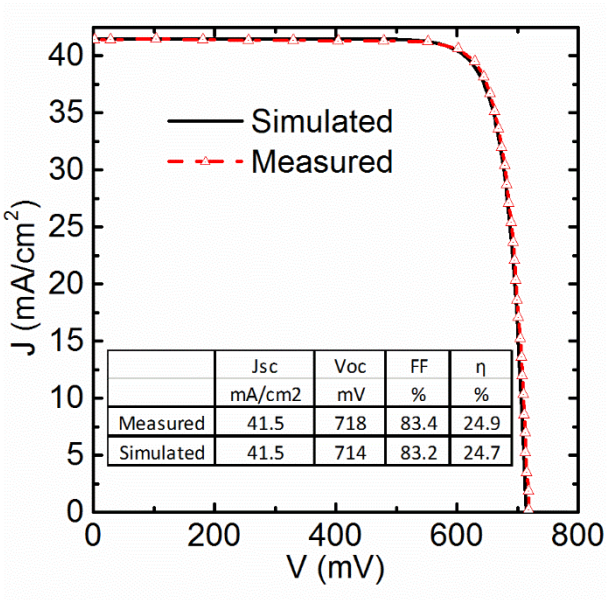

Figure 2. Opto-electrical model validation.

5.4 Results and Discussion

5.4.1 Solar Cells featuring Passivated Contacts

The roadmap to achieve higher efficiency on TOPcon structures is reported in Figure 3. The main parameters that constrains the conversion efficiency are related to c-Si thickness and front contact shadowing. Accordingly, thinner bulks lead to efficiency improvement by means of raising the FF while smaller front contact shadowing leads to J_{sc} increasing (light-trapping).

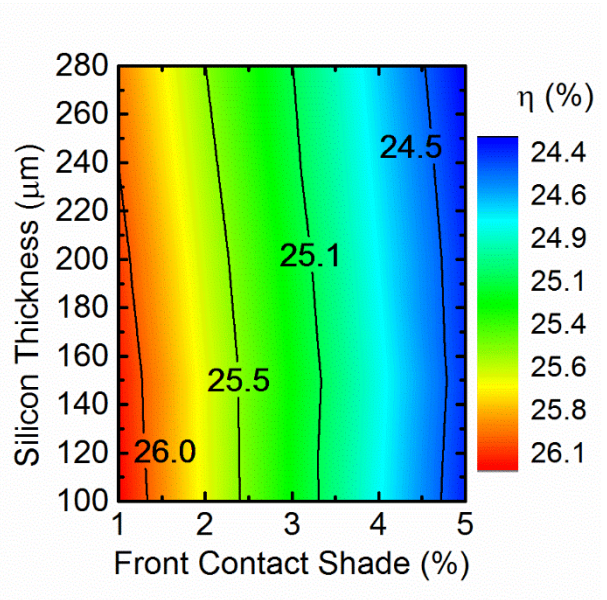

Figure 3. Roadmap for TOPcon conversion efficiency.

Beyond the potential high conversion efficiency of this structure, it is crucial to attain a high quality front emitter, an outstanding front passivation quality accompanied for a very small front contact as Figure 4 shows. In fact, these parameters become the technological constrains related to fabrication process.

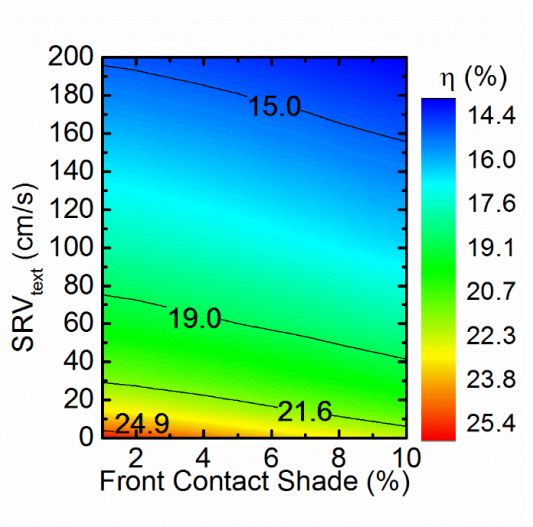

Figure 4. Potential TOPcon conversion efficiency as a function of technological constrains: front passivation quality and front contact shading.

To reach even better efficiency front contact has to be designed with similar passivation scheme. However, such implementation leads to potential J_{sc} degradation [88] due to the parasitic absorption coming from the complete front passivated structure. Accordingly, high values of V_{oc} are achieved (710mV) but a low J_{sc} as drawback.

To face this disadvantage, Ingenito et al [85] proposed a novel structure in which both contacts are passivated and apply homo-junction schemes to passivate the front of the solar cell. In this way, front contact uses the passivation structure only beneath the contact and passivation of front contact do not degrade the absorption of light. Accordingly, different than TOPcon case, Figure 5 shows the proposed structure considering a rear junction. The reason of rear junction assumption will be discussed in following sections.

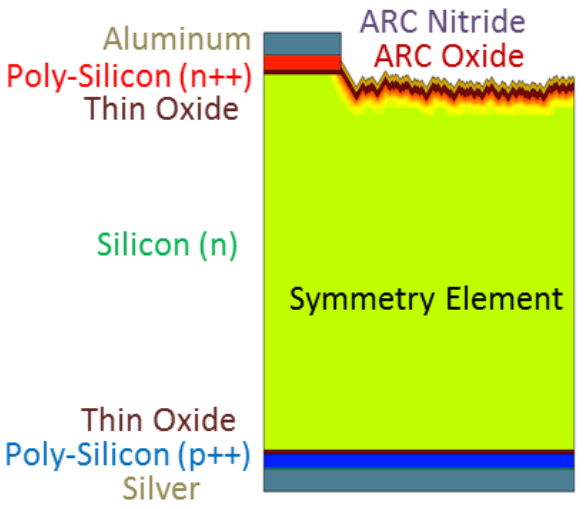

Figure 5. Passivated front and rear contact solar cell Sketch.

In order to evaluate both possible configurations: front or rear junction, it has been deployed a set of simulations considering tunneling mechanisms limitation on the typical crowding currents formed around the front contact as Figure 6 depicts.

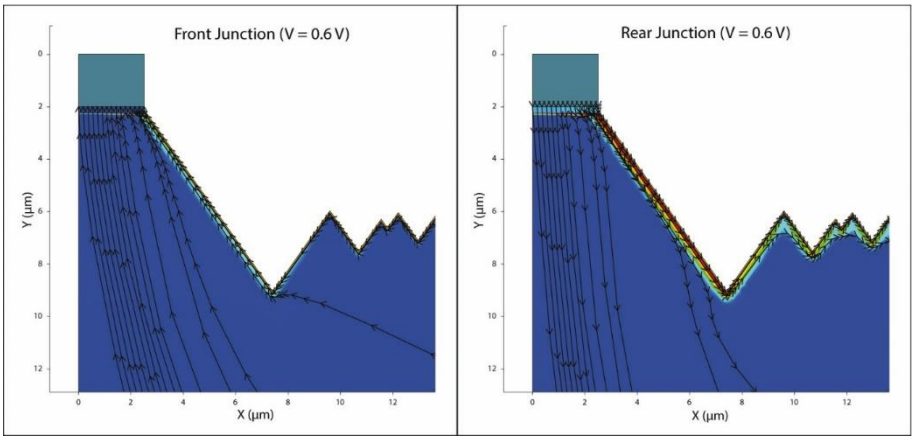

Figure 6. Current streamline formed around front contact (left) and rear contact (right) junction. Colors highlight the crowding increase near to front homojunction.

In order to account the tunneling mechanisms that allows the transport of carriers through the TOX (SiO_2) on both contacts, it has been deployed a set of simulations for different effective tunneling masses for electrons ($m_{t,e}$) and holes ($m_{t,h}$). As shown in Figure 7, rear junction devices have higher potential efficiency than front junction considering reported values of $m_{t,e}$ and $m_{t,h}$ for SiO_2 [86]. Furthermore, such an effect is more apparent when comparing calculated potential efficiencies corresponding to recommended values of $m_{t,e}$ = 0.4 and $m_{t,h}$ = 0.32 [86] for rear junction (~26%) and front junction (~24%).

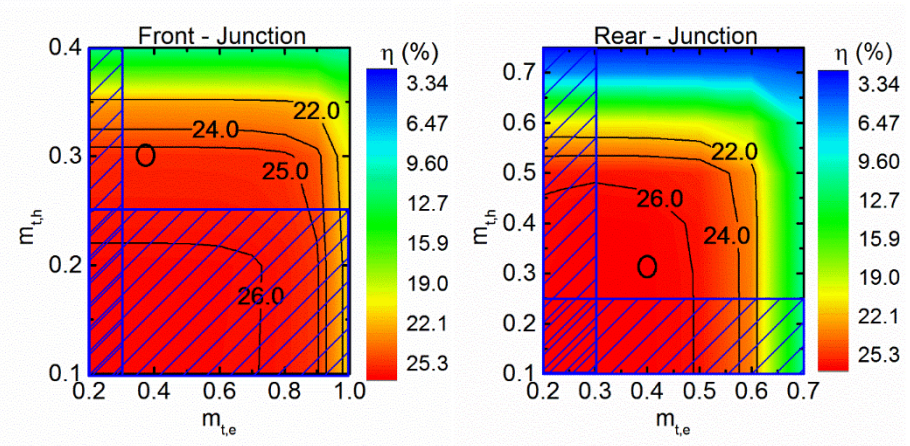

Figure 7. Conversion efficiency maps for different $m_{t,e}$ and $m_{t,h}$, Efficiency values under blue pattern correspond to not reported $m_{t,e}$ and $m_{t,h}$ values. Efficiency values for $m_{t,e}$ = 0.4 and $m_{t,h}$ = 0.32 for oxides thickness < 3.6nm [86] *are marked with black circles.*

5.4.2 Tunneling Mechanisms

Tunneling mechanisms in TCAD Sentaurus [28] are modelled by a non-local method that apply:

$$J_{e,h} = \frac{qm^*}{2\pi^2\hbar^3}\int \Gamma(E)N(E)dE \qquad (13)$$

Where $m^*$is the effective mass of the parabolic band edges, $\Gamma(E)$ is the tunneling probability, $N(E)$ is the supply function [89] and it is expressed as follows:

$$N(E) = kT\ ln\frac{\xi_{h,e1}(E)}{\xi_{h,e2}(E)} = kT\ ln\frac{1+e^{\frac{E_{f1}-E}{kT}}}{1+e^{\frac{E_{f2}-E}{kT}}} \qquad (14)$$

Where E_{f1} and $E_{f2}$are the Fermi energy in each side of the interface. Similarly, Sentaurus evaluate the tunnel probability by applying a non-local method. For the sake of simplicity, on passivated contacts structures the approach can be driven by direct tunneling [90] through a rectangular barrier in which, tunnel probability can be expressed as follows:

$$\Gamma(E) = e^{-2d\frac{\sqrt{2m_t\Delta E}}{\hbar}} \qquad (15)$$

Where d is the tunneling distance, m_t is effective tunneling masses (e,h) and ΔE is barrier energy.

In fact, looking into (15), the parameters that degrade exponentially the tunneling current are d, m_t, and ΔE. Note that all the other parameters are pre-exponentials [90].

In Figure 8, tunneling mechanisms working on this structure can be observed by means of aforementioned critical parameters in conduction band (left) and valence band (right) alignment. A proper band alignment that enhance the supply function is achieved thanks to the assist of in-diffused doping profile in c-Si, starting from silicon/TOX. In both contacts, for in-diffused cases, the tunneling current is increased improving the transport through tunneling oxide.

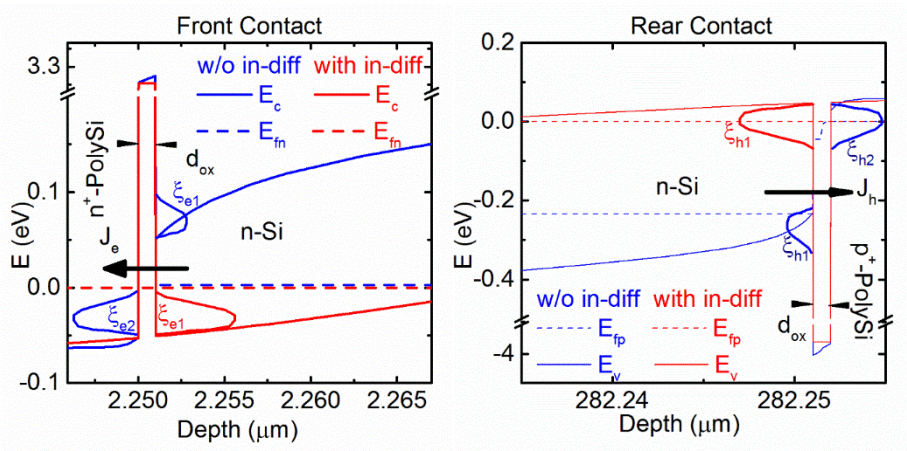

Figure 8. Conduction band alignment (left), and valence band alignment (right) for the extraction of electrons and holes. Band alignment is supported by in diffusion that improve the supply function (red).

5.4.3 Passivated contacts on c-Si p/p++ deposited material

With the aim to extend the results to other possible materials that can be deposited over TOX, it has been deployed an analysis accounting the use of passivated contacts on c-Si p-type and deposited p++ layer on the rear side as Figure 9 depicts.

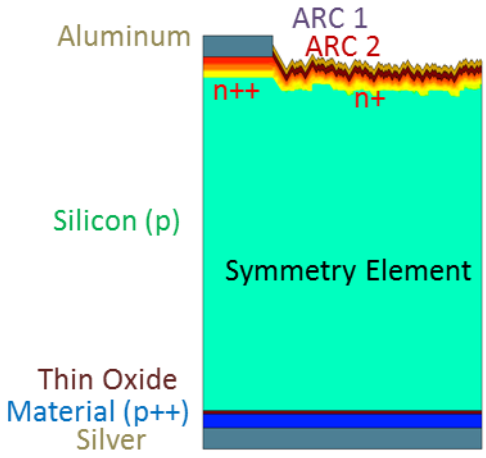

Figure 9. Sketch of simulated structure used for the study of holes carrier selective contact.

Models previously described in Table 1 were used for a structure featuring characteristics described on Table 9.

Table 9. Simulated solar cell parameters

Parameter	**Value**
n++ doping	$1x10^{20}cm^{-3}$
p++ active doping (N_A)	$1x10^{20}cm^{-3}$
p doping	$3x10^{15}cm^{-3}$
C_{peak} front passivation (n+)	$1x10^{18}cm^{-3}$
p++ thickness	0.25µm
Silicon thickness	100µm

Thin Oxide thickness	1.5 nm
Metal thickness	2µm
Pitch	500µm
Front contact	5µm
Deposited p++ material	SiC:3C [91]

5.4.4 Tunneling Transport limitation

As it was described on Eq. (3), intrinsic critical parameters affecting tunneling probability are the tunneling masses for holes and electrons ($m_{t,e}$ and $m_{t,h}$) and the energy barrier (ΔE) while tunneling distance parameter (d) is a process related parameter. Accordingly, it has been deployed simulations considering material as Table 10 summarizes. It is worth noting that barrier energy was assumed considering valence band as reference.

Table 10 Summary of tunneling oxide materials and parameters.

	SiON	**SiO_2**	**HfO_2**
$m_{t,e}/m_{t,e}$	(1) 0.21/0.21 (2) 0.42 /0.31[2]	0.3-0.8 [1]	0.1-0.18 [2][3]
E_B HVB	2.9eV	4.5eV	2.5eV

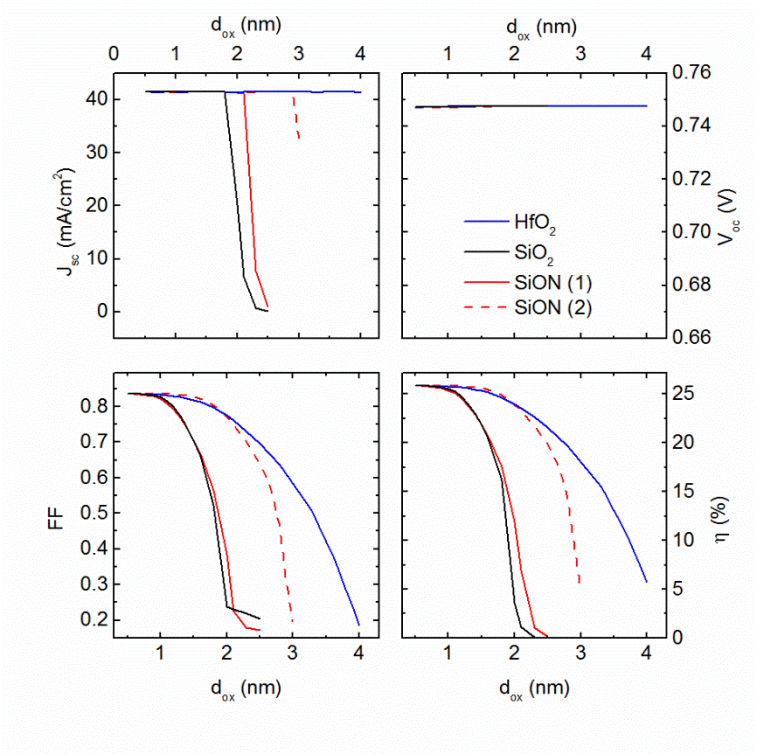

Figure 10. d_{ox} for different TOX materials with different tunneling parameters.

As it was expected, d is an extrinsic (related to process) critical parameter that limits the transport of holes as Figure 10. Indeed, small tunneling masses, and a small energy barrier improve the tunneling mechanisms allowing a thicker TOX to achieve higher efficiency. As matter of this fact, dox<3nm leads to η>22% in case of HfO2, but for SiO2 such efficiency can be reached for dox<1.7nm.

Similarly, the passivation quality at c-Si/TOX interface has been evaluated by means of surface recombination velocity (SRV) as Figure 11 reports. Conversion efficiency is almost insensitive to the SRV.

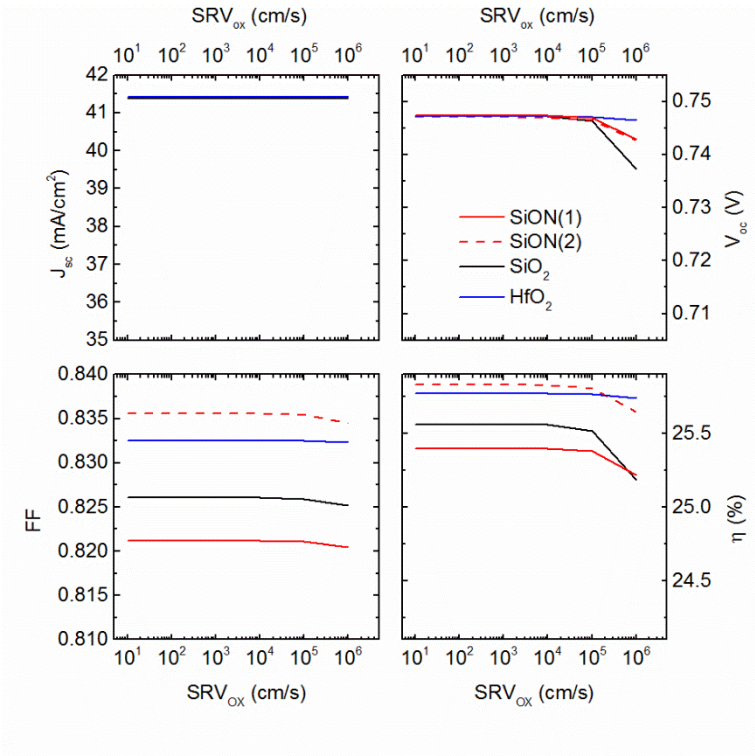

Figure 11. Solar cell FOM evaluated for different SRV at c-Si/TOX interface.

Such an effect is ascribed to the positive band bending on valence band close to c-Si/TOX interface observed on Figure 12. In fact, the band bending over-pass quasi-fermi level of holes filling hole states and repealing electrons (minority carrier) from the interface. For SiC:3C p++, the band bending in c-Si interface is achieved thanks to the Vbi between c-Si (p) and SiC:3C (p++), as it is explained on following sections.

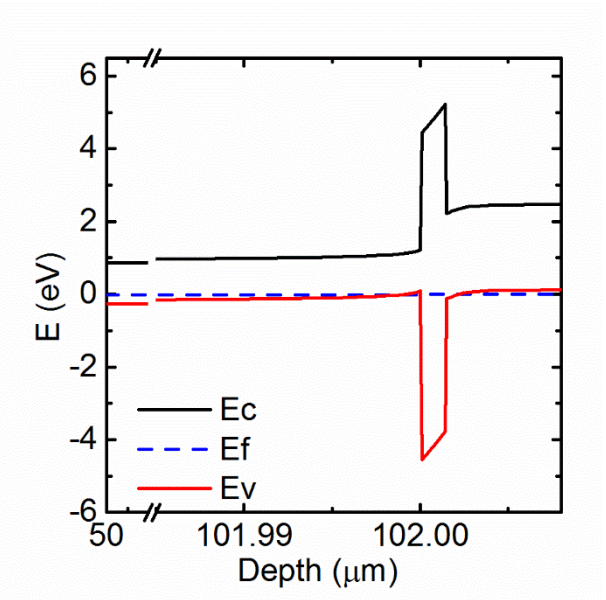

Figure 12. Band diagram illustrating the band bending close to TOX interfaces.

To understand the potential of this structure, by achieving similar band bending than SiC:3C, it has been deployed a set of simulation considering bandgap and electron affinity as variables. Accordingly, results are showed on Figure 13 evaluating conversion efficiency as a function of band gap (Eg) and electron affinity (χ_o). In fact, as it was proposed efficiency behavior is correlated to Vbi form the c-Si and deposited material.

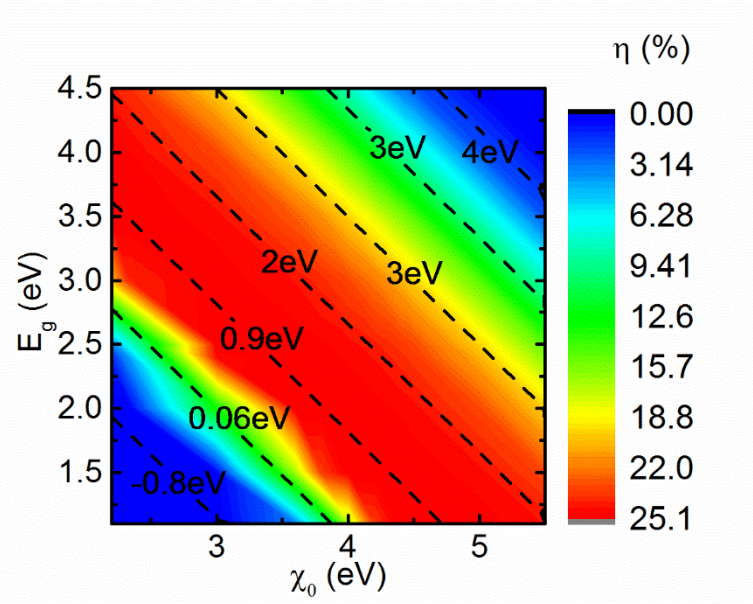

Figure 13. Conversion efficiency as a function of Eg and χ_o. Dotted lines show calculated Vbi values.

In Figure 13, it can be observed 3 different regions:

i) Vbi<0.1eV
ii) 0.1eV<Vbi<3eV
iii) Vbi>3eV

In region i), tunneling transport mechanisms are degraded by the absence of filled hole states on c-Si. Thus, in such case, the assist of in-diffusion on c-Si potentially improves the transport mechanisms as Figure 14 depicts. In-diffusion allows that valence band overpass quasi-fermi level of holes degenerating c-Si near to interface with the consequent increase of holes density. Indeed efficiency rise from 20% to 24.5% when modelling including in-diffusion profile.

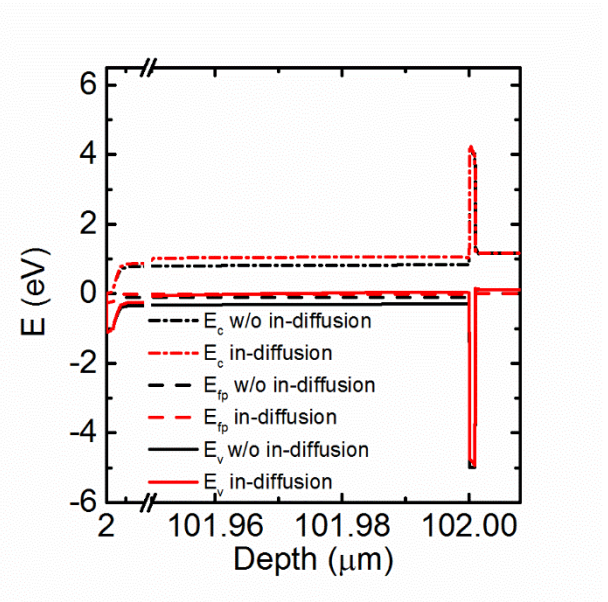

Figure 14. Band diagram for χ_o = 3.8eV and Eg = 1.1eV (Vbi<0.1eV) illustrating the effect of in-diffusion on c-Si.

In region ii), tunneling transport through TOX is improved by the good band alignment that allows the filled hole states at c-Si interface and also repealing minority carriers (electrons). In this zone, is expected that efficiency is insensitive to passivation quality thanks to the aforementioned band bending at c-Si (see Figure 12)

Finally, in region iii), tunneling transport mechanisms are degraded by means of the tunneling distance from filled hole states. In fact, the band bending on the deposited layer is less apparent leading to the addition of more than 3nm to TOX thickness as total tunneling distance. This effect are overcome by rising the active doping on the deposited layer as Figure 15 illustrates.

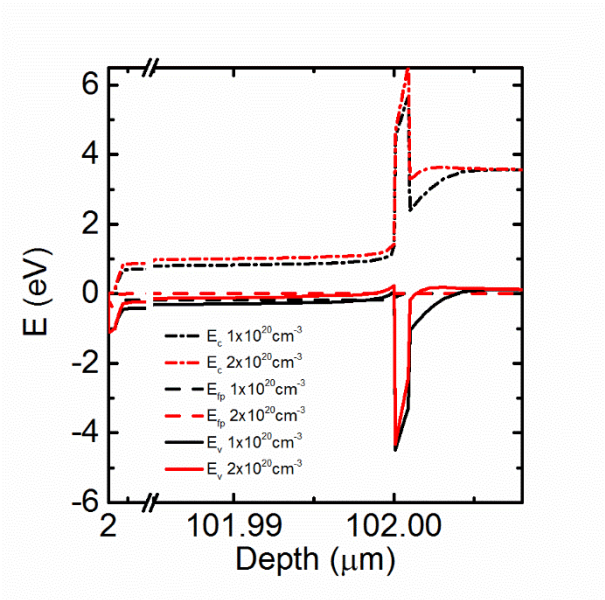

Figure 15. Band diagram for χ_o = 4.4eV and Eg = 3.5eV (Vbi>3eV) demonstrating the effect of rising the doping on the deposited layer from $1x10^{20}cm^{-3}$ to $2x10^{20}cm^{-3}$.

5.5 Conclusions

In this Chapter, it has been presented a detailed analysis of mechanisms working on passivated contacts structures. The analysis was developed by using TCAD numerical simulations on the basis of a calibrated and validated model through J-V measurements. Then, the opto-electrical model was used to analyze the potential efficiency for novel solar cells structures as TOPcon [ref] and PeRFECt [ref]. As result of the analysis, it was found that in case of TOPcon, front passivation quality and front contact shadowing are the main technological constrains. In case of PeRFECt structure, it has been demonstrated that tunneling transport occurring in front contact limit the most the conversion efficiency. Accordingly, a PeRFECt design featuring a rear emitter is potentially more efficient than the front emitter case. It was also noted

that for collecting carriers by using highly doped poly-silicon, it is crucial the support of acceptors/donors in-diffused zones, close to the interface because the improvement on the supply function by filling states of holes/electrons on c-Si/TOX interface (band alignment). The analysis was extended to a c-Si p-type structure featuring a front emitter and rear passivated contact by means of p++ SiC:3C as deposited layer. It was confirmed that the technological constrain that limit tunneling transport is oxide thickness, but such limitation is linked to critical intrinsic parameters of TOX as mt,e, mt,h and energy barrier. As smaller TOX intrinsic parameters are, the thicker TOX are allowed to achieve suitable conversion efficiency. Similarly, it was demonstrated that this structure is almost insensitive to contact passivation quality due to the band bending that overpass quasi-fermi level of holes near to c-Si/TOX interface rising holes density and repealing electrons. This effect is result of Vbi and replace the impact of the aforementioned doping in-diffusion for polysilicon case. Similarly, it was identified a range of Vbi (0.1eV<Vbi<3eV) that results on attainable potential conversion efficiency without the adoption of in-diffusion dopants. For smaller Vbi values, tunneling transport mechanisms are restricted by the absence of hole filled states at c-Si, in such cases the assist of in-diffusion doping is crucial. For Vbi larger than the optimal range, tunneling transport is restricted due to the increase of the tunneling distance by means of smooth band bending on deposited layer that leads to increase in more than 3nm the tunneling distance from filled states in c-Si to same energy valence band in deposited layer. This distance is potentially reduced when increasing the active doping in deposited layer. Finally, main design guidelines are summarized on Table 11.

Table 11 Design guidelines for passivated contacts.

Parameter	**Best**	**Remarks**
Oxide thickness (d_{ox})	↓	Process limited
Effective tunneling mass for holes ($m_{t,h}$)	↓	Intrinsic to TOX material
Energy barrier (E_B)	↓	Intrinsic to TOX material
Deposited layer band bending width	↓	Active ionized acceptors => $N_{A,SiC}$↑
Available carriers at cSi interface: In-diffusion (E_{fp}-E_v)↓ or V_{bi} in optimal range	↑	Δn↓; p↑ => $R_{surf,srh}$↓ In-diffusion

Six

6 Conclusions

In order to exploit the advantages of solar energy, novel solar cells concepts and devices have been developed. Such models became complex and demands the compromise between physical mechanisms occurring inside the solar cells to achieve higher efficiencies. In this context, to calculate the best trade-off for highest efficiencies, it is crucial the use of simulation tools. In this thesis, novel c-Si solar cells structures and concepts have been discussed and assessed by means of numerical simulations. In particular, critical parameters have been presented providing guidelines to achieve the highest efficiency according to technological limitations.

To this purpose, in Chapter 1, the evolution of c-Si solar cells was presented in the pathway to achieve the realistic efficiency limit. In this path, the decisive key of using advanced c-Si solar cell structures and concepts were presented. In addition, the main goals of this thesis were presented.

In Chapter 2, the general state-of-the-art properties related to c-Si solar cells were described. In particular, c-Si models and parameters were presented with the aim to calibrate and implement a simulation platform that describes accurately the physics inside c-Si solar cells. Additionally, the typical solar cell simulation scheme was presented. The simulation methodology introduced in this chapter highlighted the work presented on following chapters.

In Chapter 3, a theoretical study based on electro-optical numerical simulations of the impact of geometrical and doping parameters on main figures of merit of c-Si IBC solar cells was presented. The study was based on the

analysis of main design parameters identifying dominant mechanisms that improve or degrade conversion efficiency. Indeed, optimal doping were presented as result of Auger and SRH (interfaces) recombination result. Additionally, it was observed efficiency degradation as a result of wider gap region, due to the resistive losses and the SRH surface recombination losses. Similarly, an optimal emitter/pitch (R) coverage was obtained for R=0.85. This maximum efficiency is achieved for the best electrical shadowing (recombination) and resistive effect compromise. It was also observed efficiency degradation for larger pitch values, due to the FF decrease caused by the increase of the resistive losses

In Chapter 4, a novel IBC simulation model was presented, validated and deployed to study optical light-trapping and front recombination competitive mechanisms. Accordingly, a more accurate simulation methodology is presented to account in detail the optical and passivation mechanisms of front texturization. The opto-electrical losses of the investigated device have been identified quantitatively and qualitatively. Then, an optimization study about the optimal front architecture (doping, front-side texturing morphology), and rear-side geometry has been performed. Simulation results showed that a not-smoothed pyramid-textured front interface and an optimal FSF doping are mandatory to minimize both the optical and the recombination losses. Similarly, it has been showed that recombination losses are affected more by the doping profile rather than the surface smoothing. According to this result, it has been demonstrated that an IBC cell featuring an optimal FSF doping does not exhibit a significant efficiency improvement when the FSF passivation quality strongly improves, proving that IBC cell designs based on low-doped FSF require a very outstanding passivation quality to be competitive. As result of rear side optimization study, an efficiency improvement of

about 1%abs were achieved. Further, by improving both emitter and c-Si bulk quality, a 22.84% efficient solar cell were presented.

In Chapter 5, a validated simulation model is used to identify critical design parameters when using passivated contacts in a conventional solar cells. Simulation results demonstrated that energy barrier, electron and holes tunneling masses, and oxide thickness are the critical parameters that constrains transport mechanisms. Moreover, it was found that build in voltage behavior is correlated to band alignment pointing on the critical parameters related to deposited layer and crystalline silicon interface. For passivating contacts, material with small effective tunneling mass (h,e) and low energy barriers potentially improve the transport through tunneling oxide. Similar effect is obtained when it is deposited very thin tunneling oxide materials. A proper band alignment can be achieved when highly active doping is achieved on the deposited layer. Depending of build in voltage, a band bending inside crystalline silicon boost the collection of carriers on c-Si side, and repelling non collecting carriers.

7 Bibliography

[1] R. Perez and M. Perez, “A Fundamental Look at Energy Reserves for the Planet,” *IEA SHC Sol. Updat.*, vol. 50, no. October 2016, pp. 2–3, 2009.

[2] U.S. Energy Information Administration, “International Energy Outlook 2016,” 2016.

[3] S. I. Association, “International Technology Roadmap for Photovoltaic (ITRPV): Results 2015,” 2016.

[4] C. Battaglia, A. Cuevas, S. De Wolf, and A. Manuscript, “High-efficiency Crystalline Silicon Solar Cells: Status and Perspectives,” *Energy Environ. Sci.*, vol. 9, p. , 2016.

[5] W. Shockley and H. J. Queisser, “Detailed Balance Limit of Efficiency of p-n Junction Solar Cells,” *J. Appl. Phys.*, vol. 32, no. 3, p. 510, 1961.

[6] A. Richter, S. W. Glunz, F. Werner, J. Schmidt, and A. Cuevas, “Improved quantitative description of Auger recombination in crystalline silicon,” *Phys. Rev. B - Condens. Matter Mater. Phys.*, vol. 86, no. 16, p. 165202, 2012.

[7] A. Richter, M. Hermle, and S. W. Glunz, “Reassessment of the limiting efficiency for crystalline silicon solar cells,” *IEEE J. Photovoltaics*, vol. 3, no. 4, pp. 1184–1191, 2013.

[8] R. M. Swanson, “Approaching the 29% limit efficiency of silicon solar cells,” *Conf. Rec. Thirty-first IEEE Photovolt. Spec. Conf.*, pp.

889–894, 2005.

[9] M. A. Green, “The path to 25% silicon solar cell efficiency: History of silicon cell evolution,” *Prog. Photovoltaics Res. Appl.*, vol. 17, no. 3, pp. 183–189, May 2009.

[10] National Renewable Energy Laboratory, “Efficiency_Chart,” *Http://Www.Nrel.Gov/Ncpv/Images/Efficiency_Chart.Jpg*, 2016. [Online]. Available: http://www.nrel.gov/ncpv/images/efficiency_chart.jpg.

[11] R. S. Ohl, “Light-sensitive electric device,” US2402662 A, 1946.

[12] D. M. Chapin, C. S. Fuller, and G. L. Pearson, “A New Silicon p-n Junction Photocell for Converting Solar Radiation into Electrical Power,” *J. Appl. Phys.*, vol. 25, no. 5, p. 676, 1954.

[13] J. Perlin, *From Space to Earth: The Story of Solar Electricity*. Aatec Publications, 1999.

[14] M. Wolf, “Drift Fields in Photovoltaic Solar Energy Converter Cells,” in *Proceedings of the IEEE*, 1963, vol. 51, no. 5, pp. 674–693.

[15] J. Mandelkorn, C. McAfee, J. Kesperis, L. Schwartz, and W. Pharo, “Fabrication and Characteristics of Phosphorous-Diffused Silicon Solar Cells,” *J. Electrochem. Soc.*, vol. 109, no. 4, p. 313, Apr. 1962.

[16] E. S. Rittner and R. A. Arndt, “Comparison of silicon solar cell efficiency for space and terrestrial use,” *J. Appl. Phys.*, vol. 47, no. 7, 1976.

[17] M. A. Green, A. W. Blakers, and C. R. Osterwald, “Characterization of high-efficiency silicon solar cells,” *J. Appl. Phys.*, vol. 58, no. 11, 1985.

[18] N. Energy, “World ’s Highest Conversion Efficiency of 26.33% Achieved in a Crystalline Silicon Solar Cell - A World First in a Practical Cell Size -,” *New Energy and Industrial Technology*

Development Organization (NEDO) Kaneka Corporation, 2016. [Online]. Available: http://www.kaneka.co.jp/kaneka-e/images/topics/1473811995/1473811995_101.pdf.

[19] R. De Rose, M. Zanuccoli, P. Magnone, M. Frei, E. Sangiorgi, and C. Fiegna, "Understanding the Impact of the Doping Profiles on Selective Emitter Solar Cell by Two-Dimensional Numerical Simulation," *IEEE J. Photovoltaics*, vol. 3, no. 1, pp. 159–167, 2013.

[20] F. Feldmann, M. Bivour, C. Reichel, M. Hermle, and S. W. Glunz, "A passivated rear contact for high-efficiency n-Type silicon solar cells enabling high Vocs and FF>82%," *28th Eur. Photovolt. Sol. Energy Conf. Exhib.*, pp. 988–992, 2013.

[21] K. Masuko, M. Shigematsu, T. Hashiguchi, D. Fujishima, M. Kai, N. Yoshimura, T. Yamaguchi, Y. Ichihashi, T. Mishima, N. Matsubara, T. Yamanishi, T. Takahama, M. Taguchi, E. Maruyama, and S. Okamoto, "Achievement of More Than 25% Conversion Efficiency With Crystalline Silicon Heterojunction Solar Cell," *IEEE J. Photovoltaics*, vol. 4, no. 6, pp. 1433–1435, 2014.

[22] M. Taguchi, A. Yano, S. Tohoda, K. Matsuyama, Y. Nakamura, T. Nishiwaki, K. Fujita, and E. Maruyama, "24.7% Record efficiency HIT solar cell on thin silicon wafer," *IEEE J. Photovoltaics*, vol. 4, no. 1, pp. 96–99, 2014.

[23] P. Stradins, S. Essig, W. Nemeth, B. G. Lee, D. Young, a Norman, Y. Liu, J. Luo, E. Warren, a Dameron, V. Lasalvia, M. Page, and Y. Ok, "Passivated Tunneling Contacts to N-Type Wafer Silicon and Their Implementation into High Performance Solar Cells Preprint," *6th World Conf. Photovolt. Energy Convers.*, no. December, 2014.

[24] F. Granek, "High-Efficiency Backcontact Back-Junction Silicon Solar Cells," 2009.

[25] W. W. P. Mulligan, D. D. H. Rose, M. J. M. Cudzinovic, D. M. De Ceuster, K. R. McIntosh, D. D. Smith, R. M. Swanson, and D. M. De Ceuster, “Manufacture of solar cells with 21% efficiency,” *Proc. 19th EPVSEC*, no. 408, pp. 3–6, 2004.

[26] A. Fell, K. R. McIntosh, P. P. Altermatt, G. J. M. Janssen, R. Stangl, A. Ho-Baillie, H. Steinkemper, J. Greulich, M. Muller, B. Min, K. C. Fong, M. Hermle, I. G. Romijn, and M. D. Abbott, “Input parameters for the simulation of silicon solar cells in 2014,” *IEEE J. Photovoltaics*, vol. 5, no. 4, pp. 1250–1263, 2015.

[27] M. A. Stettler, “Device and process modeling: 20 Years at Intel’s other fab,” in *2014 International Conference on Simulation of Semiconductor Processes and Devices (SISPAD)*, 2014, vol. 1994, pp. 13–16.

[28] Synopsis, “Sentaurus Device User,” no. June. p. 2009, 2013.

[29] P. P. Altermatt, “Models for numerical device simulations of crystalline silicon solar cells—a review,” *J. Comput. Electron.*, vol. 10, no. 3, pp. 314–330, 2011.

[30] V. Moroz, J. Huang, K. Wijekoon, and D. Tanner, “Experimental and theoretical analysis of the optical behavior of textured silicon wafers,” in *2011 37th IEEE Photovoltaic Specialists Conference*, 2011, pp. 002900–002905.

[31] D. Thorp and S. R. Wenham, “Ray-tracing of arbitrary surface textures for light-trapping in thin silicon solar cells,” *D. Thorp, S.R. Wenham. 1997. Ray-tracing Arbitr. Surf. textures Light. thin silicon Sol. cells. Sol. Energy Mater. Sol. Cells 48 295-301.*, vol. 1–4, no. 48, pp. 295–301, 1997.

[32] P. Procel, M. Zanuccoli, V. Maccaronio, F. Crupi, G. Cocorullo, P. Magnone, and C. Fiegna, “Numerical simulation of the impact of

design parameters on the performance of back-contact back-junction solar cell," *J. Comput. Electron.*, vol. 15, no. 1, pp. 260–268, Mar. 2016.

[33] A. Schenk, "Finite-temperature full random-phase approximation model of band gap narrowing for silicon device simulation," *J. Appl. Phys.*, vol. 84, no. 7, pp. 3684–3695, 1998.

[34] R. De Rose, M. Zanuccoli, P. Magnone, E. Sangiorgi, and C. Fiegna, "Open issues for the numerical simulation of silicon solar cells," in *Ultimate Integration on Silicon (ULIS), 2011 12th International Conference on*, 2011, pp. 1–4.

[35] D. B. M. Klaassen, "A unified mobility model for device simulation I, Model equations and concentration dependence.pdf," *Solid-State Elecctronics*, vol. 35, no. 7. pp. 953–959, 1992.

[36] A. Richter, F. Werner, A. Cuevas, J. Schmidt, and S. W. Glunz, "Improved parameterization of Auger recombination in silicon," *Energy Procedia*, vol. 27, pp. 88–94, 2012.

[37] P. P. Altermatt, F. Geelhaar, T. Trupke, X. Dai, a. Neisser, and E. Daub, "Injection dependence of spontaneous radiative recombination in c-Si: Experiment, theoretical analysis, and simulation," *NUSOD '05 - Proc. 5th Int. Conf. Numer. Simul. Optoelectron. Devices*, vol. 2005, no. 2, pp. 47–48, 2005.

[38] P. P. Altermatt, A. Schenk, F. Geelhaar, and G. Heiser, "Reassessment of the intrinsic carrier density in crystalline silicon in view of band-gap narrowing," *J. Appl. Phys.*, vol. 93, no. 3, p. 1598, 2003.

[39] M. A. Green, "Self-consistent optical parameters of intrinsic silicon at 300 K including temperature coefficients," *Sol. Energy Mater. Sol. Cells*, vol. 92, no. 11, pp. 1305–1310, 2008.

[40] J. G. Fossum, R. P. Mertens, D. S. Lee, and J. F. Nijs, “Carrier recombination and lifetime in highly doped silicon,” *Solid. State. Electron.*, vol. 26, no. 6, pp. 569–576, Jun. 1983.

[41] P. P. Altermatt, J. O. Schumacher, A. Cuevas, M. J. Kerr, S. W. Glunz, R. R. King, G. Heiser, and A. Schenk, “Numerical modeling of highly doped Si:P emitters based on Fermi–Dirac statistics and self-consistent material parameters,” *J. Appl. Phys.*, vol. 92, no. 6, p. 3187, 2002.

[42] “PVLighthouse.” [Online]. Available: https://www2.pvlighthouse.com.au/resources/photovoltaic materials/refractive index/refractive index.aspx. [Accessed: 05-Nov-2016].

[43] A. Cuevas, R. A. Sinton, and M. Stuckings, “Determination of recombination parameters in semiconductors from photoconductance measurements,” *1996 Conf. Optoelectron. Microelectron. Mater. Devices. Proc.*, no. 2, pp. 16–19, 1996.

[44] W. Shockley and W. Read, “Statistics of the Recombinations of Holes and Electrons,” *Phys. Rev.*, vol. 87, no. 5, pp. 835–842, Sep. 1952.

[45] A. Cuevas, P. A. Basore, G. Giroult-Matlakowski, and C. Dubois, “Surface recombination velocity of highly doped n-type silicon,” *J. Appl. Phys.*, vol. 80, no. 6, p. 3370, 1996.

[46] S. W. Glunz, F. Feldmann, A. Richter, M. Bivour, C. Reichel, H. Steinkemper, J. Benick, and M. Hermle, “the Irresistible Charm of a Simple Current Flow Pattern – 25 % With a Solar Cell Featuring a Full-Area Back Contact,” *Proc. 31st Eur. Photovolt. Sol. Energy Conf. Exibition*, no. September, pp. 259–263, 2015.

[47] ASTM G173 - 03, *Standard Tables for Reference Solar Spectral Irradiances: Direct Normal and Hemispherical on 37° Tilted Surface*.

2012.

[48] K. McIntosh, M. J. Cudzinovic, D. D. Smith, W. P. Mulligan, and R. M. Swanson, “The choice of silicon wafer for the production of low-cost rear-contact solar cells,” in *3rd World Conference on Photovoltaic Energy Conversion*, 2003, no. May 11-18, pp. 971–974.

[49] J. Renshaw and A. Rohatgi, “Device optimization for screen printed interdigitated back contact solar cells,” *Conf. Rec. IEEE Photovolt. Spec. Conf.*, pp. 002924–002927, 2011.

[50] R. N. Hall, “Electron-Hole Recombination in Germanium,” *Phys. Rev.*, vol. 87, no. 2, p. 387, Jul. 1952.

[51] S. W. Glunz, R. Steeman, W. Warta, J. Knobloch, and W. Wettling, “Emitter dark saturation currents of high efficiency solar cells with inverted pyramids,” in *European Photovoltaic Solar Energy Conference*, 1995.

[52] P. Magnone, D. Tonini, R. De Rose, M. Frei, F. Crupi, E. Sangiorgi, and C. Fiegna, “Numerical simulation and modeling of resistive and recombination losses in MWT solar cells,” *IEEE J. Photovoltaics*, vol. 3, no. 4, pp. 1215–1221, 2013.

[53] R. De Rose, P. Magnone, M. Zanuccoli, E. Sangiorgi, and C. Fiegna, “Loss Analysis of Silicon Solar Cells by Means of Numerical Device Simulation :,” pp. 205–208.

[54] P. Procel, V. Maccaronio, F. Crupi, G. Cocorullo, M. Zanuccoli, P. Magnone, and C. Fiegna, “Analysis of the Impact of Doping Levels on Performance of back Contact-Back Junction Solar Cells,” *Energy Procedia*, vol. 55, pp. 128–132, 2014.

[55] R. R. King, R. A. Sinton, and R. M. Swanson, “Studies of diffused phosphorus emitters: saturation current, surface recombination velocity, and quantum efficiency,” *IEEE Trans. Electron Devices*, vol.

37, no. 2, pp. 365–371, Feb. 1990.

[56] F. Granek, M. Hermle, C. Reichel, A. Grohe, O. Schultz-Wittmann, and S. Glunz, “Positive effects of front surface field in high-efficiency back-contact back-junction n-type silicon solar cells,” in *Photovoltaic Specialists Conference, 2008. PVSC’08. 33rd IEEE*, 2008, pp. 1–5.

[57] P. J. Cousins, D. D. Smith, H. C. Luan, J. Manning, T. D. Dennis, A. Waldhauer, K. E. Wilson, G. Harley, and W. P. Mulligan, “Generation 3: Improved performance at lower cost,” *Conf. Rec. IEEE Photovolt. Spec. Conf.*, pp. 275–278, 2010.

[58] C. Reichel, F. Granek, M. Hermle, and S. W. Glunz, “Investigation of electrical shading effects in back-contacted back-junction silicon solar cells using the two-dimensional charge collection probability and the reciprocity theorem,” *J. Appl. Phys.*, vol. 109, no. 2, p. 24507, 2011.

[59] J. Renshaw, M. H. Kang, V. Meemongkolkiat, A. Rohatgi, D. Carlson, and M. Bennett, “3D-MODELING OF A BACK POINT CONTACT SOLAR CELL STRUCTURE WITH A SELECTIVE EMITTER Substrate Contact Spacing Emitter contact Base contact Emitter Contact Selective Shallow Emitter Emitter FSF Gap Base BSF Contact a b,” *Building*, pp. 375–379, 2009.

[60] O. Nichiporuk, A. Kaminski, M. Lemiti, A. Fave, and V. Skryshevsky, “Optimisation of interdigitated back contacts solar cells by two-dimensional numerical simulation,” *Sol. Energy Mater. Sol. Cells*, vol. 86, no. 4, pp. 517–526, 2005.

[61] P. Procel, V. Maccaronio, F. Crupi, I. Informatica, E. Sistemistica, and U. Calabria, “Analysis of the Impact of Rear Side Geometry on Performance of Back-Contact Back-Junction Solar Cells.”

[62] M. Hermle, F. Granek, O. Schultz-Wittmann, and S. W. Glunz, “Shading effects in back-junction back-contacted silicon solar cells,”

Conf. Rec. IEEE Photovolt. Spec. Conf., pp. 10–13, 2008.

[63] S. Kluska, F. Granek, M. Rüdiger, M. Hermle, and S. W. Glunz, "Modeling and optimization study of industrial n-type high-efficiency back-contact back-junction silicon solar cells," *Sol. Energy Mater. Sol. Cells*, vol. 94, no. 3, pp. 568–577, 2010.

[64] F. Granek, M. Hermle, D. M. Huljić, O. Schultz-Wittmann, and S. W. Glunz, "Enhanced lateral current transport via the front N + diffused layer of n-type high-efficiency back-junction back-contact silicon solar cells," *Prog. Photovoltaics Res. Appl.*, vol. 17, no. 1, pp. 47–56, Jan. 2009.

[65] L. J. Koduvelikulathu, V. D. Mihailetchi, G. Galbiati, A. Halm, R. Roescu, R. Kopecek, and K. Peter, "2-D Modeling of n-Type IBC Solar Cells Using SILVACO ATLAS Simulation," *Nusod 2011*, pp. 3–4, 2011.

[66] P. Ortega, E. Calle, G. von Gastrow, P. Repo, D. Carrió, H. Savin, and R. Alcubilla, "High-efficiency black silicon interdigitated back contacted solar cells on p-type and n-type c-Si substrates," *Prog. Photovoltaics Res. Appl.*, vol. 23, no. 11, pp. 1448–1457, Nov. 2015.

[67] C. S. Cho, D. Kong, and B. Kim, "Wet/dry etching combined microtextured structures for high-efficiency solar cells," *Micro Nano Lett.*, vol. 10, no. 10, pp. 528–532, 2015.

[68] A. Ingenito, O. Isabella, and M. Zeman, "Nano-cones on micro-pyramids: modulated surface textures for maximal spectral response and high-efficiency solar cells," *Prog. Photovoltaics Res. Appl.*, vol. 23, no. 11, pp. 1649–1659, Nov. 2015.

[69] J. Ximello, "Wet chemical textures for crystalline silicon solar cells," 2013.

[70] I. Kashkoush, G. Chen, D. Nemeth, and J. Rieker, "Optimized wet

processes and PECVD for high-efficiency solar cells," no. Figure 1, pp. 1–4.

[71] L. Fesquet, S. Olibet, J. Damon-Lacoste, S. De Wolf, A. Hessler-Wyser, C. Monachon, and C. Ballif, "Modification of textured silicon wafer surface morphology for fabrication of heterojunction solar cell with open circuit voltage over 700 mV," *Conf. Rec. IEEE Photovolt. Spec. Conf.*, no. 100, pp. 000754–000758, 2009.

[72] M. Cascant, D. Morecroft, K. Boulif, L. Vauche, H. Yuste, J. P. Ballester, I. Gonzalez, J. R. Rovira, J. J. Sierra, C. Castillo, E. E. Bende, and F. J. Castaño, "Front surface field formation and diffusion profiles for industrial interdigitated back contact solar cells," *27th Eur. Photovolt. Sol. Energy Conf. Exhib.*, no. September, pp. 2083–2086, 2012.

[73] D. S. Kim, V. Meemongkolkiat, A. Ebong, B. Rounsaville, V. Upadhyaya, A. Das, and A. Rohatgi, "2D-modeling and development of interdigitated back contact solar cells on low-cost substrates," *Conf. Rec. 2006 IEEE 4th World Conf. Photovolt. Energy Conversion, WCPEC-4*, vol. 2, pp. 1417–1420, 2007.

[74] A. Fell, K. C. Fong, K. R. McIntosh, E. Franklin, and A. W. Blakers, "3-D simulation of interdigitated-back-contact silicon solar cells with quokka including perimeter losses," *IEEE J. Photovoltaics*, vol. 4, no. 4, pp. 1040–1045, 2014.

[75] E. Franklin, K. Fong, K. McIntosh, A. Fell, A. Blakers, T. Kho, D. Walter, D. Wang, N. Zin, M. Stocks, E.-C. Wang, N. Grant, Y. Wan, Y. Yang, X. Zhang, Z. Feng, and P. J. Verlinden, "Design, fabrication and characterisation of a 24.4% efficient interdigitated back contact solar cell," *Prog. Photovoltaics Res. Appl.*, p. n/a-n/a, Oct. 2014.

[76] S. M. Kim, S. Chun, M. G. Kang, H. E. Song, J. H. Lee, H. Boo, S.

Bae, Y. Kang, H. S. Lee, and D. Kim, “Simulation of interdigitated back contact solar cell with trench structure,” *J. Appl. Phys.*, vol. 117, no. 7, p. 74503, Feb. 2015.

[77] M. Zanuccoli, P. Magnone, E. Sangiorgi, and C. Fiegna, “Analysis of the impact of geometrical and technological parameters on recombination losses in interdigitated back-contact solar cells,” *Sol. Energy*, vol. 116, pp. 37–44, 2015.

[78] R. De Rose, M. Zanuccoli, P. Magnone, E. Sangiorgi, and C. Fiegna, “Open issues for the numerical simulation of silicon solar cells,” *Ulis 2011 Ultim. Integr. Silicon*, pp. 1–4, 2011.

[79] A. Ingenito, O. Isabella, and M. Zeman, “Simplified process for high efficiency, self-aligned IBC c-Si solar cells combining ion implantation and epitaxial growth: Design and fabrication,” *Sol. Energy Mater. Sol. Cells*, vol. 157, pp. 354–365, 2016.

[80] A. Ingenito, O. Isabella, and M. Zeman, “Self-aligned low temperature process for interdigitated back contacted solar cells,” NL016047, 2014.

[81] O. S. Heavens, *Optical Properties of Thin Solid Films*. Dover Publications, 1991.

[82] S. C. Baker-Finch, K. R. McIntosh, D. Yan, K. C. Fong, and T. C. Kho, “Near-infrared free carrier absorption in heavily doped silicon,” *J. Appl. Phys.*, vol. 116, no. 6, p. 63106, 2014.

[83] F. Feldmann, M. Bivour, C. Reichel, M. Hermle, S. W. Glunz, H. Steinkemper, M. Hermle, S. W. Glunz, M. Simon, M. Bivour, C. Reichel, M. Hermle, S. W. Glunz, P. Stradins, S. Essig, W. Nemeth, B. G. Lee, D. Young, A. Norman, Y. Liu, J. Luo, E. Warren, A. Dameron, V. Lasalvia, M. Page, Y. Ok, Y. Tao, V. Upadhyaya, K. Jones, A. Rohatgi, and J. C. Goldschmidt, “Tunnel oxide passivated

rear contact for large area n-type front junction silicon solar cells providing excellent carrier selectivity," *Sol. Energy Mater. Sol. Cells*, vol. 131, no. PART A, pp. 46–50, 2014.

[84] H. Steinkemper, F. Feldmann, M. Bivour, and M. Hermle, "Numerical Simulation of Carrier-Selective Electron Contacts Featuring Tunnel Oxides," *1348 IEEE J. Photovoltaics*, vol. 5, no. 5, pp. 1348–1356, 2015.

[85] A. Ingenito, H. Dijkslag, G. Yang, O. Isabella, and M. Zeman, "n-PERC c-Si Solar Cell Architecture with Front and Rear Ion-Implanted Carrier-Selective Contacts." .

[86] A. Gehring and S. Selberherr, "Modeling of tunneling current and gate dielectric reliability for non volatile memory devices," *Device Mater. Reliab. IEEE Trans.*, vol. 4, no. 3, pp. 306–319, 2004.

[87] K. R. McIntosh and P. P. Altermatt, "A freeware 1D emitter model for silicon solar cells," in *Photovoltaic Specialists Conference (PVSC), 2010 35th IEEE*, 2010, pp. 2188–2193.

[88] F. Feldmann, C. Reichel, R. Müller, and M. Hermle, "The application of poly-Si/SiOx contacts as passivated top/rear contacts in Si solar cells," *Sol. Energy Mater. Sol. Cells*, vol. 159, pp. 265–271, 2017.

[89] A. Gehring, "Simulation of Tunneling in Semiconductor Devices," Technischen Universität Wien, 2003.

[90] A. Schenk, "Simulation of Gate Leakage Currents in UTB MOSFETs and Nanowires," 2010. [Online]. Available: http://www.sinano.eu/data/document/talk_schenk-sinano_nanosil-sept09.pdf.

[91] A.F.Ioffe Institute, "SiC - Silicon Carbide parameters database," *Electronic archive New Semiconductor Materials. Characteristics and Properties.* [Online]. Available:

http://www.ioffe.ru/SVA/NSM/Semicond/SiC/bandstr.html#Basic. [Accessed: 31-May-2016].

Summary

The use of simulation tools has become a strategic key to design more efficient solar cells. In this thesis, advanced c-Si solar cells structures and technologies have been discussed and evaluated by means of numerical simulations. As matter of fact, critical parameters have been presented providing guidelines to achieve the highest efficiency according to technological constrains. To this purpose, the evolution of c-Si solar cells with the target to approach to the realistic efficiency limit was reviewed in Chapter 1. Then, in Chapter 2, the general state-of-the-art properties related to c-Si solar cells were described focusing on their implementation in numerical simulations as basic methodology used in reminder chapters. Therefore, a theoretical study based on electro-optical numerical simulations of the impact of design parameters on main figures of merit of c-Si IBC solar cells was presented in Chapter 3. The study was based on the analysis of main design parameters identifying dominant mechanisms that improve or degrade conversion efficiency. In particular, optimal doping concentration and rear geometry were demonstrated as result of intrinsic and extrinsic recombination mechanisms trade-off, in case of doping; and, transport and recombination, in case of rear geometry. Then, the approach presented in Chapter 2 was upgraded in Chapter 4, when presenting a novel IBC simulation model. The opto-electrical approach was validated and deployed to study the front side of the IBC. The novel simulation methodology accounts in detail the optical and passivation mechanisms of front texturization. Simulation results showed that perfect ir-

regular pyramid-textured front interface and an optimal FSF doping are mandatory to minimize both the optical and the recombination losses. Similarly, it has been showed that recombination losses are affected more by the doping profile rather than the surface smoothing. As result of rear side optimization study, an efficiency improvement of about 1%abs were achieved. Additionally, by improving both emitter and c-Si bulk quality, a 22.84% efficient solar cell were presented. In Chapter 5, a validated simulation model was used to analyze critical design parameters when using passivated contacts in conventional solar cells. Simulation results demonstrated that energy barrier, electron and holes tunneling masses, and oxide thickness are the critical parameters that constrains transport mechanisms. Moreover, it was found that build in voltage behavior is correlated to band alignment. Such an effect, provide the understanding of in-diffused doping c-Si to support transport through tunneling oxide layer. Accordingly, passivated contacts design hints were presented. As a conclusion, in this thesis, design guidelines for IBC solar cells and conventional solar cells using passivated contacts were provided in order to support the fabrication of higher efficient advanced c-Si solar cells.

Sommario

L'utilizzo di strumenti di simulazione è diventato un approccio chiave nel processo di progettazione di celle solari ad alta efficienza. In questo lavoro di tesi, strutture e tecnologie relative a celle solari avanzate in silicio cristallino sono state discusse e analizzate per mezzo di simulazioni numeriche. In particolare, i parametri critici sono stati evidenziati fornendo linee guida per ottenere la massima efficienza in relazione ai vincoli tecnologici. Nel Capitolo 1 è stata presentata l'evoluzione delle celle in c-Si effettuata con l'obiettivo di avvicinarsi il più possibile agli effettivi limiti di efficienza.. Nel Capitolo 2, è stato descritto lo stato dell'arte generale relativo alle celle in silicio cristallino, focalizzandosi sulla loro implementazione in simulazioni numeriche. Di seguito, nel Capitolo 3, è stato presentato uno studio teorico dell'impatto dei parametri di progettazione sulle principali figure di merito di celle solari IBC in c-Si, basato su simulazioni elettro-ottiche. Lo studio è stato condotto analizzando i principali parametri e identificando i meccanismi dominanti che migliorano o degradano l'efficienza di conversione. In particolare, è stato dimostrato che le concentrazioni di drogaggio e le geometrie della faccia inferiore ottimali sono il risultato di compromessi tra meccanismi di ricombinazione intrinseci ed estrinseci, nel caso dei drogaggi, e tra maccanismi di trasporto e ricombinazione, nel caso delle geometrie posteriori. Successivamente, l'approccio presentato nel Capitolo 2 è stato ampliato nel Capitolo 4, in cui è stato illustrato un innovativo modello di simulazione per IBC. La simulazione elettro-ottica è stata validata e impiegata per lo studio della

regione frontale della cella *back-contact*. La nuova metodologia di simulazione modella in dettaglio il comportamento ottico e i meccanismi di passivazione sulla texturizzazione frontale. I risultati ottenuti hanno mostrato che un'interfaccia frontale texturizzata con piramidi irregolari e un FSF ottimale sono necessari per minimizzare sia le perdite ottiche che per ricombinazione. Analogamente, è stato evidenziato che le perdite per ricombinazione sono influenzate in misura maggiore dal profilo di drogaggio che dalla rugosità delle superficie. In relazione all'ottimizzazione del regione inferiore è stato ottenuto un miglioramento del 1% nell'efficienza assoluta e, in conseguenza di questo, migliorando sia la qualità dell'emettitore che della base in silicio cristallino, è stata presentata una cella solare con efficienza del 22.84%. Nel Capitolo 5, il modello di simulazione è stato usato per analizzare parametri critici di progettazione nell'applicazione di contatti passivanti in un cella solare convenzionale. I risultati delle simulazioni hanno dimostrato che i parametri principali che limitano il meccanismo di trasporto sono l'energia di barriera, le masse di tunneling di elettroni e lacune e lo spessore dell'ossido. Inoltre, è stato riscontrato che il comportamento del potenziale di *built-in* è correlato all'allineamento delle bande. Questo effetto fornisce la comprensione di come il silicio cristallino con drogaggio internamente diffuso supporta il trasporto per mezzo di tunneling attraverso lo strato di ossido. In accordo con le analisi svolte, sono state fornite delle indicazioni per la progettazione di contatti passivanti.

In conclusione, in questo lavoro di tesi sono state fornite linee guide per il design di celle solari IBC e celle solari convenzionali con contatti passivanti, con lo scopo di favorire processi di fabbricazione di celle solari in silicio cristallino ad alta efficienza.

List of Publications

[P1] P. Procel, A. Ingenito, R. De Rose, S. Pierro, F. Crupi, M. Lanuzza, G. Cocorullo, O. Isabella, M. Zeman, "Modelling and optimization study of a novel IBC c-Si solar cell based on ion implantation and epitaxial growth," submitted (under review) at Progress in Photovoltaics journal

[P2] M. Guevara, P. Procel, R. De Rose, N. Guerra, F. Crupi, and M. Lanuzza, "Design guidelines for a metallization scheme with multiple-emitter contact lines in BC-BJ solar cells," J. Comput. Electron., pp. 1–7, 2016.

[P3] P. Procel, M. Zanuccoli, V. Maccaronio, F. Crupi, G. Cocorullo, P. Magnone, and C. Fiegna, "Numerical simulation of the impact of design parameters on the performance of back-contact back-junction solar cell," J. Comput. Electron., vol. 15, no. 1, pp. 260–268, Mar. 2016.

[P4] M. Guevara, P. Procel, N. Guerra, S. Pierro, V. Maccaronio, F. Crupi, G. Cocorullo, "Numerical simulation of back contact-back junction solar cells with emitter double contact", Italian Conference on Photonics Technologies, Fotonica AEIT, Torino 2015

[P5] P. Procel, M. Guevara, V. Maccaronio, N. Guerra, F. Crupi, G. Cocorullo, "Understanding the optimization of the emitter coverage in BC-BJ solar cells", to be published in International Conference on

Crystalline Silicon Photovoltaics, Energy Procedia, Volume 77, pp. 149–152 Konstanz 2015

[P6] P. Procel, V. Maccaronio, F. Crupi, G. Cocorullo, M. Zanuccoli, P. Magnone, C. Fiegna, “Analysis of the impact of doping levels on performance of back contact - back junction solar cells”, International Conference on Crystalline Silicon Photovoltaics, Energy Procedia, vol. 55, pp. 128-132, 's-Hertogenbosch 2014.

[P7] P. Procel, V. Maccaronio, F. Crupi, G. Cocorullo, M. Zanuccoli, “Analysis of the impact of rear side geometry on performance of back-contact back-junction solar cells”, Italian Conference on Photonics Technologies, Fotonica AEIT, Napoli 2014

Acknowledgments

It is almost four years from I started my PhD period at UNICAL. During this time I got enjoyable time and good experiences I would like to thank for.

First of all, I want to express my gratitude to SENESCYT, it is a really amazing fruitful program I was part of. Thank you for the opportunity to pursuit my PhD.

I am very thankful with my tutor, Prof. Giuseppe Cocorullo, for the nice talks, remarks and advices.

Special thanks to my supervisor, Prof. Felice Crupi, for your encouragement, discussions and motivation. I expect to keep working with you in the future.

I am happy to acknowledge to Prof. Miro Zeman, Dr. Olindo Isabella and Dr. Andrea Ingenito for the collaboration, when applying modeling to fabricated devices in TUDelft.

I want to express my gratitude to Dr. Mauro Zanuccoli and Dr. Paolo Magnone for the nice ideas that encourage me on the beginning of my PhD.

During my PhD, I got the opportunity to meet wonderful colleagues. Special thanks to Dr. Silvio Pierro, Vincenzo Maccaronio, Dr. Domenico Albano, Dr. Sebastiano Strangio, Dr. Luis Villamagua, Dr. Raffaele de Rose, Marco Guevara, Noemi Guerra, Dr. Marco Lanuzza and Ramiro Taco.

I was very lucky to be able to work with motivated masters students during their thesis: Rosa Almache, Alfonso Gunsha, Luis Chuquimarca and Carolina Acaro. I thank you all for the time and nice discussions.

Deseo demostrar mi gratitud eterna a mi familia, a mis padres: Martha y Patricio por su trabajo y apoyo incondicional soy quien soy yo ahora. A mis

hermanos: Gabriela, Luis Miguel, José Antonio, por su paciencia y amistad. Nunca estuve solo, gracias a sus mensajes y llamadas estuvieron siempre conmigo. Los amo a todos.